Silica nanoparticles grown from organofunctionalised trialkoxysilanes: Synthesis, High Density Modification Strategies and Application

A thesis submitted for fulfilment of the degree of

Doctor of Philosophy

Daniel N. Mangos

BTech (Forens&AnalytChem), BSc (Hons)

Faculty of Science & Engineering

School of Chemical and Physical Sciences

June 2016

Declaration

‘I certify that this thesis does not incorporate without acknowledgement any material previously submitted for a degree or diploma in any university; and that to the best of my knowledge and belief it does not contain any material previously published or written by another person except where due reference is made in the text.’

Daniel N Mangos.

.... on ....

Acknowledgements

The amount of emotional energy that has gone into the preparation of this document is massive, and feels overwhelming to write about. That I have even started writing this page now, makes me actualize how much dedication goes into writing a thesis, and moreover, goes into the journey of one’s candidature – The Pilgrimage.

MANY have put up with my intensity, and have helped me develop strategies to channel it.

To Dave, I am grateful for your support through this process. You have been truly instrumental, reeling in some of my more animated ideas and helping me manage my energy constructively. Your assistance in helping me communicate science effectively and clearly has been a long process, I know, but a very rewarding one for me, for that I am truly thankful for your support, and more over, tolerance. I’ll never forget what you said early on in the piece, paraphrased I believe it was something like…

> *‘You will always learn something from a presentation, what to do, or what not to do.’*

That tomb of knowledge sits with me; I apply this wisdom to many other aspects of life now, also. I would like to also extend my thanks to the Lewis Research Group for their strength, energy and odd sense of humor.

To the University, Faculty and School of Chemical and Physical Sciences, thank you for always having open doors when I required assistance, and providing me with some breathing room during the latter part of my candidature. Gunter, I agree, entering the workforce whilst writing up was a risky choice, and not one I made easily. – Thanks extend to the research higher degrees committee for their leniency in extending my candidature a couple of times, when I have failed to meet expected deadlines.

To my close university friends ‘the tea group’ – Why are you guys my friends? – Seriously, I love you all so much. You’re always there with a pick me up when I’m feeling too serious – Thankyou.

Nick, Viv and James – I am lost for words, and they wouldn’t do you justice.

At times this document made me feel really heavy through the torso, as if I was wearing a lead vest. I have asked many ‘*who have walked this road’* what they do about it? – They look at me with deep, concerned (and sometimes narcissistic) eyes, and say

‘*Just get it done*’ or ‘*Just hand it up*’

Well… Here I go! **jumps into the abyss**

Summary

Owing to their thermal stability and non-toxicity, silica nanoparticles present themselves as platforms to build functionality through surface modification, for applications in medical imaging, cosmetics and for composite materials. While this concept is not novel, all too often, only low attachment density is obtained, if it is measured at all, which limits the understanding that can be obtained and in some cases, the validity of the structure-property relationships, which are obtained.

This thesis reports the straightforward synthesis, characterization, high density chemical modification and application of functionalised silica nanoparticles. The controlled growth, maturity time and condensation state have been examined for functional particles grown from (3-mercaptopropyl)trimethoxysilane (3-MPTMS), (vinyl)trimethoxysilane (VTMS), (phenyl)trimethoxysilane (PTMS) and (3-cyanopropyl)trimethoxysilane (3-CPTMS).

A simple and robust method to quantify the attachment density using ATR-FTIR was developed, using the Si-O-Si vibrational mode as an internal standard. Using a large excess of 11-bromo-1-undecene (up to 700 fold excess), up to 4.9 molecules per nm^2 were able to be attached to thiol terminated particles. This value compares favourably with 4.7 thiols per nm^2 calculated computationally, and 5.7 attachments per nm^2 suggested by thermogravimetric analysis. The rate of this attachment reaction was also investigated, with respect to time of UV irradiation and concentration of 11-bromo-1-undecene, which provided a means to achieve the controlled attachment of multiple molecules sequentially.

Following an understanding of the critical reaction conditions for simple chemistry, the attachment of Fullerene-C_{60} to produce C_{60}-f-SiNP was then then investigated. Small molecule chemistry was used to understand the chemistry of the adduct and prove covalent attachment.

Following the observation of ignition / combustion of C_{60}-f-SiNP during a Raman spectroscopy experiment, this excitation event was recreated, and thermally tracked in a controlled environment, revealing that hollow particles can be formed by laser ablation of the C_{60}-f-SiNP. Building upon this, a subsequent camera flash resulted in the reconstruction of the spheres into amorphous carbon sheets.

In summary, the high density attachment of a simple and more complex alkene has been demonstrated, through a free radical thiol-ene reaction on a silica nanoparticle surface. The research presented here provides multiple avenues for the applications requiring high density surface modification of particle surfaces. The natural development of this project would be to attach a high density of fluorophores or electron transport molecules on the particle surface due to the close proximity of the functional groups to one another.

Dedicated to

Newstovia
(Nick, Viv and James)

Your love and support guides me daily

Contents

List of Figures

List of Tables

Chapter 1| Introduction

Motivation

Whilst silica particles have been used for many years and have the potential for many applications in clinical dentistry, biomedical science, theranostic medicine and materials science, the effectiveness of modification of the surface has been largely “assumed”. While there are many reports of the modification of silica particles, parameters such as maximum theoretical attachment density are somewhat controversial and few publications actually fully characterise the materials that they produce. This thesis is focused on the chemistry that can occur between thiol functionalised silica nanoparticles (SiNP), and alkene terminated molecules 11-bromo-1-undecene and Fullerene-C_{60}, where the energetic properties of C_{60}-f-SiNP are considered.

The aims of this research are

1. The growth and characterisation of organo-functionalised silica nanoparticles without the use of TEOS, paying specific attention to particles grown from 3-mercaptopropyltrimethoxysilane (SiNP).

2. To present the thiol terminated SiNP as a platform for high density surface attachment of 11-bromo-1-undecene.

3. Attach Fullerene-C_{60} to the surface of SiNP, creating C_{60}-f-SiNP, and investigate the chemistry governing the reaction by considering solution ‘model’ chemistry.

4. Investigate and measure energetic events that occur when C_{60}-f-SiNP is subject to optical heating.

1.1 Nanotechnology

Nanotechnology has established itself as an innovative and revolutionary way to approach and tackle real world social, technological and environmental issues, allowing for smart and intelligent design of materials. Such endeavours are increasingly offering more portable and miniaturised technologies to improve quality of life,[1, 2] owing to unique ‘quantum’ effects that occur in the nanoscale regime (10^{-9} m). In this size range, the physical and chemical properties of materials are exceptional in comparison to their macroscale ‘bulk’ counterparts where properties such as colour,[3] conductivity,[4, 5] viscosity[6] and reactivity[7-9] are exploited.[10, 11]

The archetypal example of the difference between bulk and nanoscale ‘quantum’ properties of a material can be directly observed visually by difference in colour of solid ‘bulk’ gold and gold spherical nanoparticles, dispersed in water as shown in Figure 1. This is an example a nanoscale ‘quantum’ property, called surface plasmon resonance, which is responsible for the difference in colour and optical density of the solutions illustrated in Figure 1, and is shown graphically in Figure 2, where the absorption wavelength (λ–max) shifts as the particle size increases. It can also be seen that this quantum phenomenon is limited to the sub 100 nm regime, whereas the size of the particle increases past this threshold, an increased broadness in the peak shape (FWHM) is seen, where the particle is large enough to scatter light.

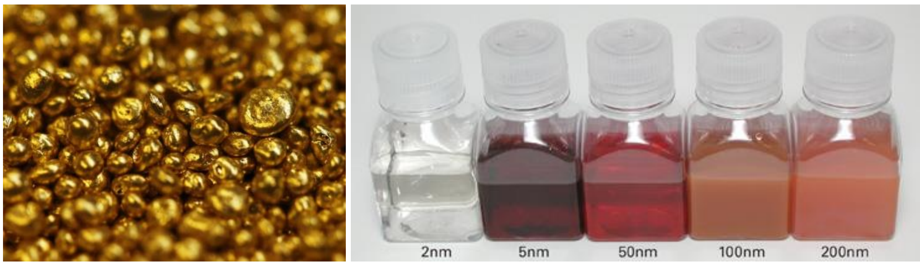

Figure 1: Comparison of bulk gold [12] (solid) to colloidal nano-gold [13] (aqueous)

1.2 Silica Nanoparticles

1.2.1 Synthesis of Silica Nanoparticles by Sol-Gel Chemistry

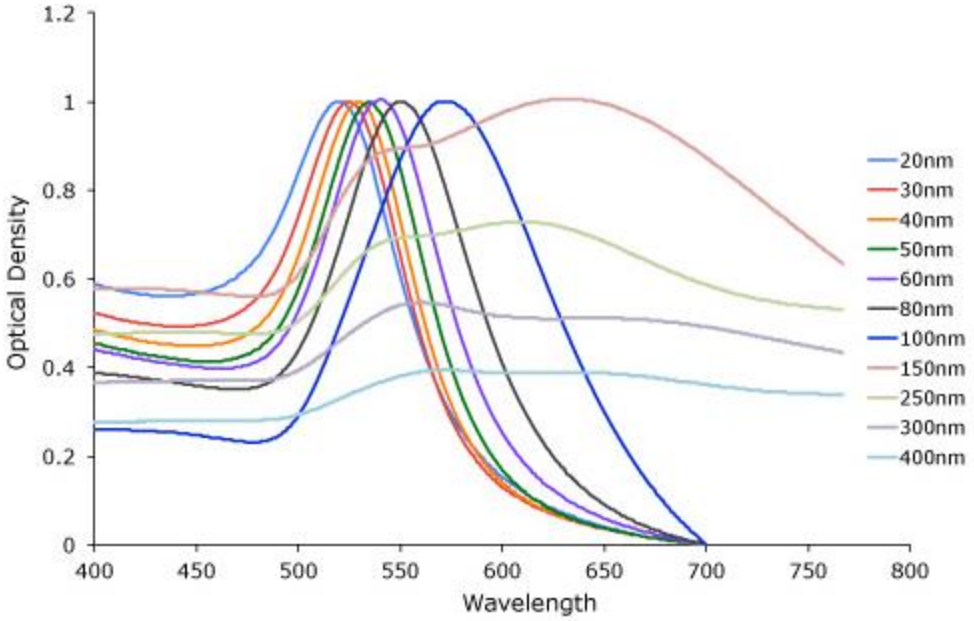

Figure 2: Regime of size dependence (nm) of gold nanoparticles exhibiting surface plasmon resonance[14]

With the highest surface area to volume ratio of all simple geometries, spherical nanoparticles present themselves as ideal candidates for a myriad of technological applications[15-20], including highly reactive surface scaffolds in catalysis[21], use in materials processing as nanofillers[22] as well as cargo delivery systems for drugs[23] and other bioactive molecules.[24-27]

Fabrication of nanomaterials, including nanoparticles is achieved by ‘top-down’ or ‘bottom-up’ processing techniques, of which there are a plethora to choose from, and options vary depending upon the purpose of the ‘nanounit’ created.[28-30] Bottom-up refers to the organisation of molecular structures where control over the material properties is governed by atomic and molecular organisation, as shown in Figure 3, which also describes the converse top-down approaches, which refer to division of a bulk material to create many smaller units.[28]

The most common method of synthesis for SiNP is by the ‘Stober Method’,

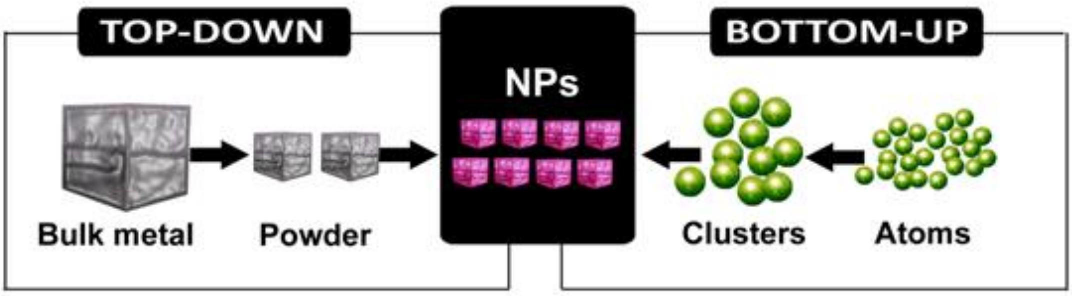

Figure 3: Top down and bottom up approaches to creating silica nanoparticles (NPs)[31]

1.2.2 Growth Mechanisms of Silica Nanoparticles

Silicon Dioxide or Silica (SiO_2), is one of the most abundant and readily available materials on earth, and exists as a variety of polymorphs within the earth's crust, some of which are crystalline.[32] Quartz is the most common crystalline form of silica discussed which has a regularly structured unit cell, and lattice, which is described and considered in further detail within this thesis.

In technologies where the fine structure of the particle is not important, cost effective top-down approaches to creating crude particulate silica structures are used, which include milling, machining, or pyrolysis of the bulk material, all of which are very energy intensive.[33] These processes are generally acceptable for silica grades to be incorporated into structural supports where thermo-mechanical and viscoelastic properties of the material need to be enhanced.[33] For the majority of recent scientific endeavours the bottom-up approach to creating silica nanostructures is favourable due to the increased control over molecular assembly and optimisation of size, structure and porosity, all of which is achievable by solution based processing techniques.[34]

Solid silica nanoparticles have been gaining increasing attention over the past decade, as shown in Figure 4. Owing to recent Food and Drug Administration (FDA) approval for use in human trials, theranostic use of nonporous silica nanoparticles is becoming more common.[35] 'Cornell Dots' (or C-Dots) are an example of such a particle, which demonstrate high sensitivity and specificity in the detection of tumours.[36] With a maximum diameter of ten nanometers they are easily extracted through the urinary tract.[37] The rigidity of the solid surface supports allows for increased resolution of the imaging agent, and the spherical geometry for high potential loading. Multiple research groups have noted an increase in quantum yield (imaging resolution) of fluorescent materials by using spherical nonporous silica supports.[38, 39] Particles such as these are generally produced by the Stober Method of condensation, which is discussed in detail.

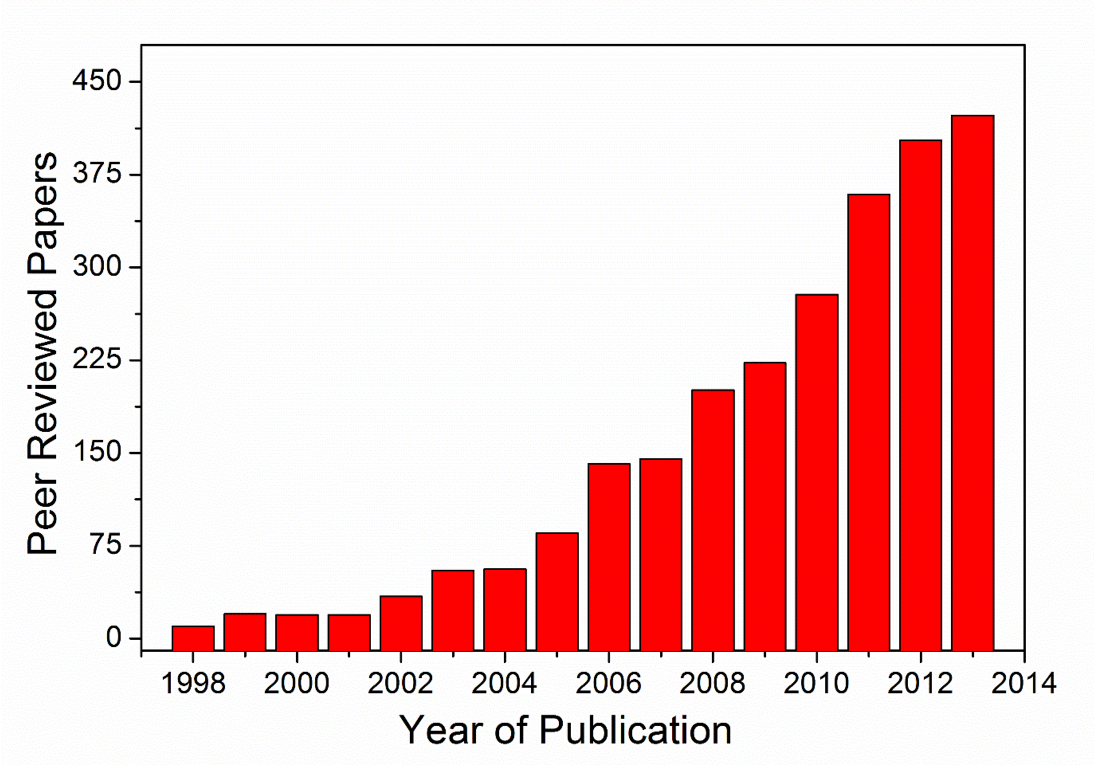

Figure 4: Thomson Reuters (Web of Knowledge) citation index for search term "solid silica nanoparticle"

1.2.3 Particle Types

The most common way to form silica nanoparticles is by bottom up synthetic approaches using a sol-gel process, where 'sol' refers to a stable colloidal suspension of solid particles in a liquid dispersant, and 'gel' refers to the ability of the process to generate three dimensional semi-solid networks, if allowed to mature.[40] Sol-gel, classically, describes the process in which large inorganic oxide structural networks are formed.[41] The formation of discrete and controlled size particles is commonly achieved by either monophasic aqueous systems,[42] or by a water in oil or oil in water emulsion,[43, 44] in which, liquid alkoxysilanes (Figure 5) undergo hydrolysis and subsequent polycondensation to form an insoluble precipitate.[45]

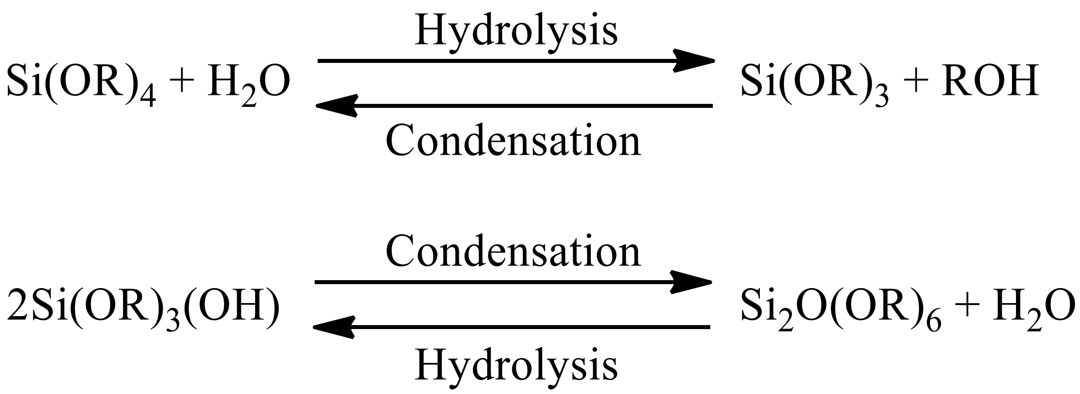

$$Si(OR)_4 + H_2O \underset{\text{Condensation}}{\overset{\text{Hydrolysis}}{\rightleftharpoons}} Si(OR)_3 + ROH$$

$$2Si(OR)_3(OH) \underset{\text{Hydrolysis}}{\overset{\text{Condensation}}{\rightleftharpoons}} Si_2O(OR)_6 + H_2O$$

Figure 5: Hydrolysis and Condensation of Organofunctionalised alkoxysilanes

The type of network structures created through the hydrolysis and polycondensation of alkoxysilanes is dependent on the type of alkoxysilane used as well as it's ratio to water, solvent effects, the nature of the catalyst, pH, temperature and relative concentrations of all these components in the resulting solution. Figure 6 shows the dependence of the relative rates of hydrolysis and condensation on pH as just one parameter.[45] Furthermore, the relative rate of condensation for the first, second, third and fourth condensation event are pH dependent, which results in the gel being an open fractal network at a pH of about 4 and a tight particle at a pH of about 9.

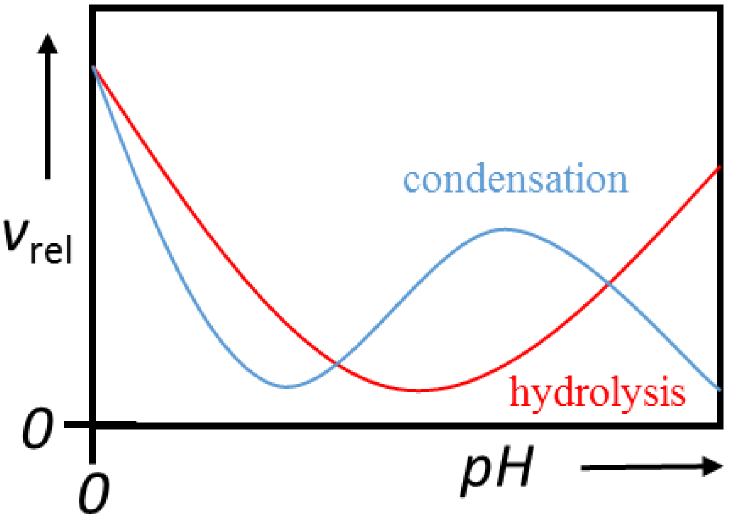

Figure 6: Relative hydrolysis and condensation rates for silanols (Si-OH) at each pH (adapted from [45])

Control over size and shape of particles synthesised by sol-gel processes is generally reliant on pH, concentration of alkoxysilane and solvent conditions. These can be altered to exploit the morphology and reactivity of the alkoxysilane precursor. At high pH, the transition from monomeric alkoxysilane species to spherical particle occurs in a sequential process of induction, nucleation and growth to form what is for all intents and purposes a charge stabilised liquid-solid colloid, as shown below in Figure 7.

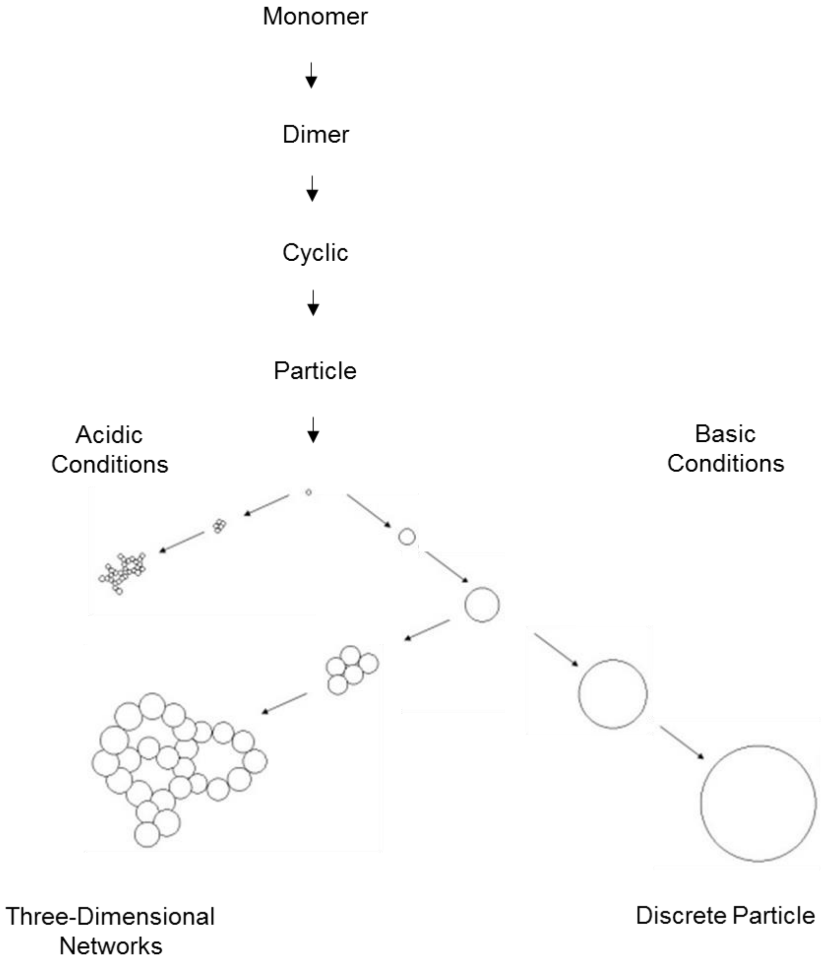

Figure 7: Schematic of pH dependence on sol-gel product (adapted from [45])

For the purposes of creating discrete spherical particles basic conditions are favoured. In such a case, hydrolysis and subsequently condensation reactions occur preferentially at the more substituted and less silanol (Si-OH) saturated silicon sites due to their susceptibility to nucleophilic attack. This occurs via an SN_2 like mechanism.[45]

The first step of silica particle formation is demonstrated in Figure 8, demonstrates that the first step of particle formation occurs through catalysed hydrolysis of the alkoxysilane precursor, and is controlled by the rate of hydrolysis for the purposes of creating spherical and discrete particles. This allows covalent siloxane networks to be formed through polycondensation of primary, secondary, tertiary and quaternary silicic acid species.

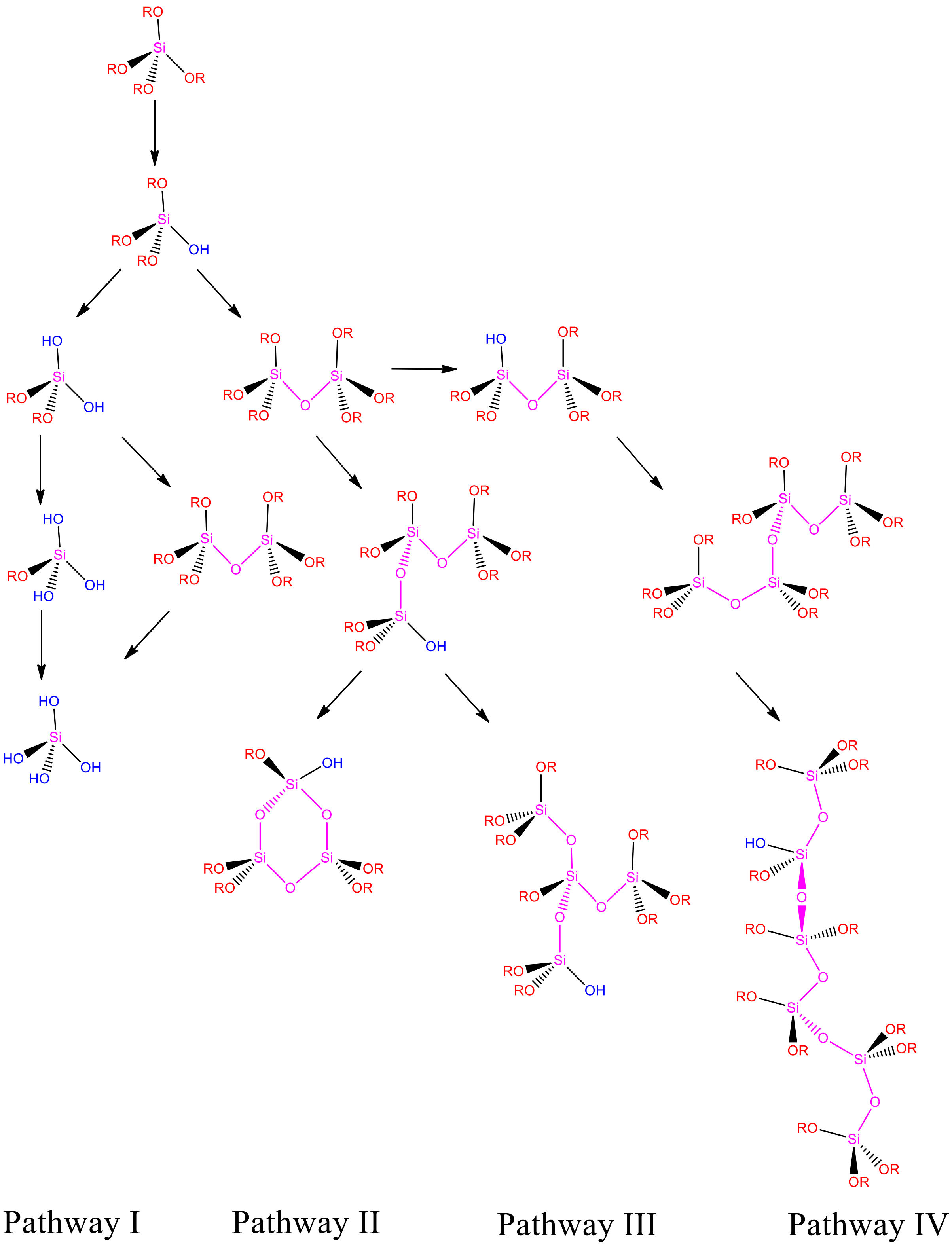

Figure 8: Potential growth pathways for the hydrolysis and/or condensation of tertiary alkoxysilanes. (Pathway I represents extreme hydrolysis and pathway IV represents extreme condensation)

If the potential induction and nucleation of Tetraethyl Orthosilicate (TEOS) were to be considered, possible reactivity pathways for S_c would be as shown below in Figure 8, where the '*O-R'* substituent is an ethoxy group. The preferred, and most likely, initial nucleation templates for base catalysed sol-gel synthesis would be the branched like structures which are labelled *Pathway II* and *III,* above. The pathways labelled *I* and *IV* represent the most extreme scenarios where repeated hydrolysis (*I*) or repeated condensation *(IV)* of primary substituted silicic acid networks occurs.

Once activated, these silicic acid networks polycondense, and start to create larger covalent networks, which are considered nucleation sites. With increased reactivity of the alkoxysilane monomer comes a greater number of nucleation sites created, which leads to a smaller size regime of particles being formed. This is achieved by adjusting reaction conditions that satisfy a high rate of nucleation and a short nucleation period, denoted as *II.*

This process is classically described by application of the La-Mer model to the sol-gel particle formation, which suggests at a critical concentration of precursor, particle formation will start, and maturity can be controlled as a function of monomer concentration as shown in Figure 9.[46] This graph visually describes that the supersaturation of the monomeric species (S_c) creates a burst of nucleation sites for controlled discrete particle growth.

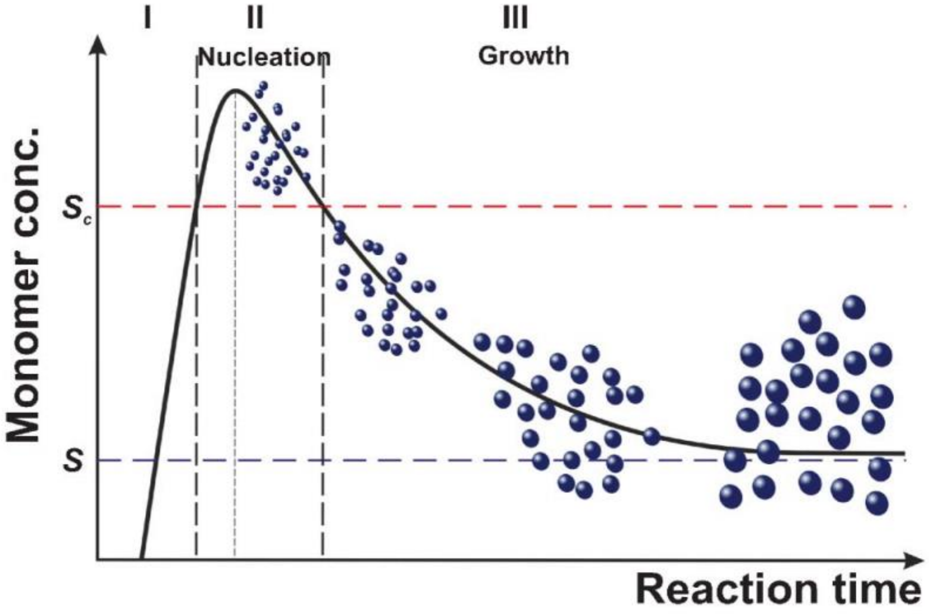

Figure 9: LaMer plot showing nucleation and growth formation of monodisperse particles, where S represents saturation, and S_c represents supersaturation.[46]

Whilst the classical process described in the LaMer model is true for quaternary alkoxysilanes, not all particle growth processes are homogenous in nature as those described above. In cases of heterogeneous nucleation, the monomer concentration over time for the early stages of growth can be described empirically, to a degree, where factors such as concentration of nucleated particles and critical nucleus radius are considered with respect to the critical monomer generation rate in the system. It is qualitatively understood that particle nucleation processes occur when precursor molecules reach a critical concentration in solution, which can be described thermodynamically, in liquid phase particle growth models. Nucleation and growth silica particles has also been studied by time resolved SAXS, where this data suggests already existing particles increase in size through the formation of new nuclei coagulating with pre-existing nuclei, as a mechanism toward larger particle growth [47].In such cases the rate of nucleation is heavily governed by the phase conditions of the solvent, which is in most cases modulated to control the diffusion of monomers toward the nucleus, where nucleation rate can be suppressed by increased diffusivity of the monomer.[48]

1.2.4 Characterisation of Silica Nanoparticles

As described above, the network formation of condensed silica particles is controlled by many factors which can result in the morphology of the particles varying from solids with continuous internal porous networks to solid non-porous structures.

The design strategy for internal particle structure depends on its intended use, generally as either a delivery vehicle or an anchor for activatable /stimuli responsive molecules. Mesoporous particles are designed to encase the cargo which they carry, which is generally contained within the pores of the structure, and are generally adsorbed to the interior surface by weak attractive forces, then desorbed by an external stimulus or diffusion.[49]

Conversely, in the case of solid nonporous structures, the agent of interest is generally covalently bound to the exterior surface. In such cases surfactants are generally avoided so that a highly condensed structure can be formed that acts as a rigid structure for anchoring of stimuli responsive molecules, such as fluorophores. A significant amount of literature pertaining to the use of mesoporous silica structures has examined the effective and efficient delivery of functional agents through interior motifs.[49-51]

In this thesis amorphous solid non-porous silica nanoparticles are used in all experimental protocol. Information regarding the distribution of particle sizes, internal porosity and external topography is obtained using a combination of analytical tools such as dynamic light scattering, gas adsorption and scanning electron microscopy.

1.2.4.1 Dynamic Light Scattering

In liquid based systems the volume of a particle in water (hydrodynamic volume), can be calculated, where the Brownian motion of particles and the free mean path taken in solution can be tracked using real time light scattering experiments. This process is known as dynamic light scattering, and the particle size is calculated using the Stokes-Einstein equation, as shown in below in Equation 1 and Figure 10 , where kT is the product of the Boltzmann constant k and temperature T, which is divided by a term on the denominator relating to the viscosity and size of the particle, and D is the rotational diffusion constant.[52]

$$R_H = \frac{kT}{6\pi\eta D}$$

Equation 1: Stokes-Einstein equation

Dynamic light scattering is a commonly used tool in tracking the growth of sol-gel particles, in a variety of inorganic processes, and is used in combination with various techniques in this thesis to determine average particle size

Figure 10: Schematic of Dynamic Light Scattering

1.2.4.2 Gas Adsorption using the Brunauer-Emmett-Teller (BET) method

Quantitative information about the average surface area as a function of weight (m^2 / gram) and internal structure of particulate surfaces can be acquired using nitrogen adsorption measurements of the material on a ‘bulk’ scale (100 mg). An inert gas (commonly nitrogen) is adsorbed to the surface of the particles, and the relative pressure at which this occurs in a fixed volume can provide information about the overall porosity and surface area of the sample, which could be due to inter or intra particle porosity.

1.2.4.3 Solid State NMR

Silicates are commonly analysed by magic-angle-spinning ^{29}Si NMR to determine the average condensation state of the particle, which can provide information about percentage conversion in the solid state.[53] In cases where organofunctionalised alkoxysilanes are present, which have an abundance of carbon and hydrogen atoms per silicon nuclei present, cross-polarization can be used from the ^{1}H or ^{13}C nucleus to provide an enhanced resolution of the silica condensation states.[54] Cross-polarisation NMR is a multinuclear technique, where the NMR process is complicated by the signal amplitude between the ^{29}Si nucleus and the ^{1}H or in some cases, ^{13}C nuclei. For the purposes of this thesis, spin locked protons are used, given their abundance, and variable amplitude modification is optimised for the recovery time (relaxation) of the nucleus.

1.2.4.4 IR and Attenuated Total Reflectance-IR (ATR-IR)

The tracking of vibrational modes in the infra-red region can be used as a quantitative tool where the absorbance of the analyte at specific concentrations is used to generate a calibration curve. For solid state samples, such as dried and cleaned nanoparticles, specific crystals with high refractive indicies such as germanium can be used to contact the sample, or act as a functionalisation substrate[55], where the infrared beam is able to enter the crystal and create an evanescent wave, where the light is internally reflected numerous times.[56] This is called an internal reflection element, where the beam does not pass through the sample, but bounces between the sample and the crystal, as can be seen below in Figure 11.

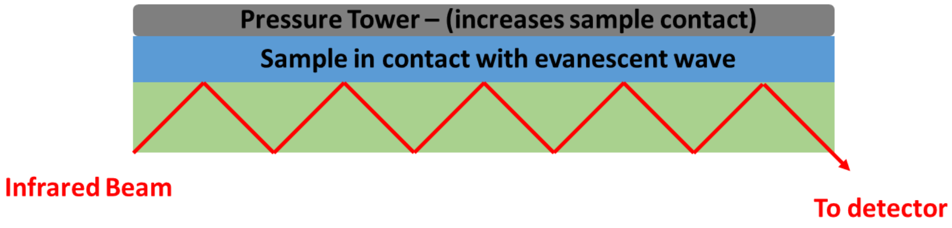

Figure 11: Pathway of the Infrared beam through the ATR-FTIR crystal

1.2.5 Surface Functionality of Silica Nanoparticles

1.2.5.1 Attachment Density of Silanols (Si-OH)

Surface Si-OH environments have been studied extensively, where the accepted literature value for the upper limit of hydroxyl presentation on the surface is 5.1 silanols per nm^{2}, known as the Kiselev-Zhuravlev constant.[57] It can be seen in Figure 12 that a variety of silanol environments can and do exist on surfaces, which differs from the flat two dimensional surface which is imagined but idealized when discussing surface structures. Other research groups quote comparable values for hydroxyl density on amorphous solid silica surfaces by a variety of techniques, shown in Table 1.

Figure 12: Different hydroxyl environments available on silica surfaces

Table 1: Density of silanol groups on silica surfaces

Reported Concentrations of Silanol Groups on Silica Surfaces (Si-OH)		
Attachments (#/nm)	Analysis Methods	Theoretical / Experimental
6.5	Adsorbed Molecule Interactions	Experimental[58]
4.6	Hydrogen to Deuterium Surface Replacement	Experimental[59]
7.85	Hydrolysis of Surface Silanols with Diborane	Experimental[60]
4.56	Monte Carlo Dehydration Simulation	Theoretical[61]
4.6 +/- 0.5	Zhuralev Model	Experimental[57]

Functionality can also be introduced to particle surfaces through the modification of the reactive Si–OH groups that present. Reactions such as aminations, esterifications and coupling based transfer catalysts have all been delivered to the surfaces of silanol functionalized particles.[62, 63] In the case of direct esterification, the attachment density is kinetically limited, where reactivity of the surface is correlated to the hydration coefficient of the silica as is shown in Figure 13.

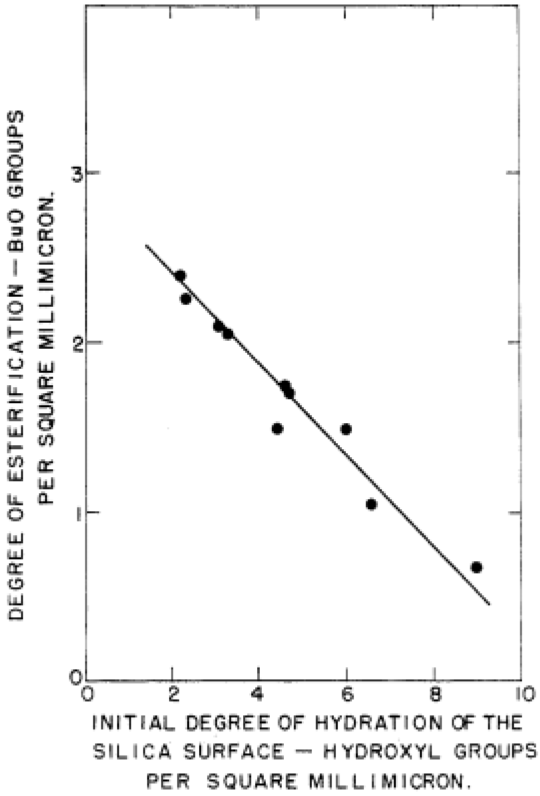

Figure 13: Surface coverage of butoxy groups on silica particles of varied hydration coefficient[62]

Controlling surface functionality relies heavily on the processing conditions used to introduce the functional monomer to the particle surface. Historically, the crosslinking agent tetraethylorthosilicate (TEOS) is used to assist particle maturation, following work pioneered by Stober et al.[34] In such cases the functional agent is introduced with the TEOS in a co-condensation technique, or in cases which higher density is required, the organically functionalized silane is condensed onto the surface of a pre-existing silanol particle[64], known as ‘post-synthesis seeding’ of the functional agent, as shown in Figure 14.

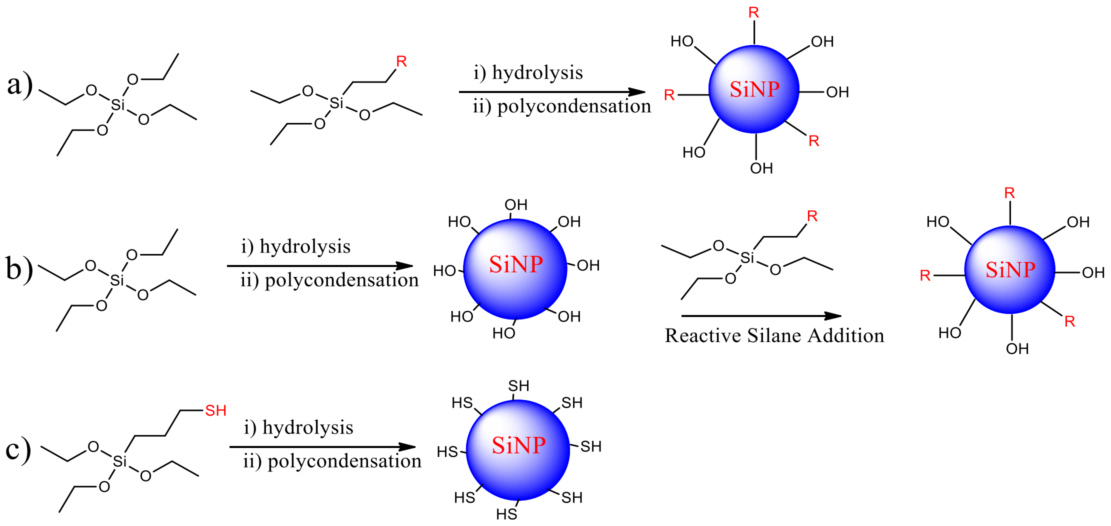

Figure 14: The formation of functionalized silica nanoparticles by by (a) co-condensation of functional monomer with TEOS (b) post synthesis seeding of functional monomer and (c) formation of particle from functional monomer.

In unique cases, functionalized alkoxysilanes can be polymerized without the need for TEOS, as shown in above in Figure 14(c). Nakamura and Ishimura have demonstrated that this is possible with (3-mercaptoproyl)trimethoxysilane, (3-mercaptopropyl)triethoxysilane, and (3-mercaptopropyl)methyldimethoxysilane.[65] The nucleophilicity of the alkyl sulfide heteroatom allows for ease of activated, either by deprotonation, or in the case of thiol, also free radical scavenging capabilities. It is difficult to optimize the phase chemistry so that other nucleophilic moieties such as amines are able to form nanoparticles as a sole silane source.[66]

1.2.5.2 Attachment Density of Organosilicates (Si-R)

In more complex systems, where specificity is required on surfaces, functionalized trialkoxysilanes such as those in Figure 15, displaying amine and thiol termni are employed over their hydroxylated (TEOS) counterparts. In the case of 3-mercaptopropyl and 3-aminopropyl alkoxysilanes, the heteroatoms inherent nucleophilicity can be easily activated by deprotonation, or in the case of the thiol is also capable to scavenge free radicals. Where chemical attachment efficacy is secondary, other molecules can be introduced to the organosilane arm, where the length of the arm has been shown to change the functionality (groups per nm^2) displayed on the surface. In the case below (Figure 15), the heteroatom is nitrogen, which is embedded within the alkyl chain.[67]

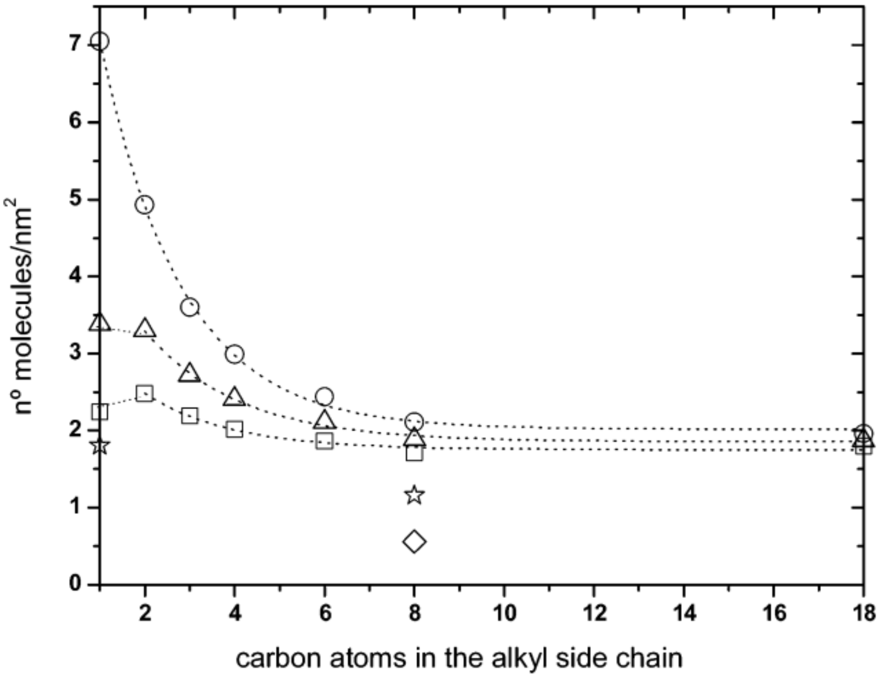

Figure 15: The influence of alkyl chain length on surface density of hydrocarbons attached to silica nanoparticles[67]

A variety of methods have been used to determine the chemistry that presents on the surface of silica nanoparticles. Where possible, the use of a spectroscopic technique under Beer-Lambert conditions is useful to quantitatively determine attachment density. Recent advances in applied particle chemistry show increased familiarity with a broad range of techniques, which include, but are not limited to, Thermogravimetric Analysis (TGA), X-Ray Photoelectron Spectroscopy (XPS), Elemental Analysis (via combustion), Stoichiometric Titrations, UV – Vis Spectrophotometry (UV/Vis), Fluorescence Spectrophotometry, Infrared Spectroscopy (IR), Raman and Dynamic Light Scattering and Particle Charge (Zeta Potential) Analysis, which are not all surface specific techniques.

An understanding of the chemistry that presents on the particle surface is crucial for controlling surface recognition in chemical sensing applications. To understand the sensitivity and selectivity of surface interactions a knowledge of the average density of functional agents that decorate the surface is required. It is demonstrated in Table 2 that calculations relating to attachment density can be derived from a variety of the different analytical techniques mentioned above. It can be seen that a variety of moieties have been attached to solid spherical nanoparticles with variable functionality (groups per nm^2) displayed on the surface.

Table 2: Empirical attachment density studies on solid silica supports

Quantitative Attachment Calculations		
Attachments (#/nm^2)	Analysis Methods	Functional Group
0.1>	UV dye adsorption	Amine[68]
0.1>	UV dye adsorption	Phenyl[68]
0.1>	Zeta Potential, SEM, Fluorescent Labelling	Amine[69]
0.1	TGA, XPS, BET	Amine
0.3	UV Vis, Titration	Isocyanate[70]
0.94	TGA, Elemental Analysis, Xray Absorption	Carboxylic Chains[71]
1.1 - 1.7	Elemental Analysis, Xray Structure	Different Length Fluorocarbons[72]
1.8	Particle Charge Detection Titration, Zeta Potential, Elemental Analysis	Amine[73]
1.8	Elemental Analysis	Amine[74]
2.9	TGA	ATRP Initiator[75]
5	TGA, ATR-FTIR	Thiol[76]
18-19	Fluorescence (Ninhydrin)	Amine[68]

1.3 Thiol-Alkene Chemistry

1.3.1 Thiol interactions with terminal olefins

Thiol-Alkene chemistry occurs through a hydrothiolation process where a thioether is formed by activation of a thionyl radical, which induces a high level of nucleophilicity of the moiety.[77] Generally, photoactivation of alkyl thiols to form thionyl radicals is preferred over other mechanisms, in the case of photosensitive reactants, thermally induced free radicals can be used. Molecules such as (3-azobisisobutyronitrile) are well known to generate free radicals through thermolytic scission. This free radical is scavenged by the sulfur heteroatom, and allows for successful addition of the thionyl functional group to the carbon carbon double bond. This reaction is coined a 'Michael Addition' in organic chemistry, and is the most simple of the hydrothiolation reactions. The main advantage of this reaction for the purpose of colloidal aqueous systems is that the formation of the thio-ether (C-S-C) it is tolerant to ambient conditions, and in some cases, does not require the presence of an initiator.[78]

However, when an initiator is used, the radical is not consumed in the reaction, as illustrated in Figure 16 below.

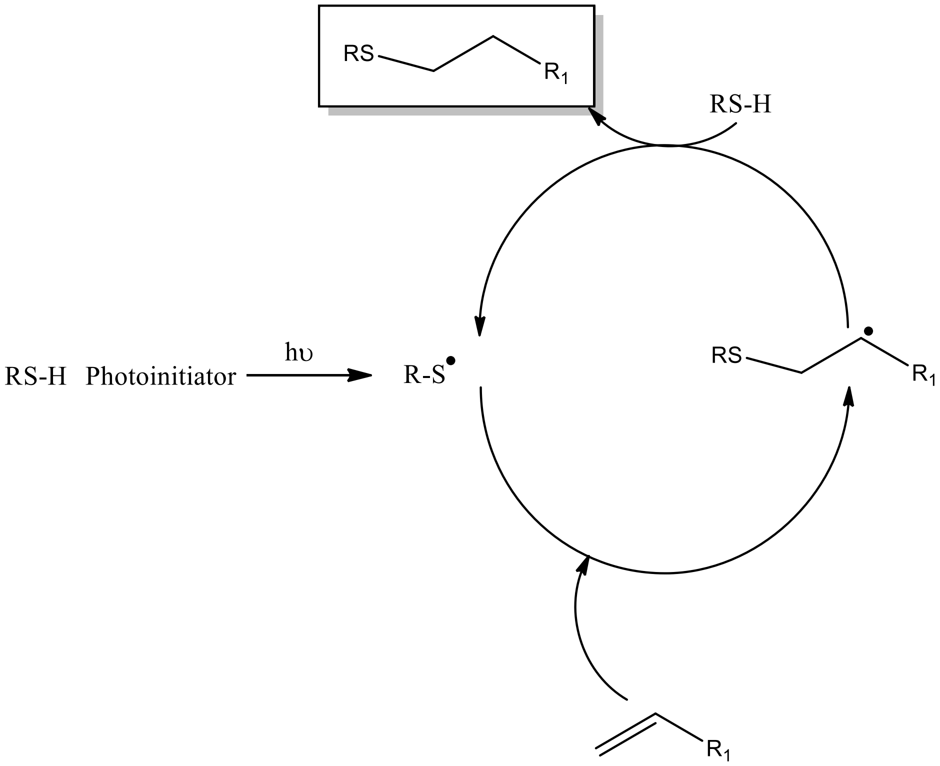

Figure 16: Free radical (photo)induced thiol-ene click mechanism[77]

Reactivity of thiols with a variety of different organic alkenes has been considered computationally[79] as demonstrated in Figure 17, where the chemical structures are illustrated in Figure 18. It has been demonstrated that electron rich alkenes are the most reactive, whilst electron poor alkenes, whilst still kinetically rapid, have inherent overall reactivity limitations. Despite this, it can be seen at equivalent stoichiometry, that not all alkenes will satisfy the requirements for stoichiometric reaction conditions, and that this specificity is limited.

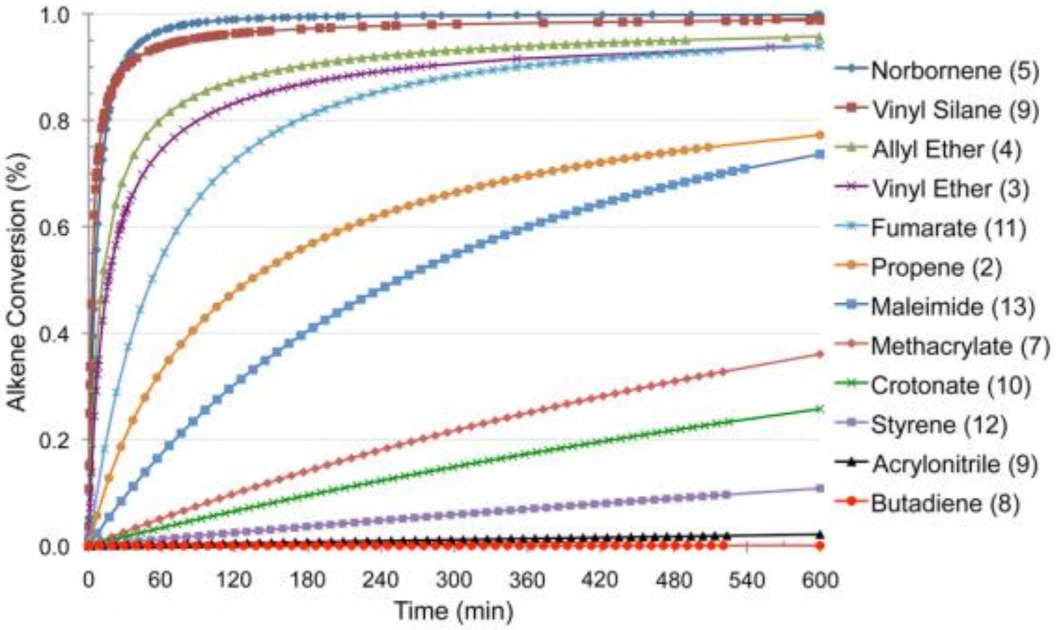

Figure 17: Reactivity of a variety of functionalised alkene precursors under thiol-ene conditions with methylthiol (equivalent stoichiometry)[79]

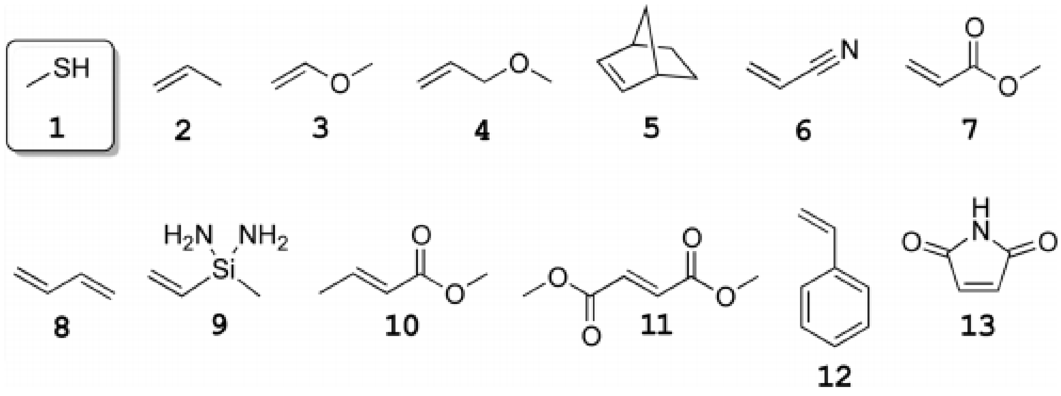

Figure 18: Different molecules used in the computational study[79]

1.3.2 Thiol interactions with Fullerene-C60

Fullerene-C60 is an alkene rich form of carbon, where the geometric arrangement of the carbon atoms gives it an icosahedral plane of symmetry. With the geometrical attributes of a soccer ball, the pentagons are used to provide a quasi-spherical curvature.[80] Two types of bonds exist within Fullerene-C60, at the junctions of two hexagons is the shorter carbon carbon bond [6,6], and at the points where the hexagon and pentagon meet a longer [5,6] bond exists, as shown below in Figure 19. The structure contains a total of 2(10+M) carbon atoms, corresponding to 12 pentagons and M hexagons. This is generally purchased commercially for research purposes, however it can be obtained from the purification of carbonaceous soot.[81]

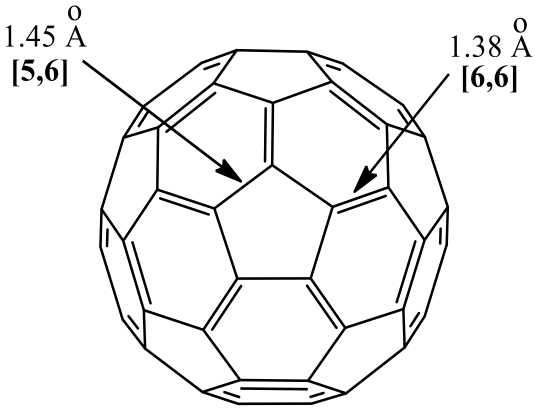

Figure 19: Bond length of Fullerene-C_{60}

Owing to its unique electronic and physico-mechanical properties, Fullerene-C_{60} is becoming an increasingly relevant carbon allotrope to fundamental and applied researchers alike.[82] Fullerene-C_{60} presents itself as an excellent platform for chemical exploitation, where the quasi-spherical Fullerene-C_{60} is susceptible to free radical attack, and has been coined by many a 'radical sponge'.[83] Through selective and multivalent chemical exploitation of the conjugated structure, Fullerene-C_{60} derivatives such as PCBM have been identified as useful electron acceptors, enhancing the properties in photovoltaic systems, and functionalised Fullerene-C_{60} molecules also present as mechanically stable additives for materials processing[84] as well as demonstrating antioxidant properties for biological purposes.[85, 86]It has also been demonstrated that the π conjugation of Fullerene-C_{60} derivatives allows for self-directed assembly into robust and tuneable nano/micro superstructures.[87]

It is well known that Pristine Fullerene-C_{60} is incompatible with most systems in its native state, where tailor made derivatives have been made to meet the requirements of specific systems, in which both the physical and chemical properties of the Fullerene-C_{60} moiety are not compromised. Such derivatives are generally synthesised through cycloaddition mechanisms such as the Bingel-Hirsch[88], Prato[89] and Diels-Alder[90] reactions or through direct addition[91] where the bonds between benzene [6,6] in Fullerene-C_{60} are localised and dienophilic. It is well understood that addition reactions involving Fullerene-C_{60} are favourable as they relieve strain of the quasi-spherical and electron deficient polyalkene, and ideally this is achieved in a controlled manner.

Thiol-ene chemistry techniques have been previously attempted with Fullerene-C_{60} structures, however it resulted in a reversible reaction, favouring reformation of reactants under photo generated free radical mechanisms.[92] It is well established that Fullerene-C_{60}

acts as a radical sponge when it undergoes photoexcitation, due to the hybridisation and overall geometry of the structure [80, 92] Whilst attempts to utilise thermally generated free radical mechanisms have been employed previously in the polymerisation of Fullerene-C_{60} structures a lack of control over the reactivity results in the byproduct of the free radical generator (AIBN) attaching to the Fullerene-C_{60} unit.[93]

Successful control and utility of this reaction via thermally generated free radical control is discussed in this thesis.

1.3.2.1 Fullerene-C_{60} as an Energetic Material

Fullerene, Graphene and Nanotubes are carbon allotropes which are sp^2 hybridised and have shown to present interesting electronic and photoactive properties in their native state. Laser ignition has induced molecular reconfiguration for various functionalised carbon allotropes, including Fullerene-C_{60}[94] and Carbon Nanotubes[95], where the carbonaceous material forms unique structures as shown in Figure 20. Theories and mechanisms underlying the reconfiguration theory are discussed in greater detail in Chapter 6. It is envisioned that reconstructions in the materials shown below, which have differing aspect ratios than the material they are derived from, could create a safer material with a less threating aspect ratio and dimensions that carbon nanotubes and fullerenes, which can puncture and permeate cells.

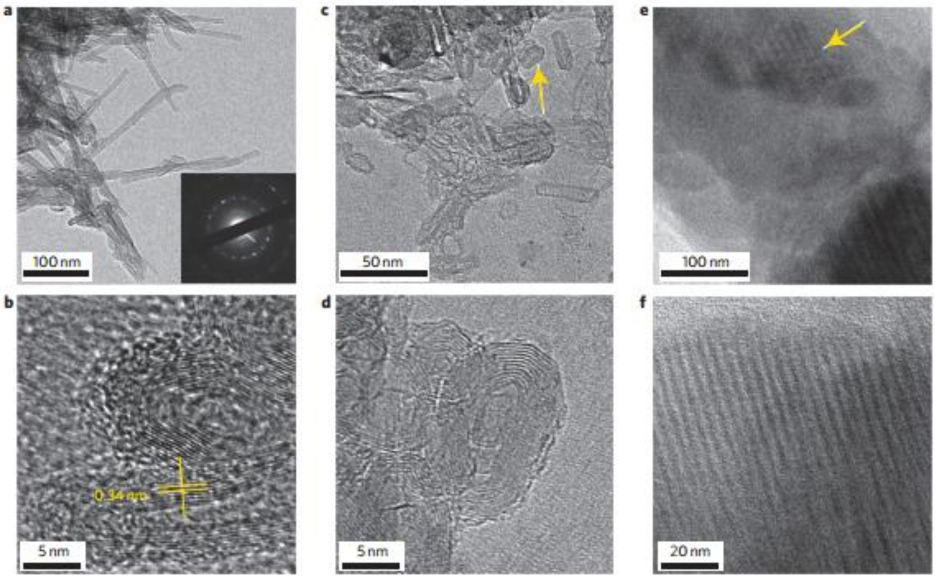

Figure 20: Structures and Orientations of various carbon polymorphs created from laser ignition of multi walled nanotubes (a-d) and single walled nanotubes (e and f)[94]

Chapter 2| Experimental: Materials and Methods

2.1 Overview

This chapter covers general experimental procedures used in this thesis. This includes the relevant materials and methods used in synthetic and analytical preparations. Firstly, a chemical list as well as the preparation of organo-functionalised particles is discussed. Secondly, information regarding instruments used and measurement parameters are outlined. Finally, radiation sources for C_{60}-f-SiNP heating are discussed.

2.2 Chemicals List

Table 3: Consumables used in this thesis

Class of Item	Consumable Name	Purity / Concentration	Supplier
Silanes	3-mercaptopropyltrimethoxysilane	95%	Sigma-Aldrich
	3-cyanopropyltriethoxysilane	95%	Santa Cruz Biochemicals
	vinyltriethoxysilane	97%	Sigma-Aldrich
	phenyltrimethoxysilane	97%	Sigma-Aldrich
Attachment Reagents	11-bromo-1-undecene	95%	Sigma-Aldrich
	fullerene-C60	99.50%	Lumtec
	dodecanethiol	95%	Tokyo Chemical Industry
Initiators	azobisisobutyronitrile	98%	Sigma-Aldrich
	benzophenone	99%	Sigma-Aldrich
Purification Materials	fumed Silica	N/A	Aerosil
	Bio-Rad™ SX-1 Support	N/A	BIO-RAD
Solvents	milli-Q Water		Flinders University
	ammonia hydroxide (28% in H2O)	99.99%	Chem-Supply
	absolute ethanol	99.80%	Chem-Supply
	iso-propanol	99%	Chem-Supply
	dichloromethane	99%	Tokyo Chemical Industry
	toluene	99%	Tokyo Chemical Industry
	chlorobenzene	99%	Tokyo Chemical Industry
	hexane	90%	Tokyo Chemical Industry
	chloroform	99%	Tokyo Chemical Industry
	chloroform-D	99.96%	Cambridge Isotope Laboratories
	toluene-D	99.94%	Cambridge Isotope Laboratories
	hexane – AR	>95%	Sigma-Aldrich
	dichloromethane - AR	99.50%	Sigma-Aldrich
	toluene - AR	99.50%	Sigma-Aldrich
MALDI-Tof-MS Matrix	9-nitroanthracene	93%	Sigma-Aldrich

2.3 Particle Synthesis

2.3.1 Preparation of thiol functionalised silica nanoparticles

A stable colloidal suspension of thiol functionalized SiNPs was prepared by dropwise addition of 3-mercaptopropyltrimethoxysilane (MPTMS - 57 $\boldsymbol{\mu}$l, 3.07 × 10^{-4} mol) to a blend of 28% ammonia (3.60 ml) and deionized water (46.4 ml) and allowed to stir at room temperature for 3 days at 550 rpm, creating $\boldsymbol{d}_{avg}$ 170 nm particles with thiol functionality.

A 1.56 mM solution was made using the above methodology, creating d_{avg} of 30 - 50 nm. Where the scale of the reaction was 200 mL, using 185.6 mL H_2O and 54 ul of MPTMS.

2.3.2 Preparation of cyano functionalised silica nanoparticles

A stable colloidal suspension of cyano functionalized SiNPs was prepared by dropwise addition of cyanopropyltriethoxysilane (CPTES – 1025 $\boldsymbol{\mu}$l, 4.30 x 10^{-3} mol) to a blend of 28% ammonia (3.60 ml) and deionized water (46.4 ml) and stirred vigorously at 800 rpm for the space of 3 hours, after leaving for half an hour at 300 rpm, creating $\boldsymbol{d}_{avg}$ 2000 nm particles with cyano functionality.

2.3.3 Preparation of vinyl functionalised silica nanoparticles

A stable colloidal suspension of vinyl functionalized SiNPs was prepared by dropwise addition of vinyltriethoxysilane (VTES – 908 $\boldsymbol{\mu}$l, 4.30 x 10^{-3} mol) to a blend of 28% ammonia (3.60 ml) and deionized water (46.4 ml) and stirred vigorously at 800 rpm for the space of 3 hours, after leaving for half an hour at 300 rpm, creating $\boldsymbol{d}_{avg}$ 650 nm particles with vinyl functionality.

2.3.4 Preparation of phenyl functionalised silica nanoparticles

A stable colloidal suspension of phenyl functionalized SiNPs was prepared by dropwise addition of phenyltrimethoxysilane (PTMS - 800 $\boldsymbol{\mu}$l, 4.30 x 10^{-3} mol) to a blend of 28% ammonia (3.60 ml) and deionized water (46.4 ml) and stirred vigorously at 800 rpm for the space of 3 hours, after leaving for half an hour at 300 rpm, creating $\boldsymbol{d}_{avg}$ 725 nm particles with phenyl functionality.

For preparation of phenyl functionalized silica nanoparticles at different particle sizes, the concentration of phenyltrimethoxysilane was altered to (0.014 M, 0.028 M, 0.056 M, 0.113 M, 0.226 M, 0.339 M) and procedurally was kept consistent with the synthesis of particle in Section 2.4.1, above.

2.3.5 Particle Cleaning

Particles were cleaned thoroughly by centrifugation and removal of the supernatant liquid, and redispersed, three times, at 4500 rpm.

2.4 General Preparations

2.4.1 Formation of Calibration Curve

For creation of the calibration curve 0.1, 0.2, 0.3, 0.4, 0.7, 0.9 and 1 **μ**l of 11-bromo-1-undecene were added to 13 mg samples of thiol terminated SiNPs (with an average diameter of 170 nm) via a GC syringe. Samples were homogenized with mortar and pestle, left to dry in vacuum overnight at 50°C and analysed via ATR-FTIR spectroscopy.

2.4.2 Formation of bromo-alkane functionalised nanoparticles

For nanoparticle functionalization in the photo generated free radical systems, 11-bromo-1-undecene (0.15 ml, 6.8×10^{-4} mol) and benzophenone photo initiator (23.3 mg, 1.3×10^{-4} mol) were added to 25 ml of thiol terminated SiNPs solution. The mixture was stirred for 30 min under an Oriel Illuminator UV lamp Model 82420.

2.4.3 Kinetic experiments for attachment of bromo-alkane

Kinetic control using photo irradiation was done under similar conditions to nanoparticle functionalization described earlier. The reaction was allowed to proceed for 1, 5, 10, 15 and 30 min respectively under the conditions specified in section 2.4.2.

2.5 Analytical Techniques

2.5.1 Dynamic Light Scattering

Nanoparticle solutions were analysed using dynamic light scattering (DLS) with a Malvern Instruments 'High Performance Particle Sizer' model HPP5001. DLS measures the Brownian motion of a particle in a given solute, and parameters were set given the relative viscosity of the solvent and an approximation of the chemical composition of the particle. Correlation data was analysed using Malvern Instruments software.

The DLS measurements were made at the following specifications. Temperature, 25 °C; path length, 1 cm; attenuation index, 8; mean position, 1.6 mm; run duration, 12 scans. All runs were done in triplicate in monomodal mode.

An example of the 30 – 50 nm particles synthesised is shown below in Figure 21, where the raw correlation data and data fit demonstrate how the size intensity profile is created.

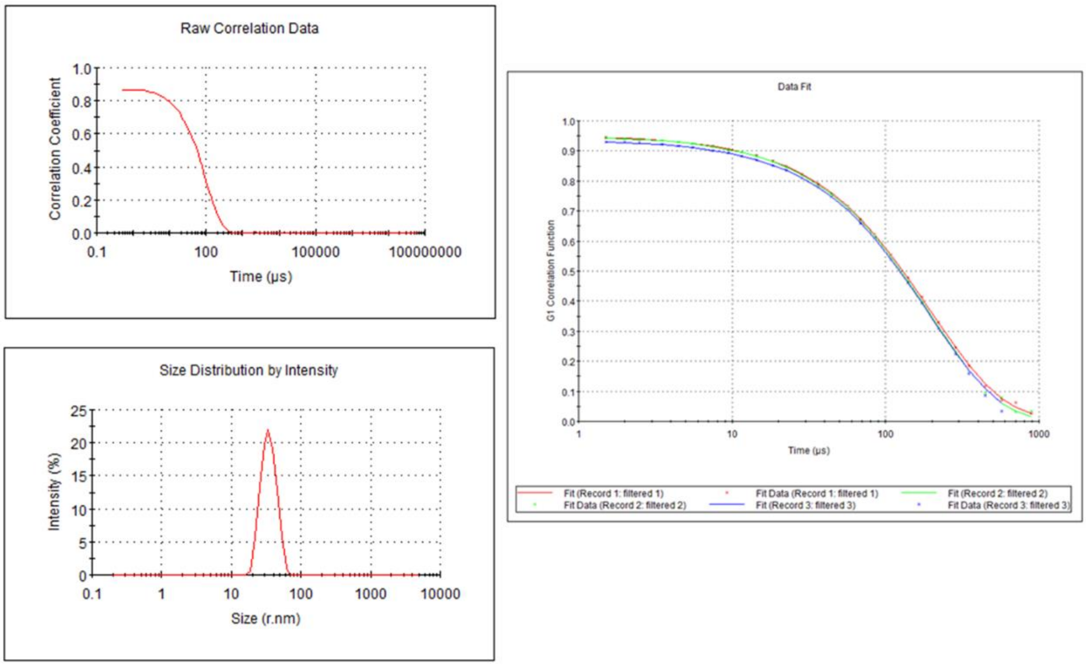

Figure 21: Multiple verification mechanisms to ensure measurement reliability.

2.5.2 Scanning Electron Microscopy

Nanoparticles were prepared for scanning electron microscopy (SEM) imaging by coating with metal using a Quorumtech K575X sputter coater. A 10 nm platinum or gold coating was applied to the sample as measured using a film thickness monitor. Thiol functionalized particles were analysed using FEI Phenom^{TM} SEM

2.5.3 NMR Details

2.5.3.1 Silica NMR

Solid State – Magic Angle Spinning (SS-MAS) NMR was conducted on a Bruker 600 instrument, to determine the condensation state of silica. This work was assisted by Ass. Prof. Martin Johnston.

2.5.3.2 DDT-f-C$_{60}$ NMR

^{1}H NMR (600 MHz) spectrum of DDT and DDT-f-C$_{60}$ were measured with a Bruker Biospin DRX-600 spectrometer, and ^{13}C NMR (75 MHz) of the compounds were measured on a JOEL AL300 spectrometer, using TMS as an internal standard. These samples were prepared using deuterated chloroform.

2.5.4 Surface area analysis by nitrogen sorption

Surface area was determined experimentally by Brunauer–Emmet–Teller (BET) isotherm measurements on a micromeritics TriStar II 3030 surface area and porosity analyser. SiNPs were dried at 30 mbar and 60 °C overnight and then at 0.1 mbar at 90 °C for 3 h prior to isothermal analysis.

2.5.5 Computational Chemistry

Calculations pertaining to the growth and hydration of SiNP was performed using Materials Studio 8.0 by Accelrys Software Inc. Molecular constructs were geometry and energy optimized using the Forcite, a molecular mechanics tool. For cases where hydration of the particle were considered, an amorphous cell was created before calculations, where the particle and a water fraction were calculated, were the lowest energy configuration from a data set of 20 constructions was considered internally by the software suite.

2.5.6 Solid State UV-Vis

Ultraviolet-visible absorption measurements on solid particles were performed on a JASCO V-670 UV-Visible/NIR double-beam Spectrophotometer equipped with an integrating sphere was used to collect solid state spectra of SiNP, Fullerene-C_{60} and C_{60}-f-SiNP at a scan rate of 2 nm / min.

2.5.7 Liquid UV-Vis

Ultraviolet-visible absorption measurements in liquid state were performed on a Hitachi U-2910 spectrophotometer using spectroscopic grade hexane as the solvent

2.5.8 MALDI-ToF-MS

A Shimadzu Axima Confidence (CFR Plus) station was used in Linear Reflectron Mode to measure the mass spectrum of Fullerene-C_{60} containing compounds. In the case of C_{60}-f-SiNP no matrix was required. In the case of C60-f-DDT, 9-nitroanthracene was used as a matrix.

2.5.9 Transmission Electron Microscopy

For results pertaining to Chapter 6, with ablated C_{60}-f-SiNP, Transmission electron microscopy / EDX of the materials was performed at Adelaide Microscopy, with a Philips CM200 Transmission Electron Microscope, where the sample was taken up with chloroform and prepared on a copper based grid before analysis.

For results pertaining to Chapter 5, where TEM/EDX measurements of C_{60}-f-SiNP were performed, a JOEL JEM 2100F Field Emission Microscope was used.

2.5.10 Atomic Force Microscopy

10 µL of nanoparticles at ~10 mg/mL in acetone was placed onto freshly cleaned silicon wafer and allowed to dry under a gentle stream of Argon gas. Images were acquired in AC tapping mode on an Asylum MFP3D SPM (Asylum Research, USA) using Olympus OMCL-AC160TS probes (nominal k = 42 N/m, nominal tip radius 10 nm) or CNF probes in air at RT. Image processing was performed with freeware Gwyddion (version 2.30, http://gwyddion.net/). Topography images were plane and line levelled, and then polynomial background removal was applied to remove particle curvature. 2D FFT filtering was used to remove line noise. Phase images were plane and line levelled only. This work was performed by Dr Rhiannon Creasey.

2.5.11 Optical Heating and Ignition of Fullerene-C60

2.5.11.1 Nd:YAG laser

A Continuum Sureline III Nd:YAG 1064nm laser was used at 450 mJ radiation. Detector card for steering adjustments of the laser was provided by Thor Labs.

2.5.11.2 Xe Camera Flash

A Luxtronics TUMAX DA880Z camera flash unit with a Xe source (λ_{max} approx. 500 nm) was used to excite particles subjected to 1064nm laser, where the experiment was performed sequentially afterwards (within the space of 2-5 minutes), with similar alignment to the Nd:YAG laser, incident on the sample.

Chapter 3| Organo-functionalised silica nanoparticles (SiNPs): Synthesis, analysis and modelling.

3.2 Overview

This chapter reports the growth and analysis of functionalised silica nanoparticles. Firstly, thiol functionalised silica nanoparticles are grown from (3-mercaptopropyl)trimethoxysilane (3-MPTMS) and thoroughly characterized. This method of particle growth is then extended to (vinyl)triethoxysilane, (propyl)trimethoxysilane and (3-cyanopropyl)triethoxysilane, where particle size is larger for species grown by these, than from 3-MPTMS. Analysis of particles grown from 3-MPTMS by NMR and use of computational modelling software shows a surface density of 4.7 thiols per nm^2. This demonstrates that thiol terminated silica nanoparticles show potential as a suitable platform for high density surface modification.

3.2 Introduction

In this work it is important to understand the composition and structure of the particle exterior. It is well understood that the number of hydroxyl groups on the surface of silica particles created from TEOS, however, the density of organofunctional groups that present on the surface, when an organosilane is used, without TEOS is not well known. A variety of methods exist to create functionalised silica nanoparticles, as discussed in Chapter 1, where the functional silane is either added at the start of the reaction, or after particle nucleation has started. In the latter case, the introduced silane coats the surface of the particle. In all cases here-in the particle is grown from a functional silane only, and TEOS is not used at all. This is to ensure that high density of the organo group presents on the surface of the particle.

If condensation of each silanol group occurred at 100% a continuous network of SiO_2 such as that of crystalline quartz shown below in Figure 22 would result, where the central white silicon atom is coordinated in a tetrahedral configuration to four red oxygen atoms.

This creates a highly dense SiO_2 framework, where the absolute cell lengths for quartz (1 atm) are 0.491 33 and 0.540 53 nm. A 2 x 2 cell structure in the x-y plane is shown below, which is approximately 1 nm by 1 nm, and results in an average of 11.3 surface (or near surface) silicon atoms per nm^2.

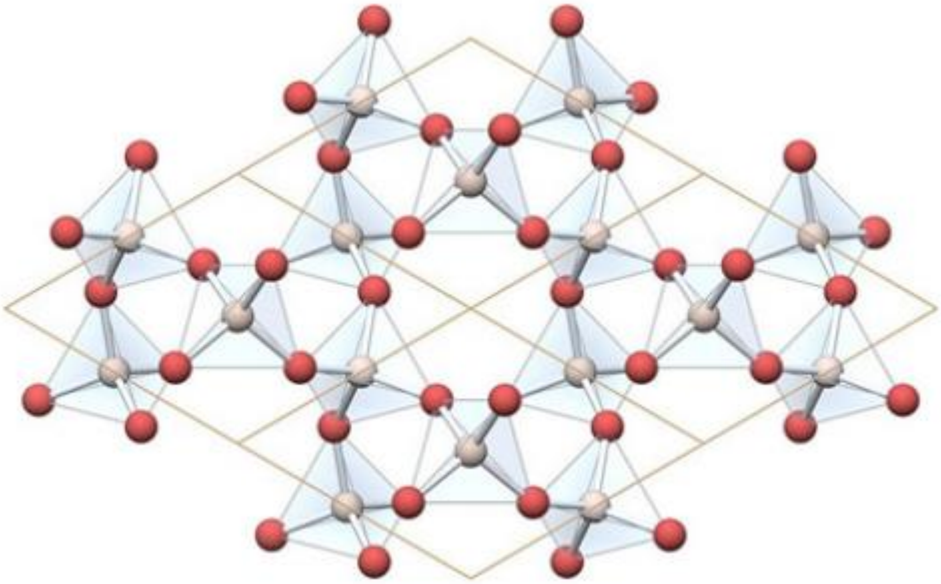

Figure 22: A 2 x 2 diagram of the repeating crystal structure of quartz (SiO_2)

3.3 Growth of thiol-functionalised silica nanoparticles

It is understood that repeated SiO_2 structures can be highly condensed repeating networks such as that of quartz (Figure 22) however, structures formed from the condensation of tetraethylorthosilicate (TEOS) will not form such a tightly packed system. In cases where silica structures (close to SiO_2) are formed synthetically (from TEOS), the Zhuralev Constant is an accurate measure of the number of surface hydroxyl groups, 4.5 +/- 0.5 hydroxyls per nm^2 as discussed in Section 1.2.5.1.

For particles produced from trialkoxyfunctionalised silanes with a hydrocarbon arm, such as (3-mercaptopropyl)trimethoxysilane (3-MPTMS), shown in Figure 23, where only three alkoxysilane sites exist for the potential transition from Si-OH to Si-O-Si, in comparison to the four alkoxysilane arms in TEOS. The chemical structures of both MPTMS and TEOS are shown below in Figure 23, where the red alkoxy arms are potential condensation sites.

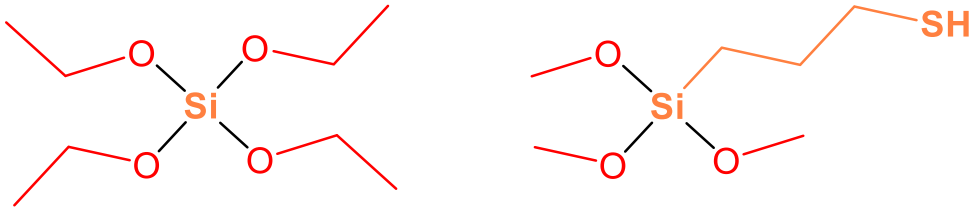

Figure 23: Structures of tetraethoxysilane (TEOS) and 3-mercaptopropyltrimethoxysilane (3-MPTMS).

To form thiol bearing organosilanes to grow spherical functional particles on the μL scale, a method was proposed by Nakamura and Ishimura.[65] The results of this process are shown below in Figure 24, where a distribution of particle sizes is displayed by electron microscopy for each concentration. Particles produced in the method below were grown in a system subject to occasional stirring within a 1 to 3 day time block, and were performed within the confines of an Eppendorf® tube.

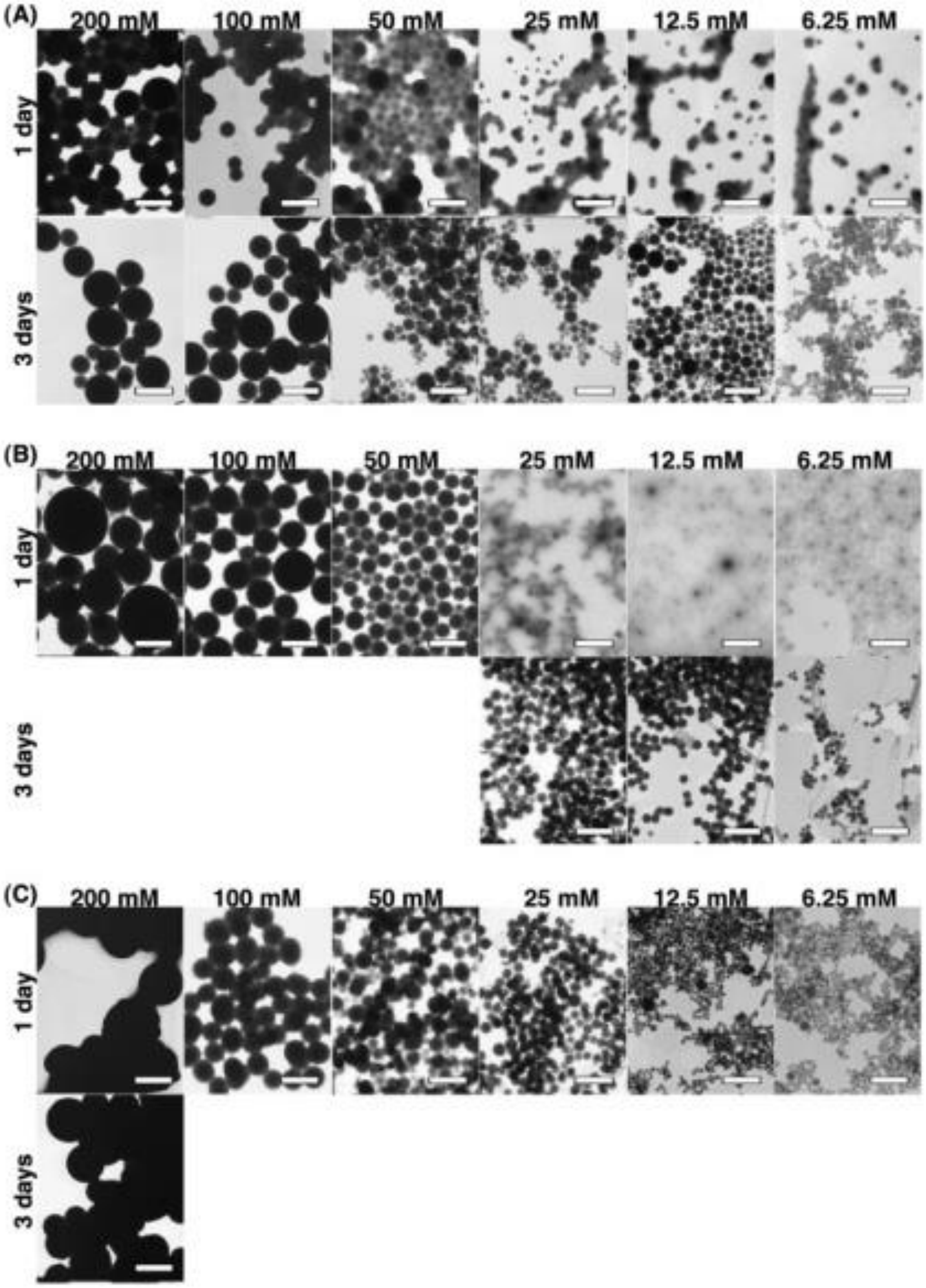

Figure 24: Particles produced from 3-MPTMS as the sole silane source[65]

To increase the quantity of nanoparticles prepared by this method, the reaction volume was increased 100 fold, from the proposed μl scale where homogenous mixing on the mL scale saw the formation of monodisperse particles. Figure 25 illustrates that upscale of the

Nakamura and Ishimura method can be used to add smaller, upscaled and monodisperse points (blue) to their existing particle regime (black points).

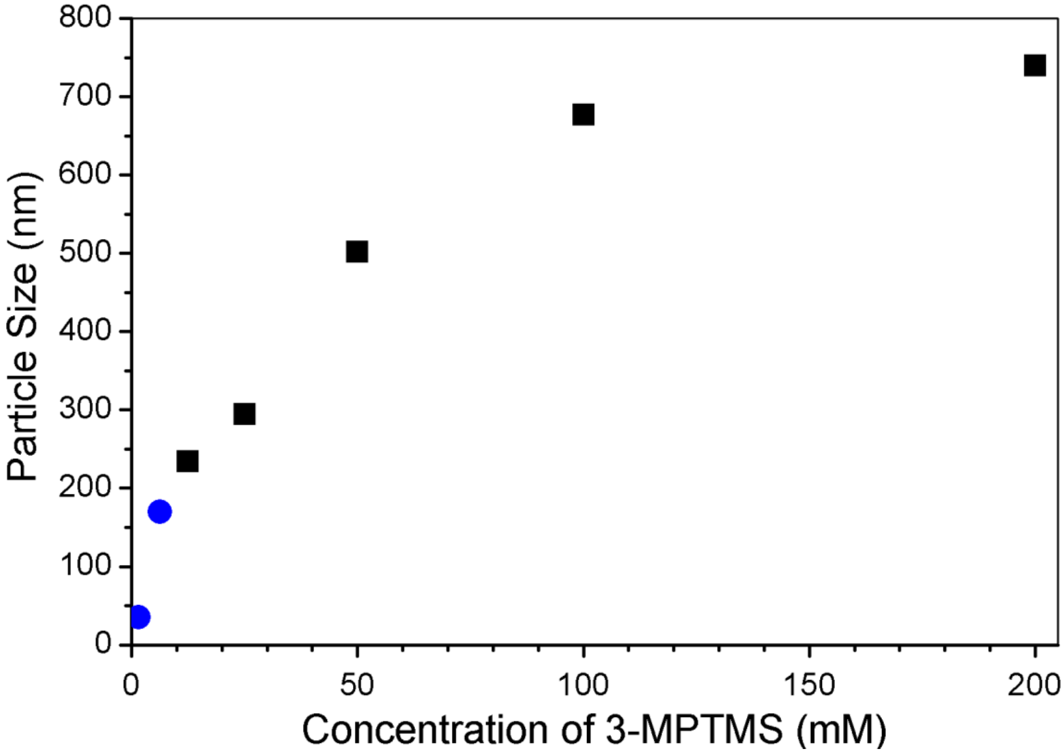

Figure 25: Extension of the relationship between silane precursor concentration and particle size (circles) to that of Nakamura and Ishimura's results (squares).

The average size of particles formed from the 3-MPTMS was measured using Dynamic Light Scattering (DLS) and Scanning Electron Microscopy (SEM). It can be seen in Figures 26 and 27 that both techniques provide the same particle size, on the order of 150 – 200 nm. The average particle size was determined to be 170 nm for particles synthesised from (3-mercaptopropyl)trimethoxysilane. Detailed information regarding the correlation data verifying the reliability of dynamic light scattering data can be found in Section 2.5.1.

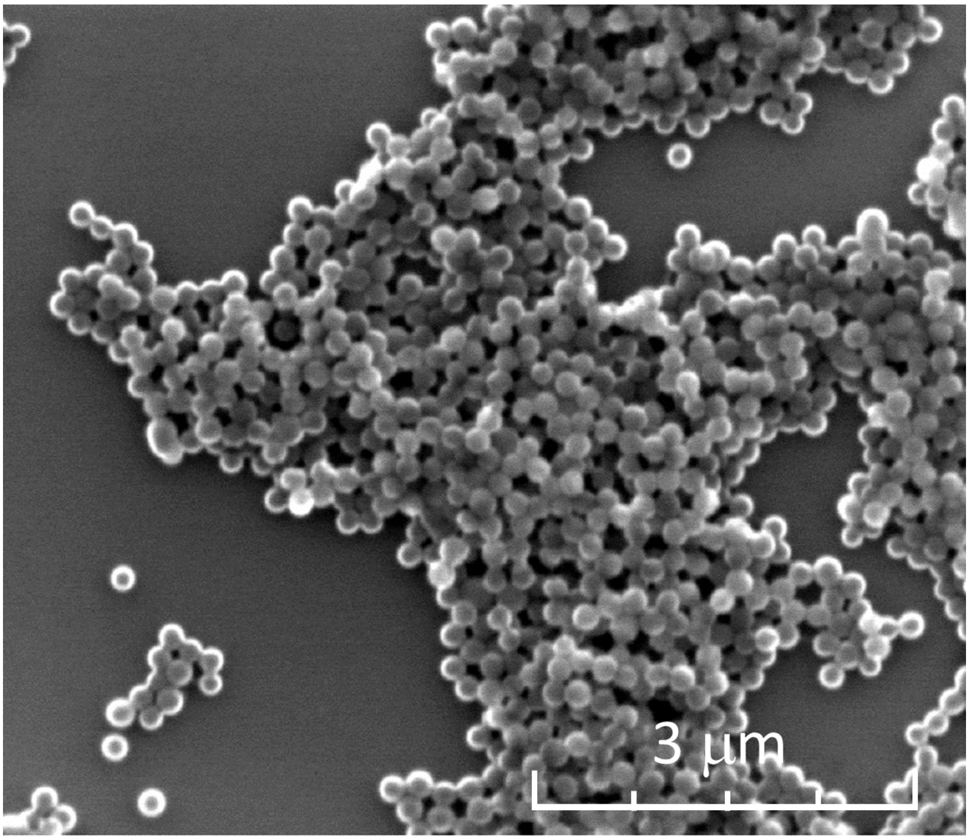

Figure 26: Silica nanoparticles imaged by Scanning Electron Microscopy

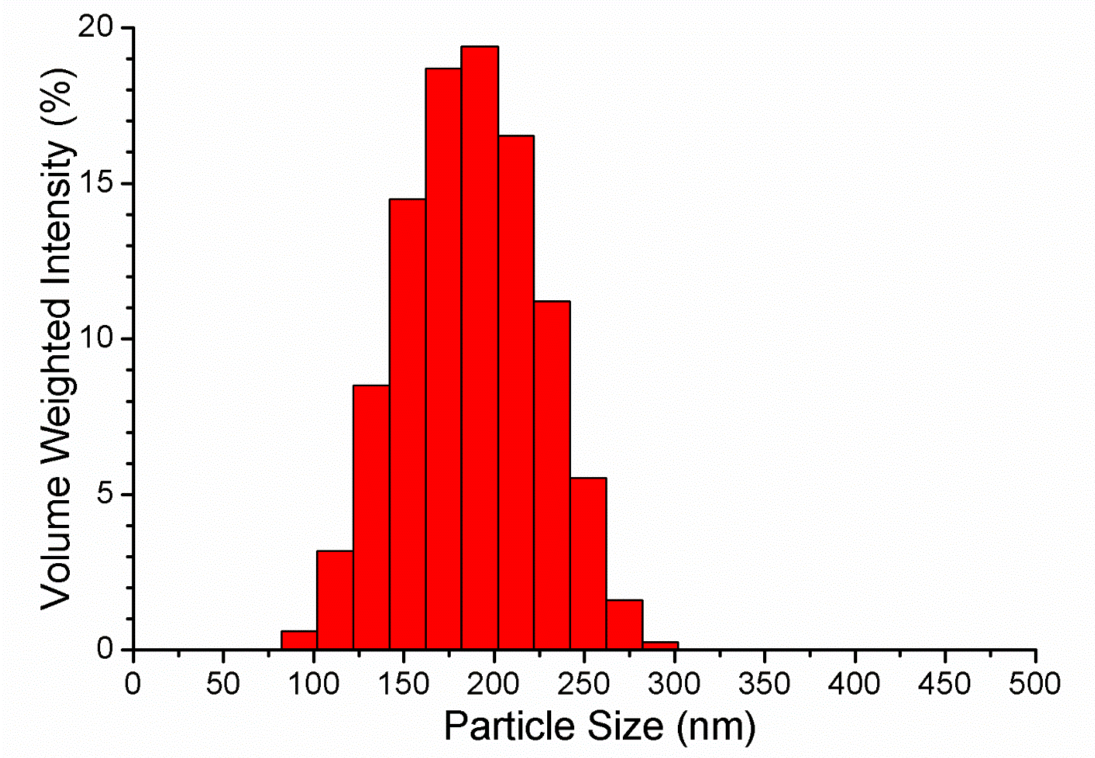

Figure 27: Silica nanoparticles measured by dynamic light scattering

The polymerisation of 3-MPTMS to create stable monodisperse particles is a three day process at room temperature, in contrast to TEOS, which will polymerise quite readily, within a manner of minutes or hours, depending on the conditions of the system (solvent and pH, to name a few). It was originally postulated that the unusually long reaction time for 3-MPTMS based particles is a product of the solubility of the propylthiol arm, and its potential for deprotonation under basic conditions (NH_4OH), in which the particles are synthesised (as described in Section 2.3.1)

3.4 Growth of organo-functionalised silica nanoparticles

Upscaled conditions discussed in Section 3.2.1 were then applied to other commercially available trialkoxysilane precursors such as cyanopropyl, vinyl and phenyl functionalised alkoxysilanes, which, similarly to 3-MPTMS, have three alkoxysilane sites for hydrolysis and polycondensation. These particles were polymerised through the same single step processing conditions, as described in Section 2.3.2.

The upscaled volume method to produce thiol terminated silica nanoparticles was extended to produce spherical particles out of other commercially available silanes, namely (vinyl)triethoxysilane, (phenyl)trimethoxysilane & (3-cyanopropyl)triethoxysilane. The conditions are shown below in Figure 28.

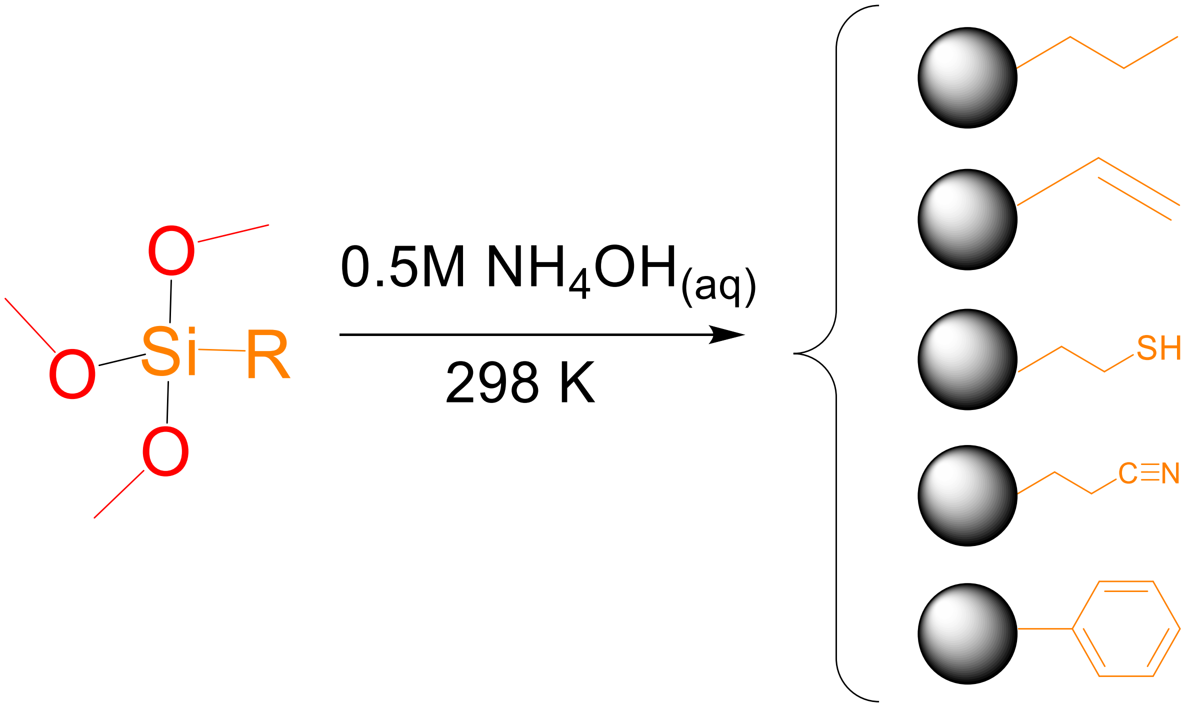

Figure 28: Conditions used to create spherical particles out of functionalized silanes

At the same initial organosilane concentration it is seen that the growth of particles from phenyl(trimethoxysilane) is much quicker than that of the vinyl, and cyano trialkoxysilanes.

This was determined by tracking the particle size in solution overtime, using dynamic light scattering, to measure the average particle size. The particle growth kinetics are monitored by DLS and SEM for the formation of particles from each functional silane, as shown in Figures 29 – 31 and Table 4. It can be seen below in Figure 29 that particles formed from the phenyl monomer are of a stable size within minutes, in comparison to particles formed from the vinyl and cyano monomers, which are shown in Figures 30 and 31 which take approximately 200 minutes to mature.

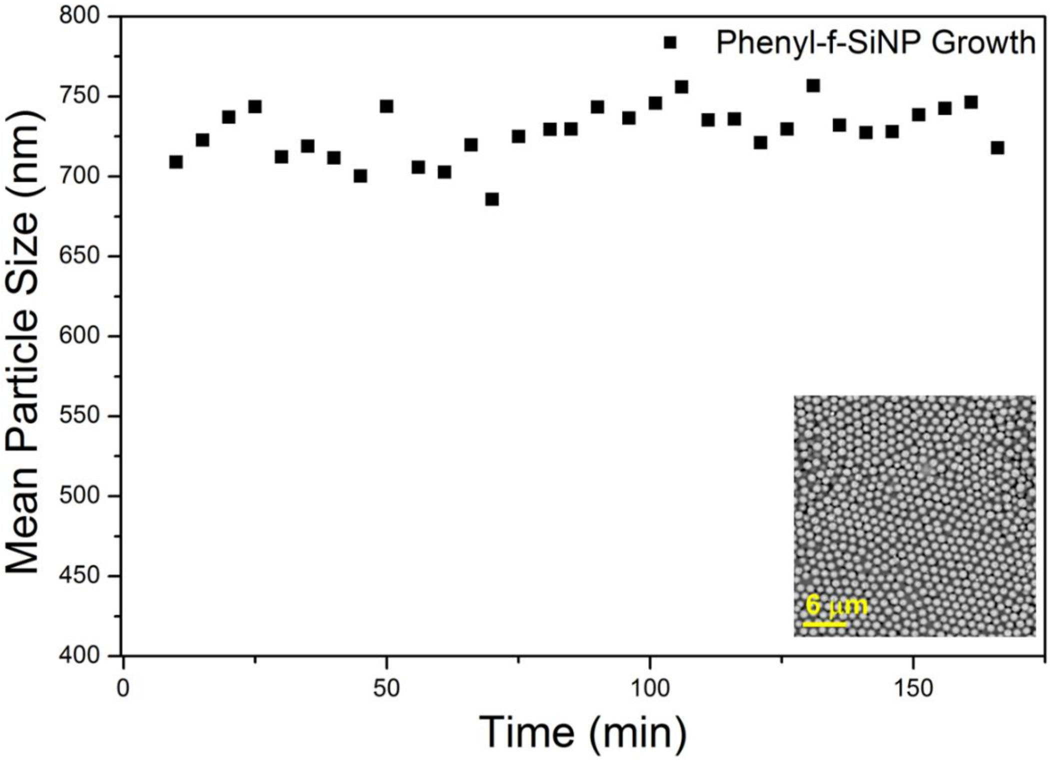

Figure 29: Growth of phenyl functionalised silica nanoparticles over time as tracked by DLS.

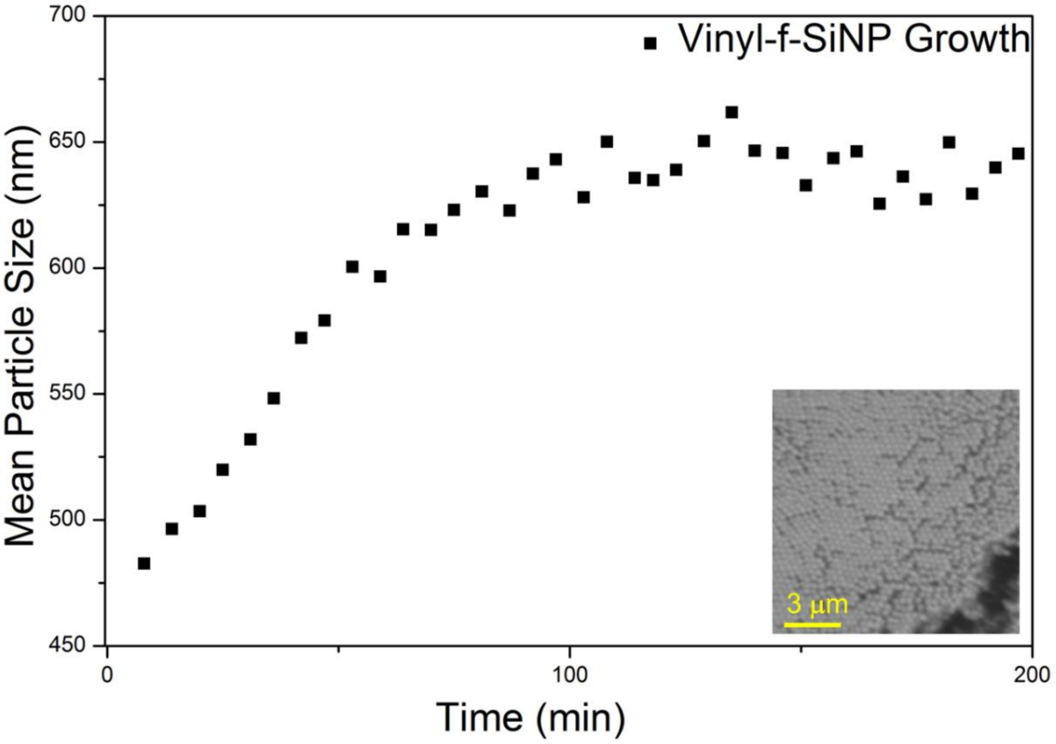

Figure 30: Growth of vinyl functionalized silica nanoparticles over time as tracked by DLS.

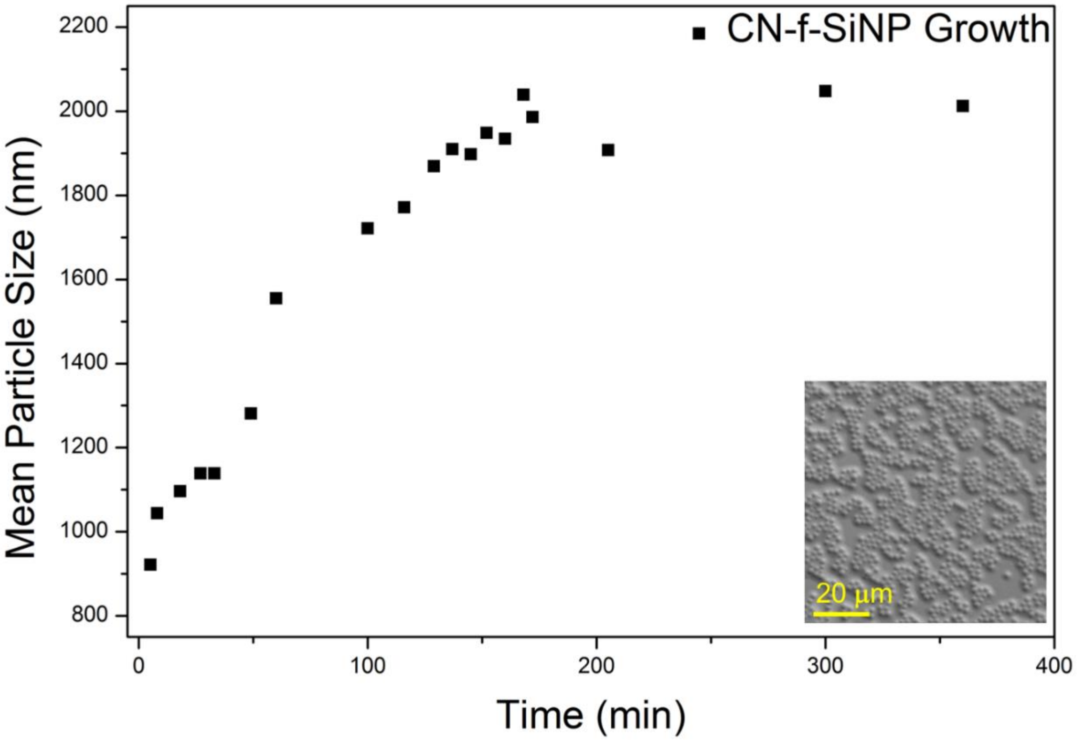

Figure 31: Growth of cyano functionalized silica nanoparticles over time as tracked by DLS.

Table 4: Maturation of particles synthesised from phenyl, vinyl and cyano functionalised alkoxysilanes.

Organosilane	Concentration (M)	Maturity Time (min)	Particle Size (nm)
PTMS (Phenyl)	8.6×10^{-2}	2	725
VTES (Vinyl)	8.6×10^{-2}	110	650
CPTMS (Cyano)	8.6×10^{-2}	160	2000

It was discussed in Section 2.3.1 that the particles produced from 3-MPTMS required 3 days to reach a mature particle that could be isolated and cleaned, however, in the case of the other organalkoxysilanes used it was noted that particles formed within a matter of minutes. The non-soluble organosilanes forming particles within minutes is remarkable compared to the water soluble monomer 3-MPTMS forming particles after 3 days. This suggests that solubility could be playing a role in the mechanism of particle formation. This supports Nakamura and Ishimura's hypothesis that micelles of 3-MPTMS form before siloxane bond formation. It was noted in the case of 3-MPTMS, opacity was seen in the early stages of particle development, but no product could be isolated from the cloudy dispersion, unless left to mature for days.[65] It is sensible based on solubility, that 3-mercaptopropyltrimethoxysilane would take longer to reach a localised critical monomer concentration (which is a requirement for a nucleation event to occur) than the water-insoluble organosilanes.

For illustrative purposes, this interfacial concept is shown in a cartoon format in Figure 32, where in the case of the vinyl monomer (p = 0.903 g.mL^{-1}), the immiscible (opaque) layer is seen above the aqueous solution, and for the phenyl monomer (1.062 g.mL^{-1}) it is below the aqueous solution.

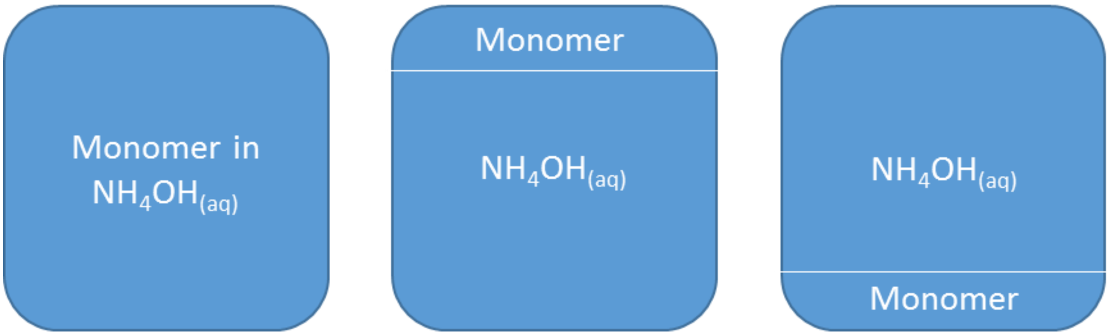

Figure 32: Different miscibility profiles of the reaction mixture pre agitation past 300 rpm

3.4.1 Concentration dependent growth of phenyl functionalised silica nanoparticles

Of all particle systems described above, it was found that only the phenyl system would demonstrate a change in particle size upon change in concentration of organoalkoxysilane. This relationship is illustrated in Figure 33 below, where it can be seen that as concentration of the phenyl monomer in solution increases, so does the resultant particle size.

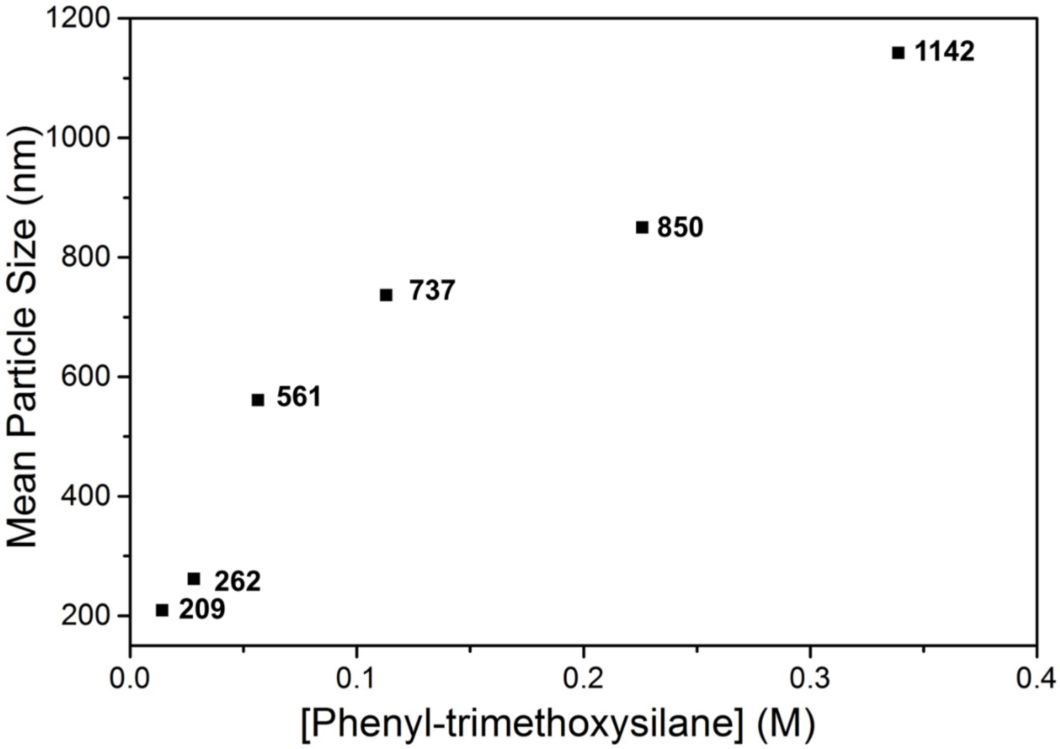

Figure 33: Resultant particle sizes from different concentrations of organosilane

The kinetics of particle growth for each concentration of monomer was tracked by DLS over time and is shown in Figure 34 below. This shows that at lower concentrations particle size is more stable than at higher concentrations, where it is seen that the particles which mature to 850 nm and 1142 nm fluctuate in measured size, at different time periods, where the correlation data looked quite normal for these samples.

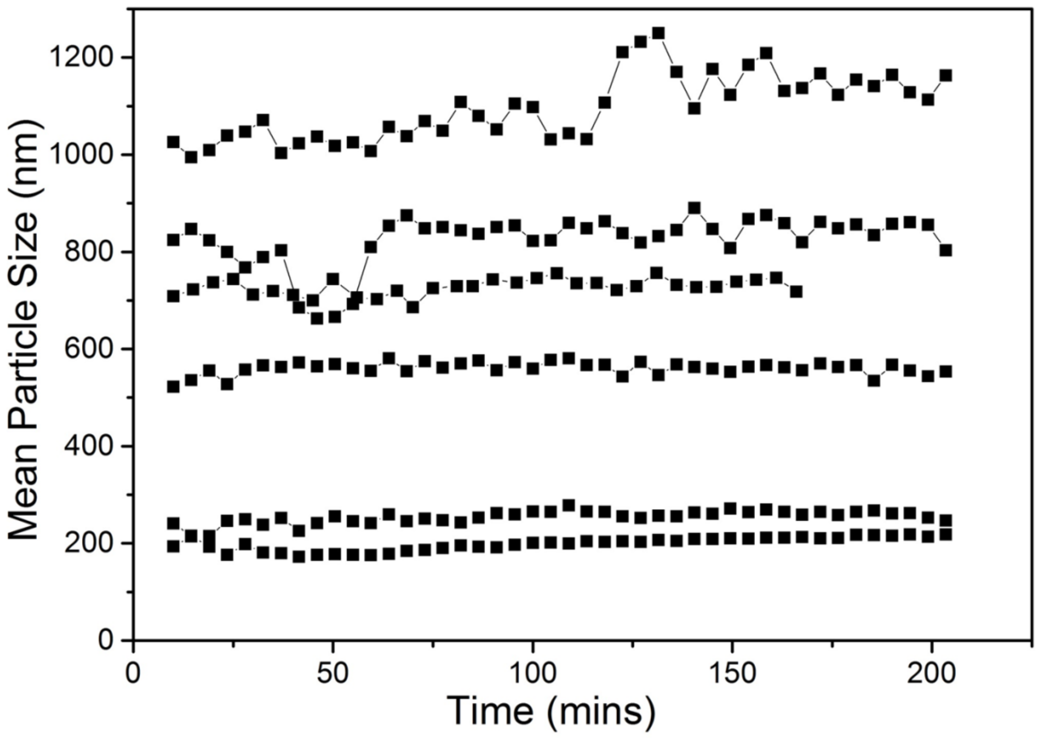

Figure 34: Kinetic data relating to mean particle size, measured by Dynamic Light Scattering

3.5 ^{29}Si-^{1}H cross polarization NMR of functionalised silica nanoparticles

The different particle systems were analysed using cross polarization ^{29}Si-^{1}H Solid State NMR, where it can be seen in Figure 35 that for all functional systems, the silicon nuclei are either fully condensed (Q_{Full}) or partially condensed ($Q_{Partial}$), where in the case of ($Q_{Partial}$) one silanol arm on the monomer has not completely condensed, only forming two Si-O-Si bonds, and leaving a dangling Si-OH bond.

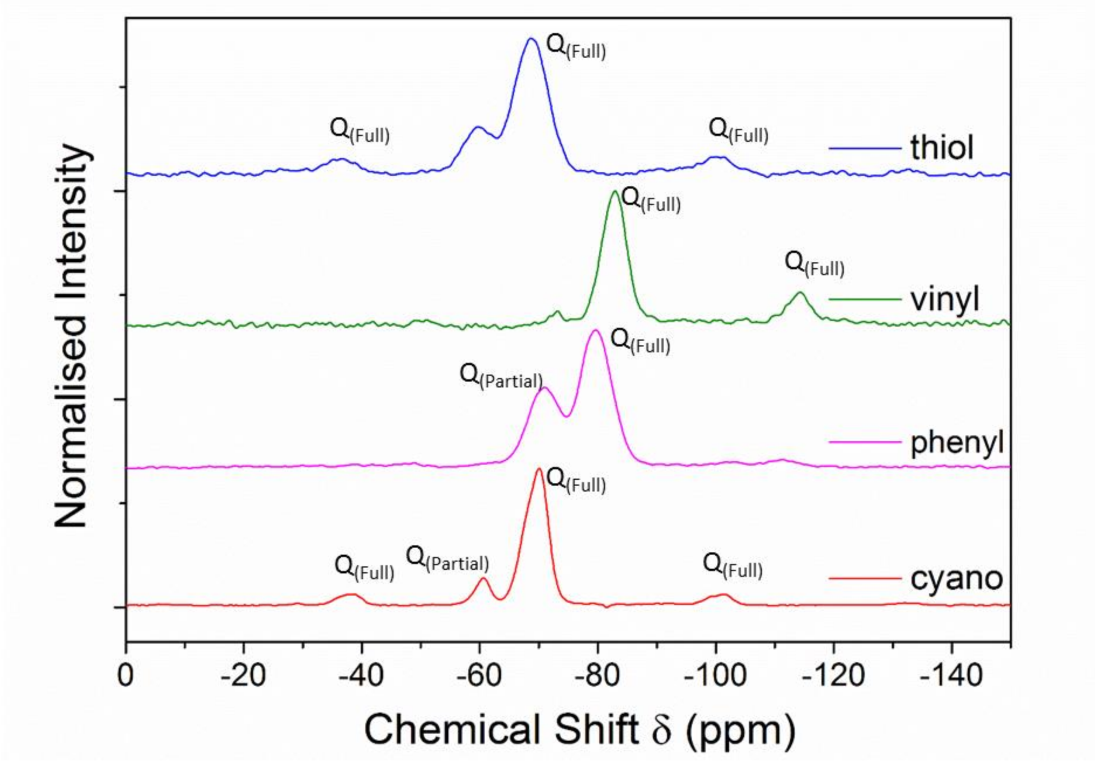

Figure 35: 29Si Cross Polarisation NMR of thiol, vinyl, phenyl and cyano functionalised particles. Where Q(Full) refers to a completely condensed silicon atom, and Q(Partial) refers to the silicon atom being bonded to one OH group (Si-OH).

It can be seen from Figure 35 that the chemical shift (resonant frequency) and therefor, relaxation time for silicon nuclei in Si-O-Si and Si-OH states varies quite significantly, depending on the nature of the 'organo' functional group. For the propyl functionalised silanes such as the cyano and thiol, there are similar shifts for the silicon nuclei, where the equidistant satellites that are symmetrical around the $Q_{(Full)}$ peak, a product of the cross polarisation process. Quantitative information regarding the condensation states for these silanes is shown below in Table 5. In order to quantitatively integrate the condensation states proposed by NMR, a contact time of approximately 3 times the relaxation time of the least sensitive nucleus was required.

Table 5: Nuclear information for different silicon environments

Monomer	Chemical Environment	T(Si)H (ms)	Chemical Shift (ppm)	Integration
MPTMS	Si-O-Si	1.2	68.62	11.38
	Si-OH	1	59.69	2.72
VTES	Si-O-Si	1.96	82.95	1
	Si-OH	Not Detected	Not Detected	-
PTMS	Si-O-Si	4.7	79.66	36
	Si-OH	3.2	70.98	13
CPTES	Si-O-Si	2.3	70.06	18
	Si-OH	1.9	60.64	2

The order of most to least condensed systems based on quantitative integration was shown to be Vinyl > Cyano > Thiol > Phenyl as shown in Table 6. There are a variety of different factors that could affect the reactivity and condensation rates of the silanol groups on the functionalised silica precursors, however, the solubility of the functional arm is believed to play the most significant role.

Table 6: Percentage conversion of silanol to siloxane determined experimentally by CP-NMR

Monomer	Conversion (%)
MPTMS	85
VTES	100
PTMS	91
CPTES	90

The difference in percentage conversion data could be due to physicochemical factors such as sterics, polarizability and solubility of the organic arm of the silane,, and the nature of the alkoxy arm, whether it be methyl or ethyl, which plays a major role in the efficiency of polycondensation which in turn, effects particle growth.

3.6 Extended analysis of thiol-functionalised silica nanoparticles

Thiol functionalised particles are investigated in detail throughout this thesis as a model platform for high density attachment to a particle surface. This section investigates the surface area available on the SiNP through gas sorption measurements, as well as consider an approximation of thiol molecules on the particle surface through computational modelling software

3.6.1 Determination of particle surface area

For a perfectly uniform, spherical dispersion of particles, the surface area can be determined from the particle diameter, however, non-uniformity in the size distribution or imperfections within the particle can impact the actual surface area.

The diameter determined by DLS and SEM was 175 nm and 170 nm leading to a surface area of 96,200 nm^2 and 90,800 nm^2 respectively, when calculated theoretically by $4\pi r^2$. However, the surface area determined experimentally, using nitrogen sorption studies, and the B.E.T. classification system, was determined to be 110,000 nm^2 per particle.

The surface area of SiNP was calculated by nitrogen sorption measurements, which provides a surface area as a function of weight. This provided a value of 21.7 m^2 per gram (compared to a calculated 18 m^2 per gram using $4\pi r^2$) which is consistent with the notion that these particles are not porous in nature.

Using the Brunauer-Deming-Deming-Teller (B.D.D.T) isotherm classification system, the gas adsorption of thiol terminated silica nanoparticles shows similarities to type III and V isotherms, where the sight hysteresis seen at higher relative pressures between the red and purple traces in Figure 36 is considered to be due to weak adsorbate-adsorbent interactions, which is indicative of a slight meso or macroporousity within the bulk sample. These results indicate a pore size of approx. 41 nm which would correspond to the space between the particles in a dried assembly of particles. This pore size indicates that the particles themselves are unlikely to be porous, where this void volume is an artefact of the sample preparation for isothermal analysis, where slightly elevated temperatures and low pressures are required to remove all residual solvent between the particles.

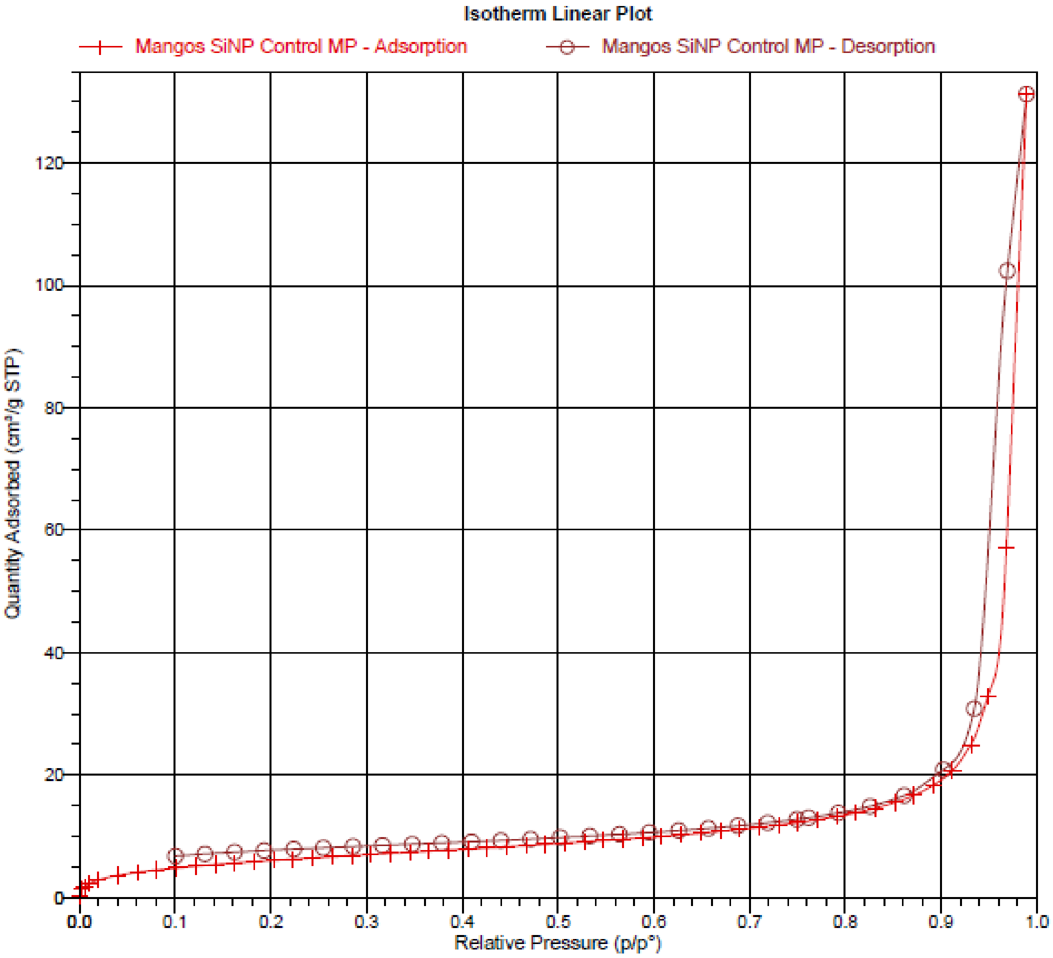

Figure 36: BET Isotherm of thiol functionalised silica nanoparticles

All calculations used here-in use the experimentally calculated value of 21.3 m^2 per gram as the surface area for a dried collection of 170 nm particles.

3.6.2 Computational Investigation into surface functionality development

Particle growth is complex and the development of surface functionality as a particle grows is critical for its ability to disperse and stabilize in the solvent. It is understood above that the growth of the thiol-terminated silica nanoparticle is unique, in comparison to other organofunctionalised silanes that have been explored in this study. The growth of a particle out of 3-MPTMS is explored by use of Materials Studio 8.0, where different generations of particle are considered in terms of the number of thiol atoms that can be seen on the surface, as a function of available surface area.

It can be seen below in Figure 37 that as the particle grows, the fraction of sulphur atoms available on the particle surface per unit area increases, and whilst this occurs, the particle transforms into a three dimensional structure. This representation of particle structure is known as a calotte model, where the sizes of the spheres are proportional to the radii of the atoms, the pink spheres represent the Si-O-Si backbone of the molecule, sulfur atoms are yellow, carbon grey, oxygen blue and hydrogens are white. Based on NMR data in section each generation an 85% probability of condensation based on the NMR results is applied to each hydroxyl group, all of which are equivalently considered as potential branching points. The blue 'wrapping' in the cracks between the atoms is the CPK is the van der waals approximation of the molecules surface area.

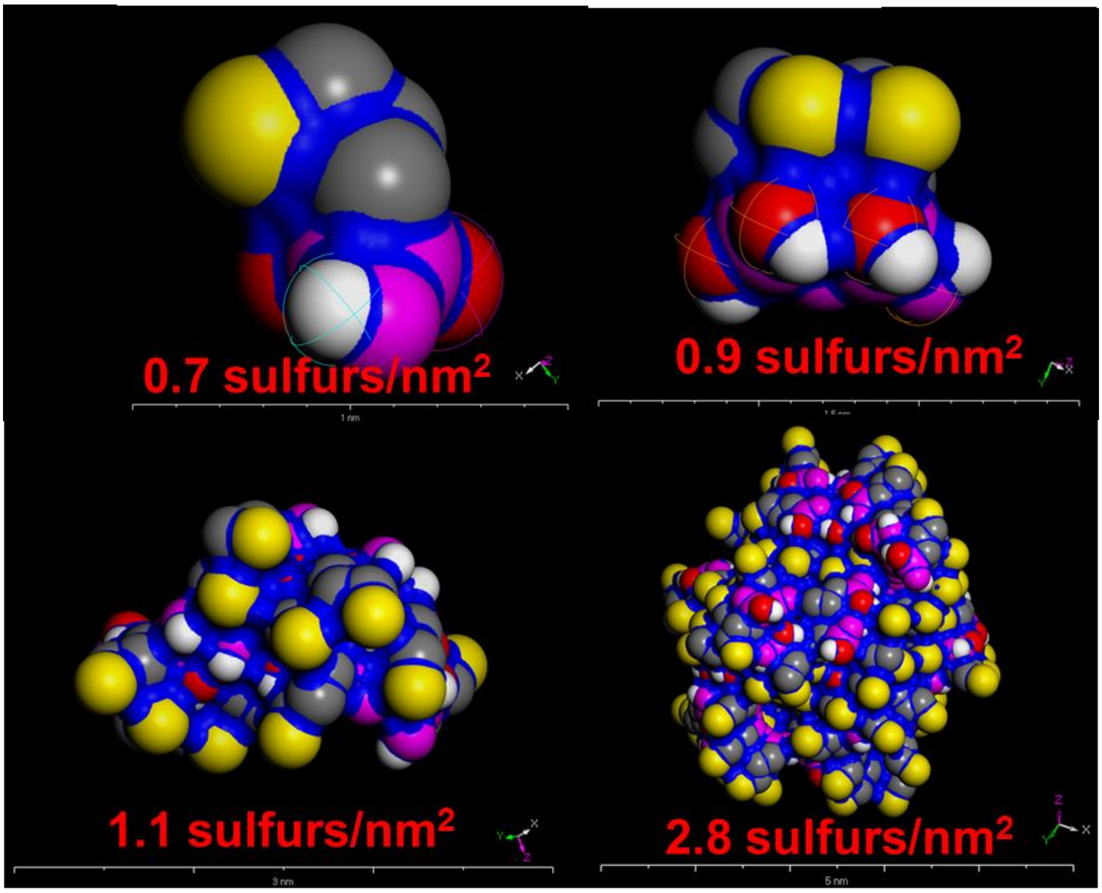

Figure 37: Growth of propylthiol functionalised siloxane network through Materials Studio Software Suite. The monomer, dimer, and following two generations of growth are shown.

The eighth generation of the particle process was the largest molecule that was able to be created by this system, which displays 4.7 thiols per nm^2 as shown in Figure 38.

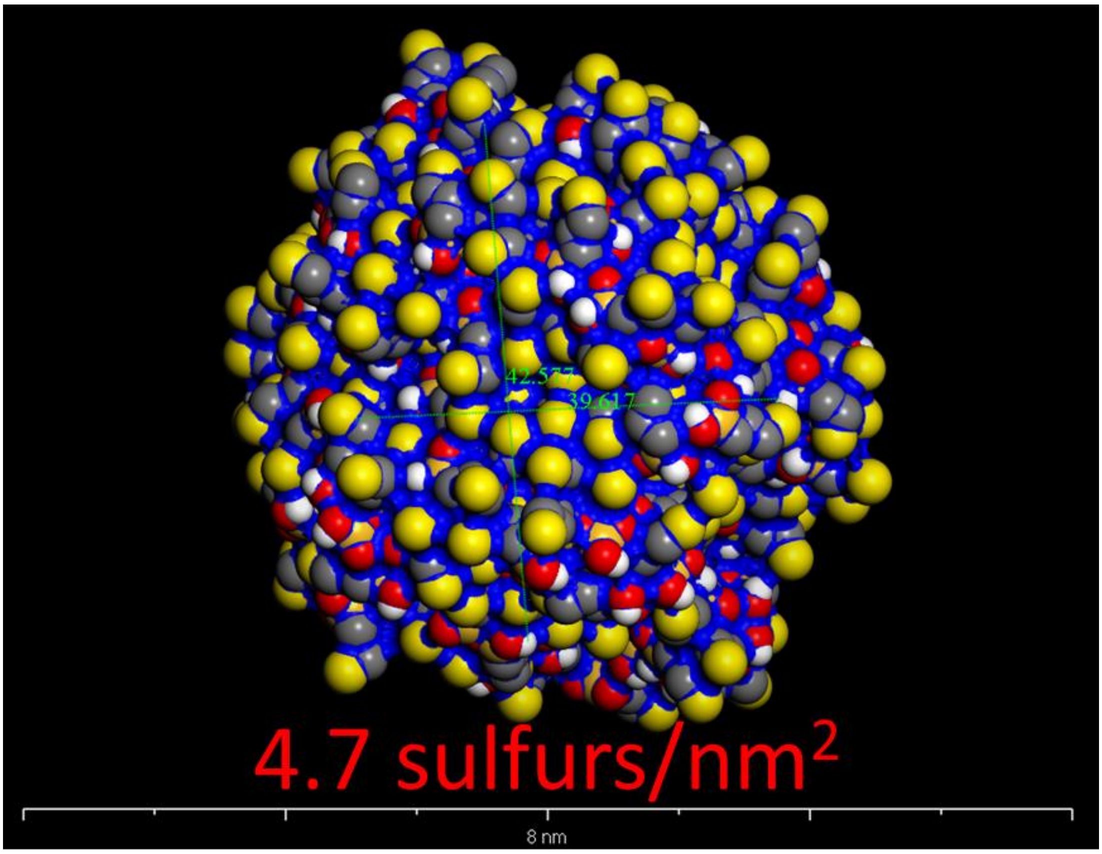

Figure 38: Generation 8 of particle grown from 3-MPTMS in Materials Studio 8.0

This value is representative of the growth of a free energy minimized siloxane polymer in a vacuum. Further optimization was attempted by solvating the Generation 8 particle with increasing weight fractions of water, in an amorphous cell, as shown below in Figure 39. It can be seen that with an increasing amount of water molecules, no significant change in particle geometry is seen, as is evidenced by the similarities between the radial distance between equivalent points in each hydration model. It can be seen that for each of these geometry optimisations for the amorphous cell, that the cell size increases significantly. Realistically for the system used, as described in

It can be seen below in Figure 39 that as an increasing amount of water molecules were included into a cell with the generation 8 polymer, the magnitude of the radius does not change significantly. There was also the concern that we are unable to account for water molecules trapped within the particle, from stages of it’s growth.

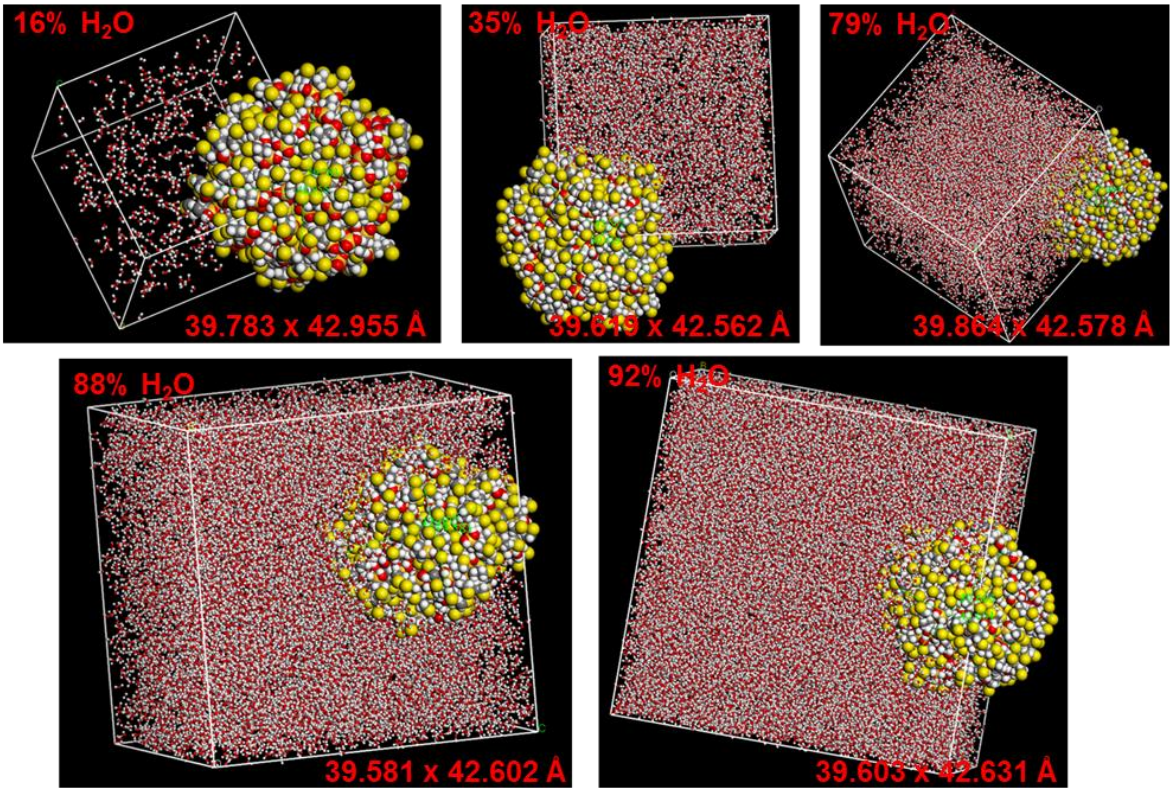

Figure 39: Hydration attempts on Generation 8 silica particle

To further optimise this structure, it is recommended that the free energy minimization used above be tailored to incorporate more detailed algorithms. Whilst parameters exist for siloxane based ‘inorganic’ polymers, they require modification to consider the van der waals and electrostatic coulombic forces associated with the introduction of the organic arm on the silica species, as well as solubility factors, and percentage of thiols deprotonated in the system. For the case of most computational methods this would require backend programming, which is beyond the scope of this thesis.

3.7 Conclusions

This chapter demonstrates the successful growth of spherical particles on the mL scale, using organo-functionalized trialkoxysilane monomers without the general reliance of TEOS for this process. Analytical techniques including DLS, SEM, and ^{29}Si-^{1}H NMR are used to determine the particle shape, size and average condensation structure, where it is seen that 3-MPTMS particles grow by a different mechanism than the non-polar functionalized silanes PTMS, CPTES and VTES, which form particles in minutes, in comparison to 3-MPTMS, which takes days.

Furthermore, modelling software was used to provide an intelligent approximation of the available thiols on the surface, where experimental data provided by cross polarised NMR coupled with computational modelling suggest a theoretical attachment density of 4.7 thiols per nm^2 upon formation of a semi-spherical structure, which is approaching that of the Zhuralev Model, which holds true for hydroxyl functionalised silica particles mentioned in Chapter One.

Chapter 4| Surface modification of SiNP through high density attachment

This chapter is based on work published in

Mangos, D., Nakanishi, T. and Lewis, D. (2014). A simple method for the quantification of molecular decorations on silica particles. ***Science and Technology of Advanced Materials,*** 15(1) pp. 015002.

4.1 Overview

This chapter builds upon the high density thiol presentation revealed from Chapter 3.Particles grown from 3-MPTMS can be used in a simple method to quantify attachment density on the thiol functionalised silica nanoparticle was developed. ATR-FTIR, was used as a quantitative technique where the Si-O-Si vibrational mode is used as an internal standard. With a large excess of 11-bromo-1-undecene, up to 4.9 molecules per nm^2 were able to be attached to thiol terminated particles by this method, where an attachment density of 5.7 molecules per nm^2 is suggested by thermogravimetric analysis. The rate of this attachment reaction is also investigated, with respect to time of UV Irradiation and concentration of 11-bromo-1-undecene.

4.2 Introduction

Chapter 3 showed that growth of a nanoparticle from 3-MPTMS can be achieved using Materials Studio 8.0, which indicated that 4.7 sulfurs are present per nm^2 of particle. As discussed in Section 1.2.5.1, attachment density for hydroxylated silica nanoparticles is generally accepted to be 4.6 ± 0.5 attachments (Si-OH) per nm^2.[57]

In this chapter thiol terminated silica nanoparticles created from MPTMS in the previous chapter are reacted with 11-bromo-1-undecene, and a calibration curve is created using ATR-FTIR to track the changes in oligo methylene stretching as a means to determine the attachment density. Free radical assisted Thiol-Ene chemistry used to modify the surface is shown below in Figure 40.

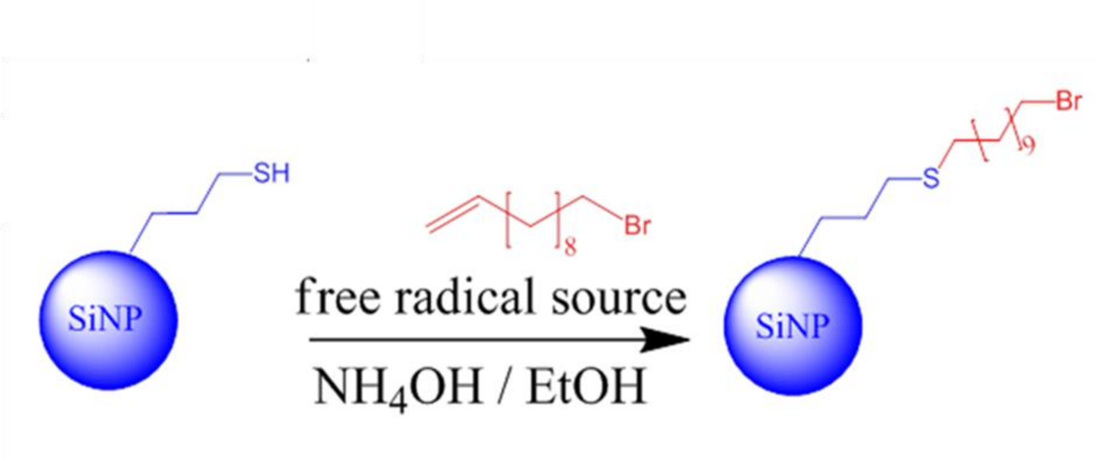

Figure 40: Attachment of 11-bromo-1-undecene to SiNP surface, by free radical assisted Thiol-Ene chemistry.

4.3 Tracking attachment to SiNP by ATR-FTIR

4.3.1 Formation of calibration curve

In order to accurately quantify the amount of 11-bromo-1-undecene attached to the surface of the particles during this reaction, a calibration curve was established using ATR-FTIR, which has been demonstrated to be a suitable technique for the tracking of vibrational modes with respect to an internal standard.[96-98] As shown in Figure 41 below, known volumes of 11-bromo-1-undecene, the alkene terminated reactant used in the Thiol-Ene reaction, was added to 13 mg of dry silica nanoparticle powder, homogenized via mortar and pestle and then transferred onto the ATR-FTIR plate for analysis.

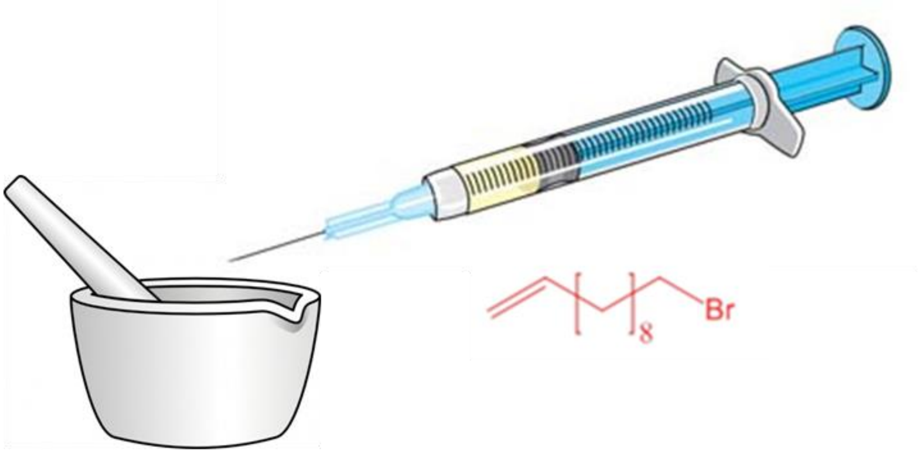

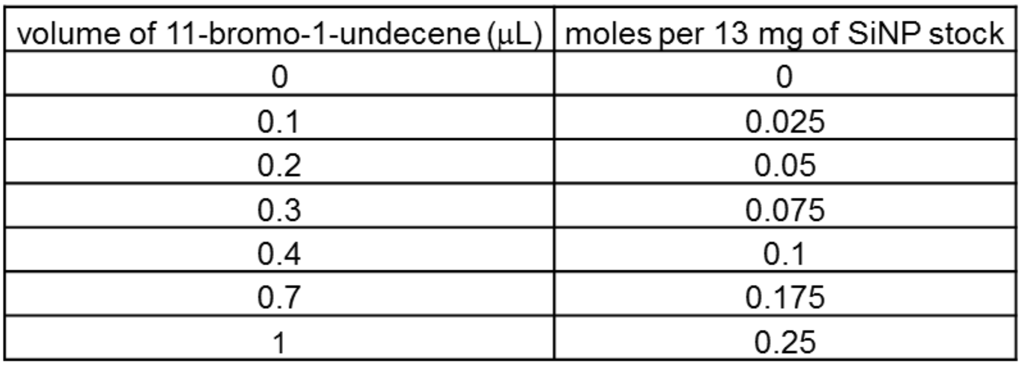

volume of 11-bromo-1-undecene (μL)	moles per 13 mg of SiNP stock
0	0
0.1	0.025
0.2	0.05
0.3	0.075
0.4	0.1
0.7	0.175
1	0.25

Figure 41: Formation of 11-bromo-1-undecene/SiNP slurry for ATR-FTIR analysis

As the concentration of 11-bromo-1-undecene increases in the slurry, the absorption of the oligomethylene ν(C-H) region, labelled A, in Figure 42 increases linearly, with respect to the ν(Si-O-Si) stretching vibration, labelled B. The Si-O-Si bending peak labelled B can be reliably used as an internal standard, as it is not involved in the functionalisation process. The oligo methylene (3008 – 2743 cm^{-1}) and siloxane (1215 – 831 cm^{-1}) peak heights are used as a ratio (A/B) where more resolved areas are highlighted in Figures 43 and 44.

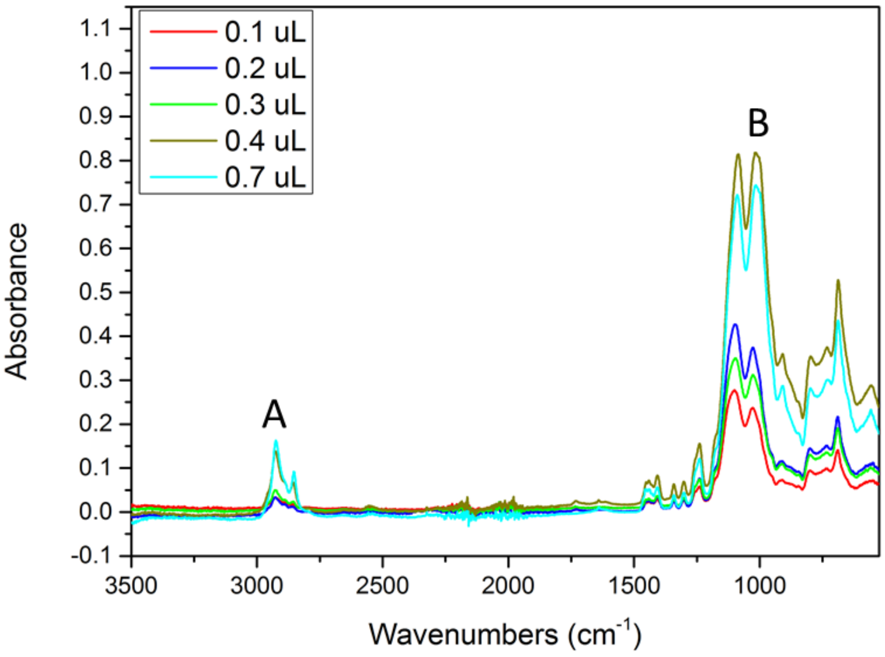

Figure 42: ATR-FTIR spectral overlay of homogenised additions of 11-bromo-1-undecene to SiNP

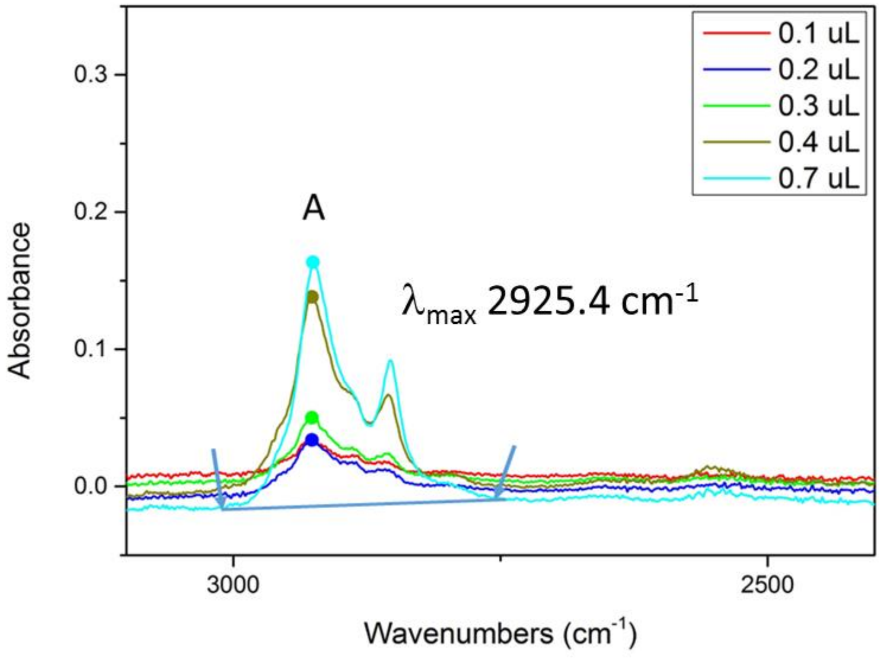

Figure 43: Zoom-in of oligomethylene region $v_{(C\text{-}H)}$ *3008 – 2743 cm*$^{-1}$

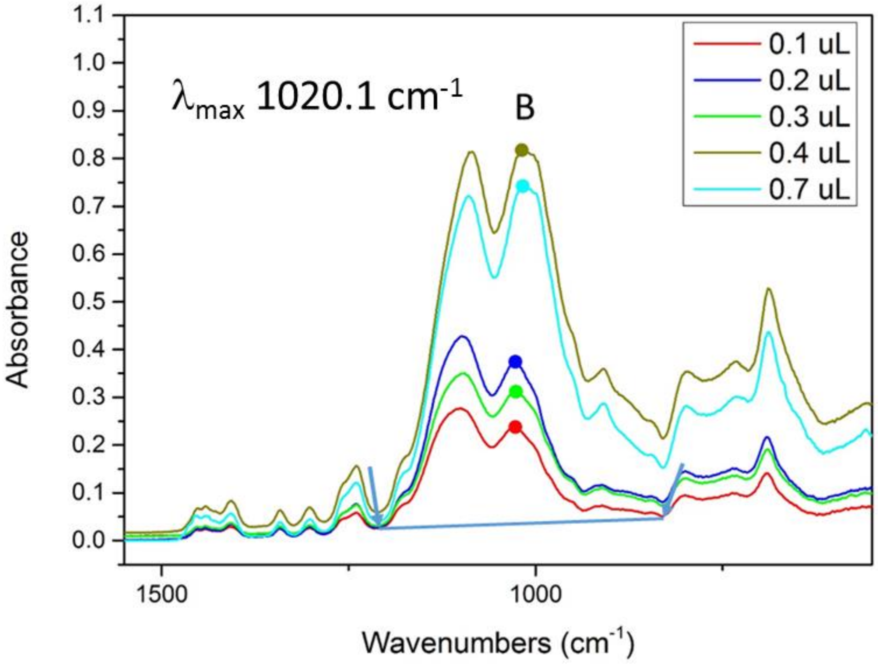

Figure 44: Zoom-in of siloxane stretching region ν(Si-O-Si) 1215 – 831 cm^{-1}

A calibration curve is shown below in Figure 45 where the ratio of A (the oligomethylene absorbance) to B (the siloxane absorbance) is seen to increase linearly with respect to concentration of 11-bromo-1-undecene added to the nanoparticle slurry. Where the slope of the graph is adjusted by 11/9 to account for the loss of the terminal double bond during the thiol-ene reaction, to create a further 2 sp^3 hybridized oligomethylene carbons, having the equation of $Y = 0.020x + 0.12$, where x is the number of molecules of 11-bromo-1-undecene in the matrix per nm^2 of surface area of silica nanoparticles.

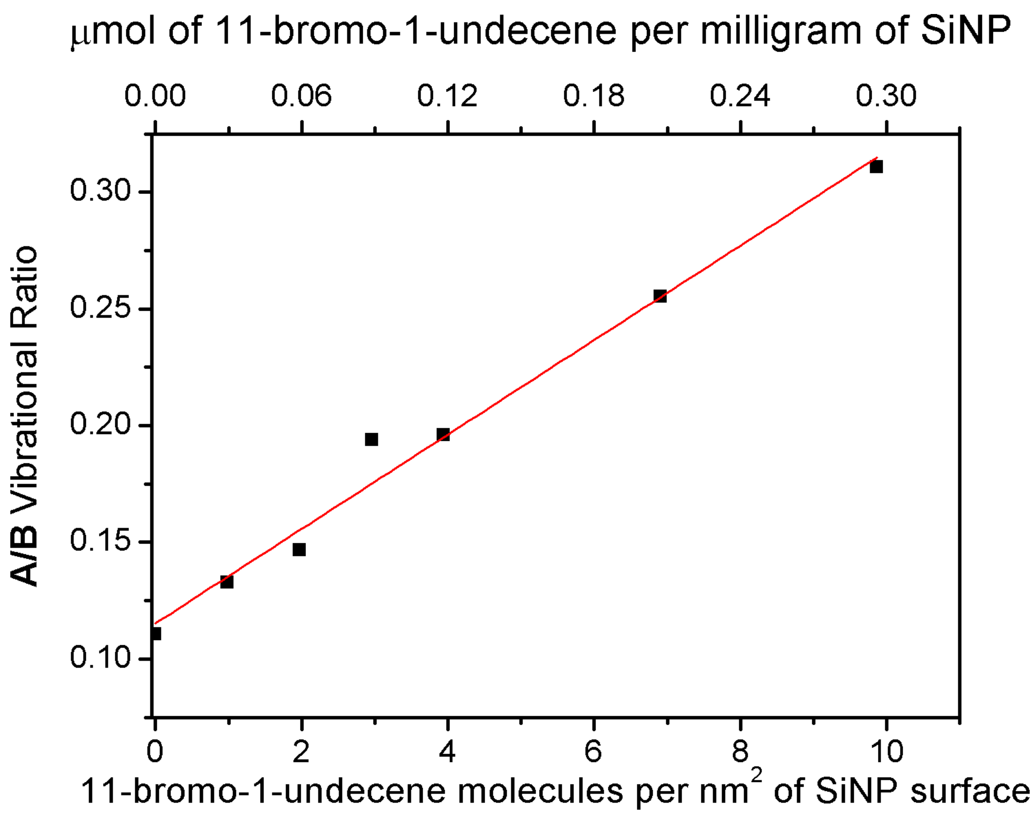

Figure 45: Calibration curve of addition of unattached alkene relative to surface area available, with a line of best fit, where error associated with measurement of A/B is ±0.05.

For each data point on the above graph, 13 mg of SiNP was mixed with the corresponding amount of 11-bromo-1-undecene as shown on the top x-axis. The representation of the x-axis in terms of molecules per nm^2 comes from converting the moles to number of molecules, and the weight of particles to amount of surface area available on the particle surface, determined by B.E.T which is discussed in Section 3.6.1.

The positive intercept on the y-axis in Figure 45 is due to the oligomethylene contribution of the propylthiol arm present for each silicon atom, which can be seen in the black trace of Figure 46, which shows the functionalised particle and reactants in an ATR-FTIR overlay. This shows comparative spectra to precursors SiNP in the red trace and 11-bromo-1-undecene in the blue trace. It can be seen in all traces that C-H stretching regions have reasonable absorbance for sp3 hybridised C-H stretching, and in the case of liquid 11-bromo-1-undecene, an extra C-H vibrational mode is seen around 3100 cm^{-1} owing to the terminal double bond.

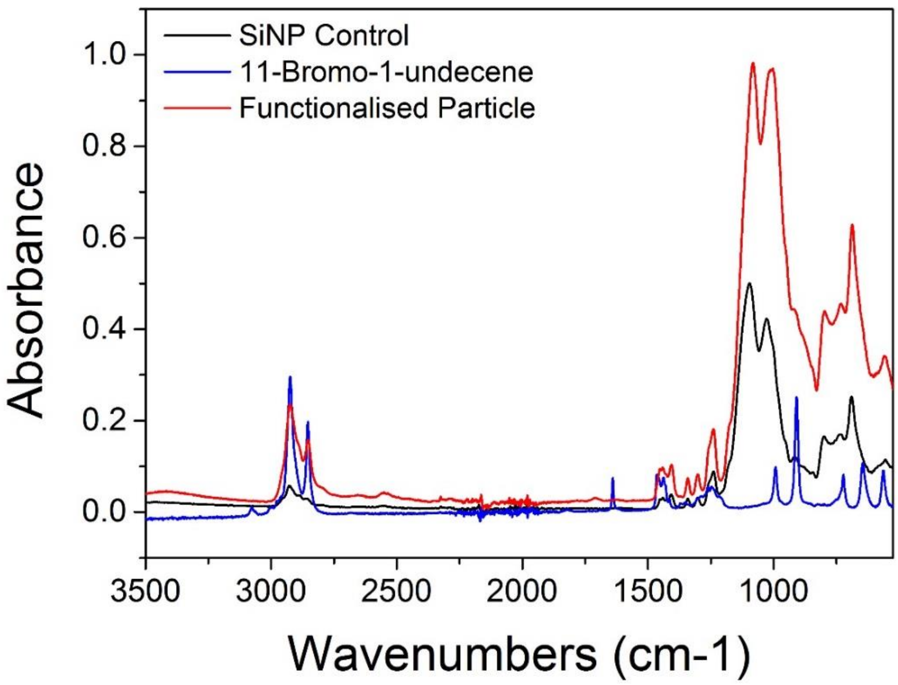

Figure 46: ATR-FTIR of SiNP, 11-bromo-1-undecene and functionalised particle

4.3.2 Attachment Kinetics

Using the A/B ratio, and its relationship to concentration of attached moiety, as evidenced in Figure 45, Attachment of alkenes to the particle surface was monitored with respect to irradiation time and concentration of alkene in the system. It can be seen in Figure 47, that after 60 minutes of irradiation time *(and a 730 molar excess of 11-bromo-1-undecene)*, no increase in attachment density is seen, past 4.9 attachments per nm^2. Given reacted sites increase the steric hindrance and thus, reactivity of the surface, it is sensible that remaining sites would take longer to react, as they would require a more specified orientation to react.

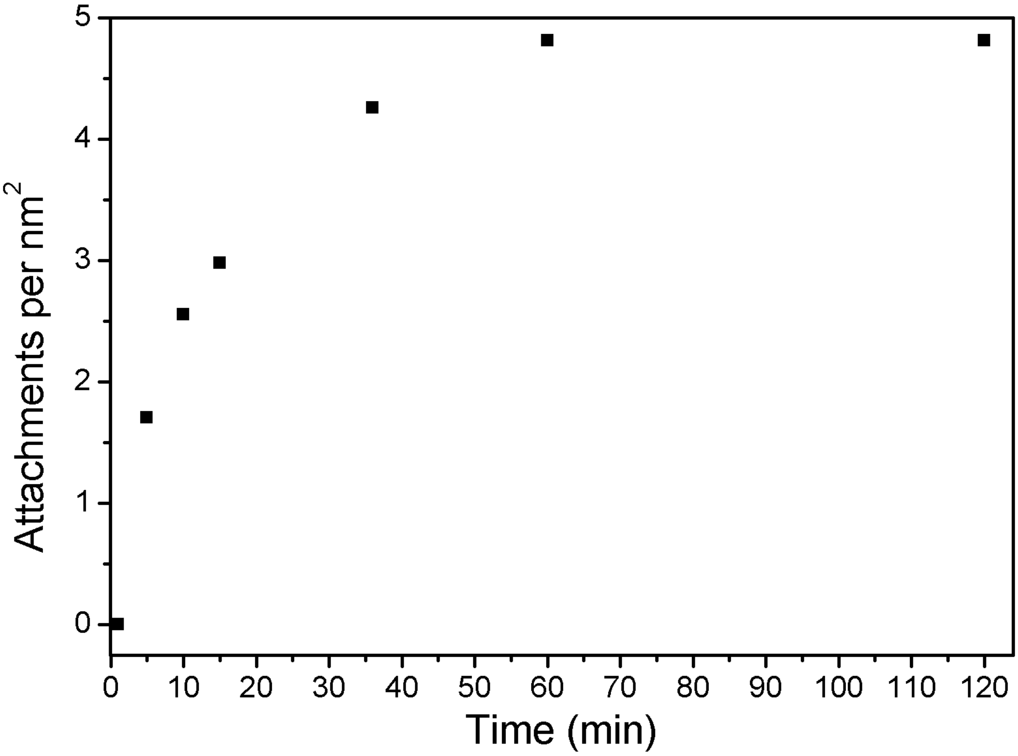

Figure 47: Rate of surface attachment for 1.75 mmol (730 molar excess) of 11-bromo-1-undecene under UV irradiation.

As seen above, a large excess of 11-bromo-1-undecene is necessary to reach a maximum attachment threshold of 4.9 attachments per nm^2. The impact of changing the concentration of 11-bromo-1-undecene in the solution is shown in Figure 48 below, which demonstrates the very large excess of alkene required, over stoichiometric addition, to see an increase in surface attachment.

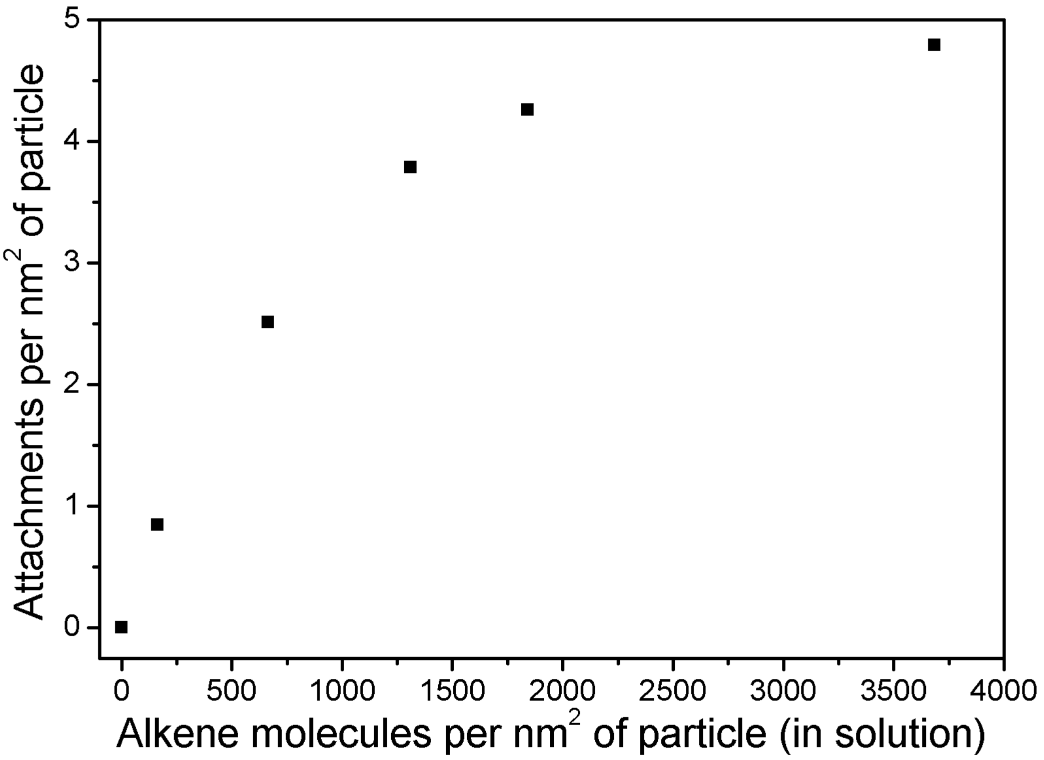

Figure 48: Controlling thiol-ene functionalization through excess 11-bromo-1-undecene added to system (reaction time: 60 minutes).

4.4 TGA as a comparative tool for attachment density

Thermogravimetric analysis was used as a complimentary tool to verify the attachment density determined by ATR-FTIR. Following the comparative weight loss plot in Figure 49, SiNP are stable to over 300 °C, whilst the particles functionalised with 11-bromo-1-undecene show a significant mass loss from 100 °C to about 250 °C. The mass loss in the 100 °C to 250 °C range for the functionalized particle is believed to be due to the loss of the covalently attached alkene, with the weight loss profile and similarities in decomposition of comparable organic species.[99]

TGA shows a mass loss of 4.4% of the total 5.046 mg due to the loss of the attached bromoalkane species, which corresponds to 1.0 x 10^{-6} moles. This value is then multiplied by Avogadro's number, which provides the number of attachments present, which is 6.0 x 10^{17} attachments. Given that the remanining 96.6% of the sample is SiNP then this mass (4.874 mg) is converted to surface area through the BET determined surface area of 21.7 m^2 per gram, which gives a surface area of .106 m^2 which equates to 1.06 x 10^{17} nm^2 of surface. This value of 6.0 x 10^{17} attachments divided by 1.06 x 10^{17} nm^2 of area gives a value of 5.66 attachments per nm^2

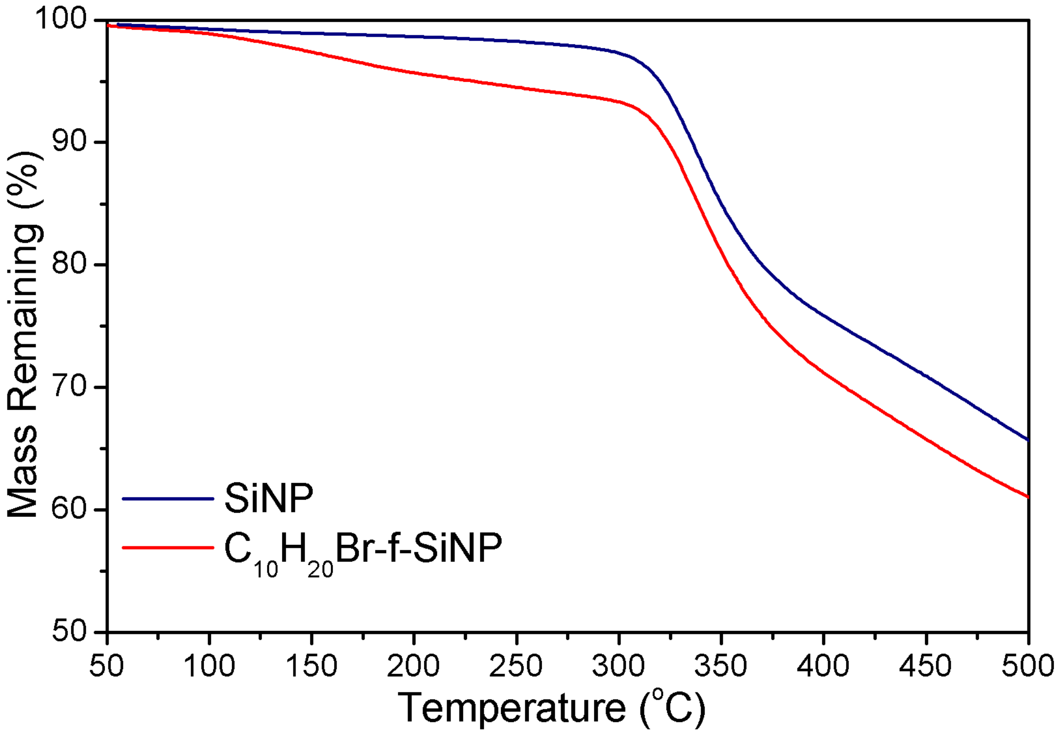

Figure 49: TGA of unfunctionalized SiNPs (blue) and 10-bromodecane functionalized SiNPs (red) prepared from a 1.75 mmol concentration of 10-bromo-1-decene.

The difference between the weight loss of the functionalized and non-functionalized SiNP is 4.4% at 290 °C. A mass loss difference of 4.4% for a 170 nm particle at maximum attachment density corresponds to 5.66 attachments per nm^2, which is similar to the attachment density determined by the ATR-FTIR analysis method above, and verifies the result provided by the FTIR analysis technique.

4.5 Conclusions

This chapter demonstrates that a maximum attachment density of approximately 4.9 attachments per nm^2 is achievable, through use of a simple ATR-FTIR calibration curve, used to quantify the functionalization density of hydrocarbons which are attached to thiol terminated silica nanoparticles, whilst gravimetric techniques suggest an upper threshold of 5.66 attachments per nm^2.

Furthermore, it is demonstrated that attachment density can be monitored as a function of reaction time, as well as concentration of alkene present in the solution. The difference between the weight loss of the functionalized and non-functionalized SiNP is 4.4% at 290 ˚C. A mass loss difference of 4.4% for a 170 nm particle at maximum attachment density corresponds to 5.66 attachments per nm^2, which is similar to the attachment density determined by the ATR-FTIR analysis method above, and verifies the result provided by the FTIR analysis technique.

Chapter 5| Formation and analysis of C_{60}-f-SiNP

5.1 Overview

This Chapter investigates the attachment of Fullerene-C_{60} to the particle surface to produce C_{60}-f-SiNP, following Chapter 4, which provided an understanding of the reaction conditions required for high density attachment. Small molecule chemistry between Fullerene-C60 and dodecanethiol was used as a comparative reaction to understand the chemistry of the adduct and prove covalent attachment in this work.

5.2 Introduction

The attachment of small particles onto large particles at a high density is the simplest bottom up process to creating what is referred to as a ‘raspberry-like’ particle structure. The surface structure of the particles is illustrated in Figure 50, where the smaller particle assembles onto the new surface. These new raspberry-like surfaces are hydrophobic, due to small air pockets created through the interaction of the two surfaces to create free or empty space.

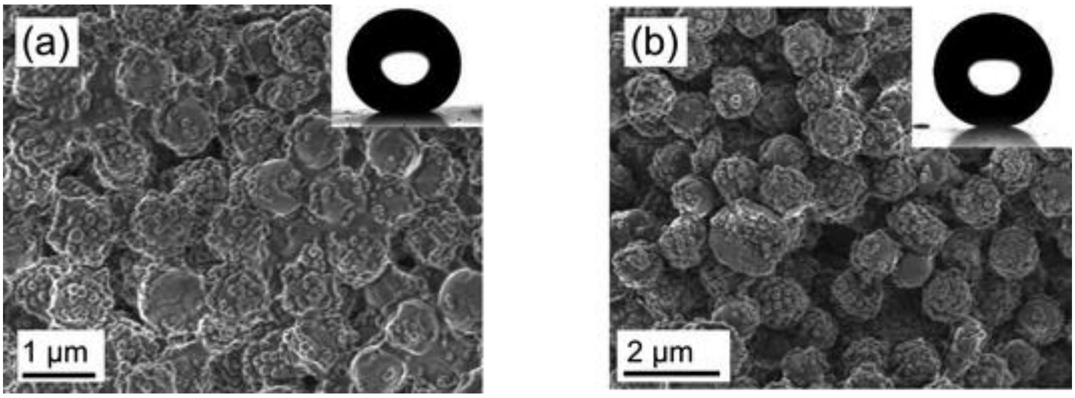

Figure 50: SEM micrographs of raspberry-like particle structures with inset contact angles .

In the case of small molecules or ‘particles’ such as Fullerene-C_{60}, the properties, such as conductivity of the smaller material, can be exploited through the close proximity of the molecules to one another, when tethered upon a surface. A recent example of Fullerene-C_{60} attached to a silica particle surface has shown potential as a photosensitizing agent[100], capable of producing singlet oxygen, with the capability to degrade and detect organic contaminants such as bisphenol A.[101]

Chapters 3 and 4 have demonstrated that high attachment densities, approaching the theoretical maximum could be achieved through thiol-ene chemistry on particles fabricated from 3-MPTMS, however literature suggests that the addition of a thiol to Fullerene-C_{60} is a reversible reaction, and further thiol-fullerene reactivity under similar mechanisms was quickly dismissed.[80] The radical addition of alkylthiols to Fullerene-C_{60} has been considered previously by electron spin resonance spectroscopy,[102] where it was seen that under photoexcitation by protons resulted in a reversible interaction between the two species, which was monitored for both methyl and ethyl sulphide radicals, where the structural chemical equation is shown below in Figure 51.

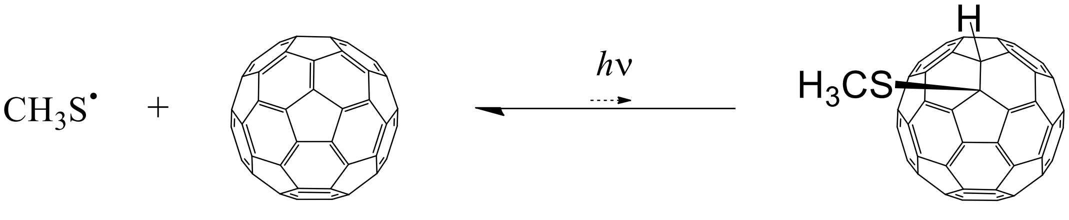

Figure 51: Reaction of methylsulfide with Fullerene-C_{60} to create an unstable adduct[102]

This chapter investigates the reaction of the thiol terminated SiNP (170 nm) with Fullerene-C_{60} (1 nm) to create raspberry like particles, using AIBN a thermal initiator, instead of *h*v. To verify the chemistry occurring on the particle surface, small molecule chemistry was performed, where the attachment between the thiol terminus of the SiNP is compared to a new reaction between dodecanethiol and Fullerene-C_{60}.

5.3 Formation of C_{60}-f-SiNP

The reaction conditions used to attach Fullerene-C_{60} to the SiNP surface are shown below in Figure 52 where a concentrated pellet of centrifuged SiNP was added to a warm solution of dichloromethane containing solubilized Fullerene-C_{60}. This starts of as a two phase mixture in the round bottom flask, then when refluxed under argon at 313 K (45°C) for 18 hours, forms a single phase.

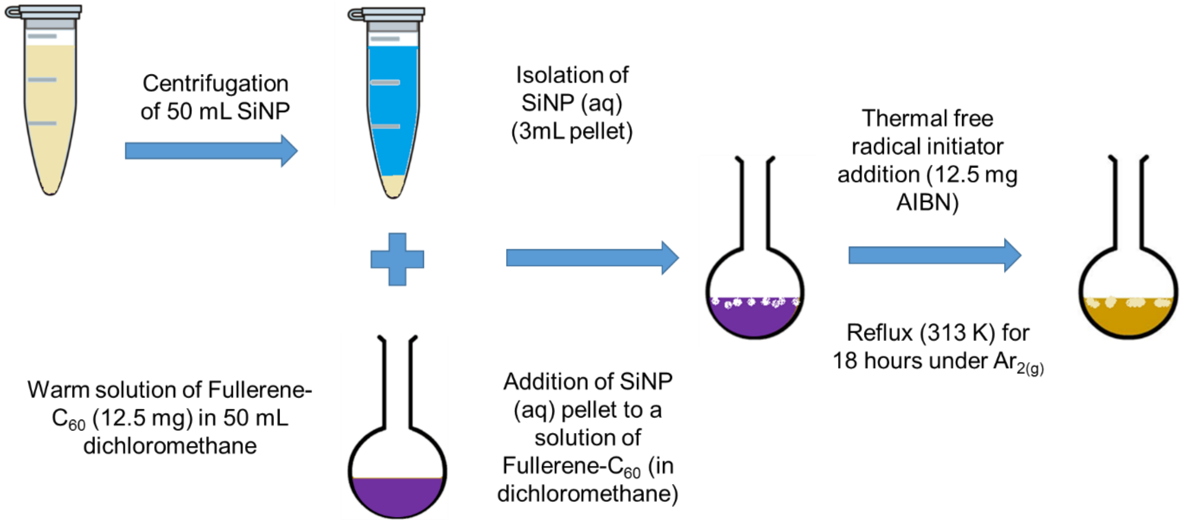

Figure 52: Synthesis of C_{60}-f-SiNP

The C_{60}-f-SiNP sample is isolated as a solid mass by centrifugation and washed thoroughly. This process occurs through resuspension in dichloromethane by a conventional vortex mixer, and washing through multiple times. This process was repeated multiple times to ensure a pure product was isolated for characterization. Figure 53 below shows the colour of the silica nanoparticles before (blue box of Figure 53) and after the reaction, where the brown particles (C_{60}-f-SiNP) in the red box are cleaned thoroughly, helping to ensure no physisorbed Fullerene-C_{60} is present.

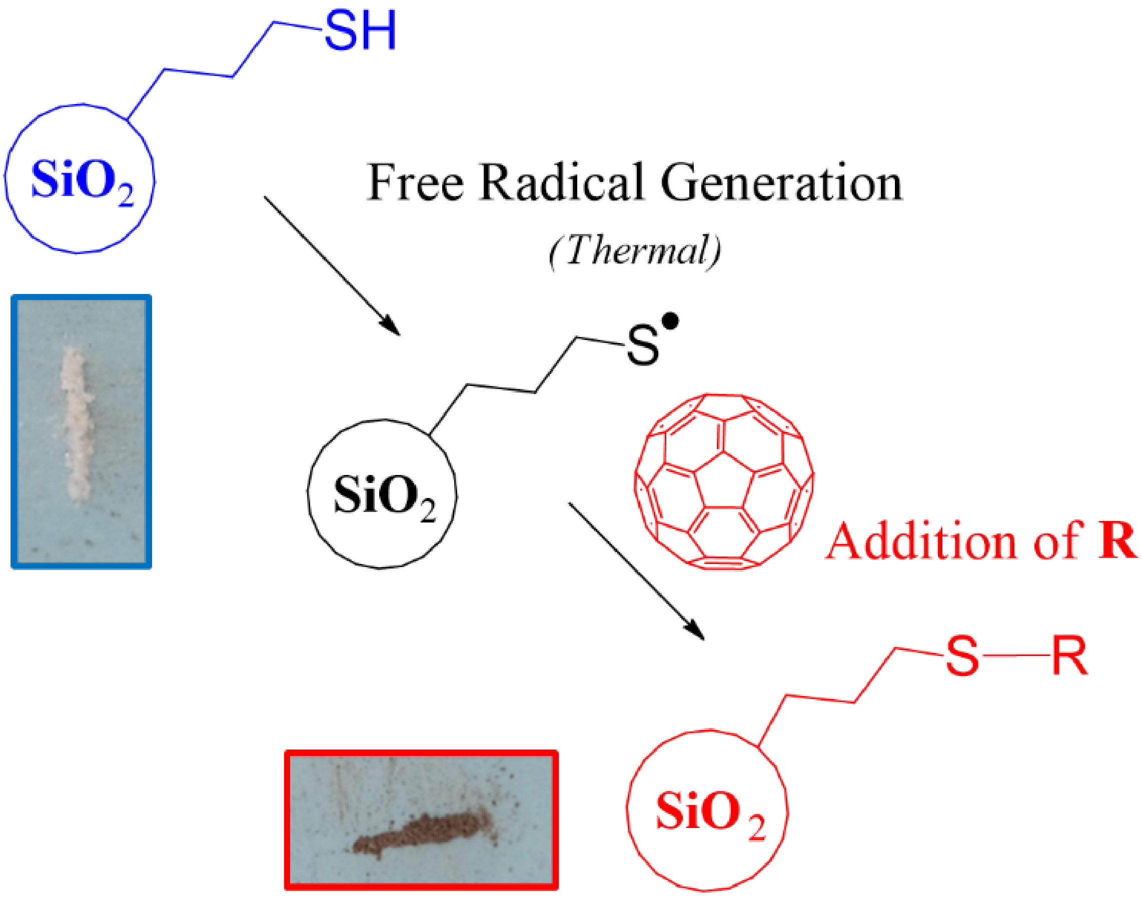

Figure 53: Mechanism of surface reaction through addition of thermal free radical generator (AIBN)

5.4 Characterisation of C_{60}-f-SiNP

To confirm the presence of Fullerene-C_{60} on the SiNP surface, the isolated C_{60}-f-SiNP product was analysed by a variety of techniques. These include ATR-FTIR, Solid State UV-Vis, MALDI-ToF-MS, TGA and AFM, which are discussed in separate subsections below.

5.4.1 ATR-FTIR Analysis

Evidence of chemical coupling to the surface of the SiNP can be seen by the change in dipole active modes of the two particulate samples, as shown in Figure 54. The loss of the *v*(S-H) stretching mode at 2250 cm^{-1} through the functionalization process supports the claim of covalent attachment of Fullerene-C_{60} to the particle surface, and the generation of peaks at 1660 cm^{-1} and 841 cm^{-1} that are unique to the C_{60}-f-SiNP sample are assigned to dipole active modes that occur when a sp^2 hybridised olefin is substituted.

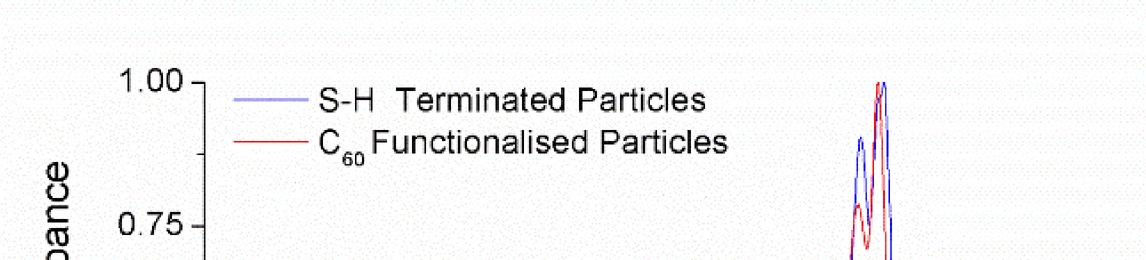

Figure 54: Infrared (ATR-FTIR) spectra of SiNP and C_{60}-f-SiNP

A zoom in of the MID-IR area of this spectrum is shown in Figure 55. This shows clearly the S-H stretch at 2553 cm^{-1} in the SiNP sample, which is not present in the C_{60}-f-SiNP sample. The formation of a peak at 1659.46 cm^{-1} is assigned to the formation of a C=C-H stretching mode, where Figure 56 shows a closer view of the fingerprint region of the spectrum for C_{60}-f-SiNP. It can be seen that a new peak is present with a weak absorption signal at 843 cm^{-1}, which is also characteristic of aromatic ring substitution.

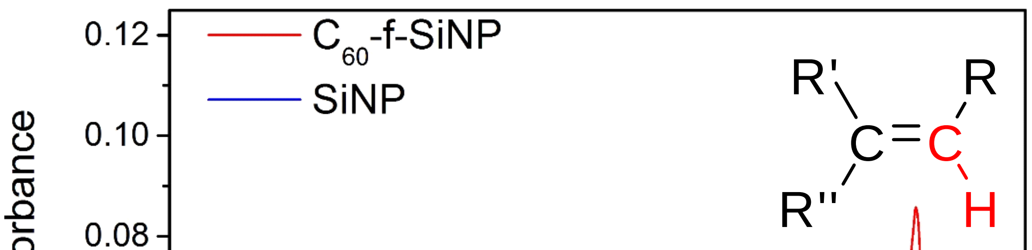

Figure 55: Zoom in of Figure 54 on MID-IR region for C_{60}-f-SiNP and SiNP

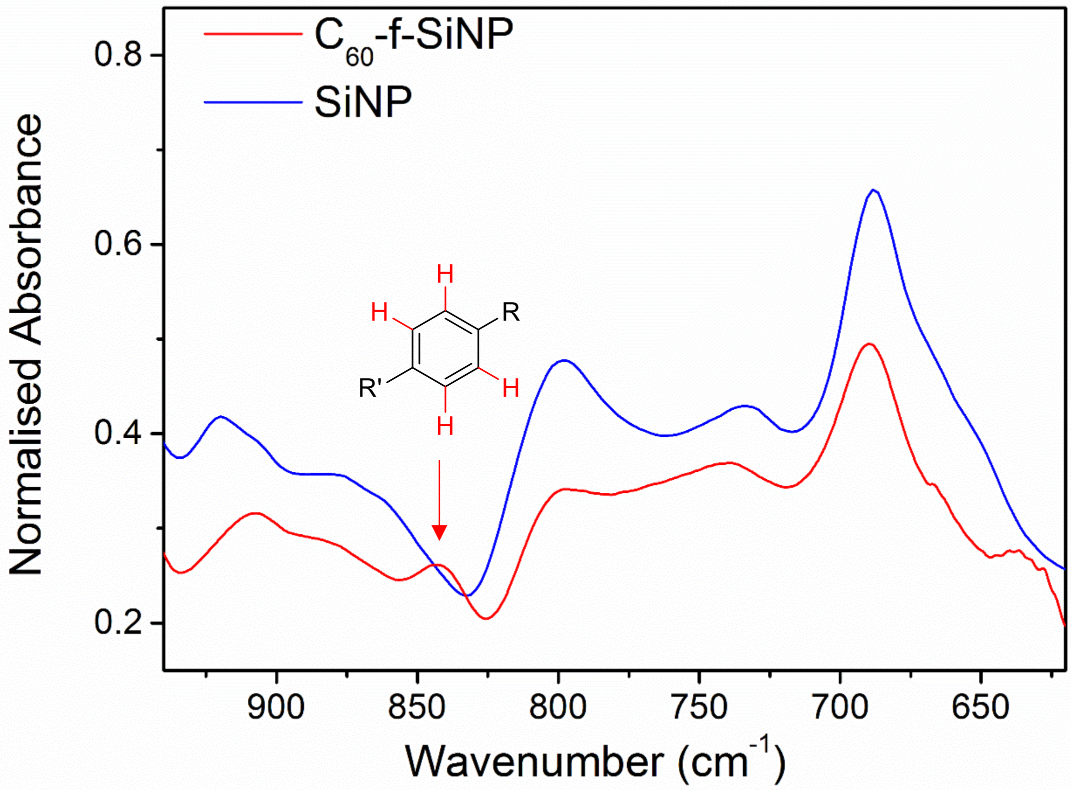

Figure 56: Zoom in of Figure 54, on Fingerprint region of IR for C_{60}-f-SiNP and SiNP.

5.4.2 Solid State UV-Vis

Importantly, the aromatic nature of the fullerene was not destroyed through the addition of Fullerene-C_{60} to the surface of SiNP, which can be seen in Figure 57 as the similar broad visible absorption characteristics exist for both the Fullerene-C_{60} and C_{60}-f-SiNP.

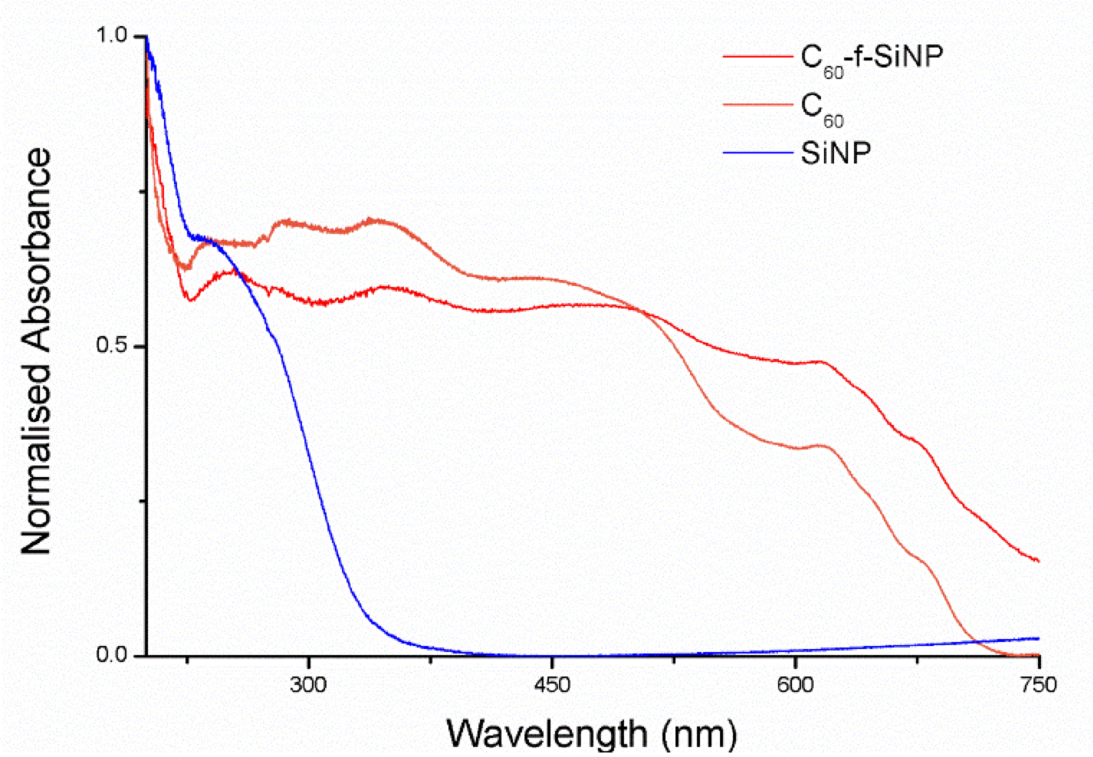

Figure 57: Solid State UV-Visible absorption spectra of C60-f-SiNP (red), Fullerene-C60 (orange) and SiNP (blue).

The blue trace in Figure 57 shows the SiNP is not photo-active in the visible region of the spectrum, as expected, allowing for spectral definition to show the fullerene structural characteristics are maintained in the C_{60}-f-SiNP.

A slight red absorption shift (10~50 nm) is seen in the C_{60}-f-SiNP sample, in comparison to pristine Fullerene-C_{60}, where the λ-max for the peaks shift from 240, 340 and 450 to 250, 350, and 500 nm respectively. Subtle differences in the absorption states between Fullerene-C_{60} and C_{60}-f-SiNP suggests that the electronic properties are slightly altered, which can be seen by the change in intensity of the peaks, as well as a change in peak position and would be expected since the fullerene is not “substituted”.

5.4.3 MALDI-ToF-MS

MALDI-ToF-MS is a commonly used tool in confirming the presence of Fullerene-C_{60} through its characteristic +720 m/z. In most cases Fullerene-C_{60} derivatives require an ablation or desorption matrix to liberate a charged ion from the surface (REF). As shown in Figure 58 below, a desorption matrix is not necessary in the case of C_{60}-f-SiNP, where the +720 m/z is a prominent peak, and is attributed to the molecular mass of the Fullerene-C_{60}, which is commonly seen in this ablation technique for Fullerene-C_{60} and is illustrated below.

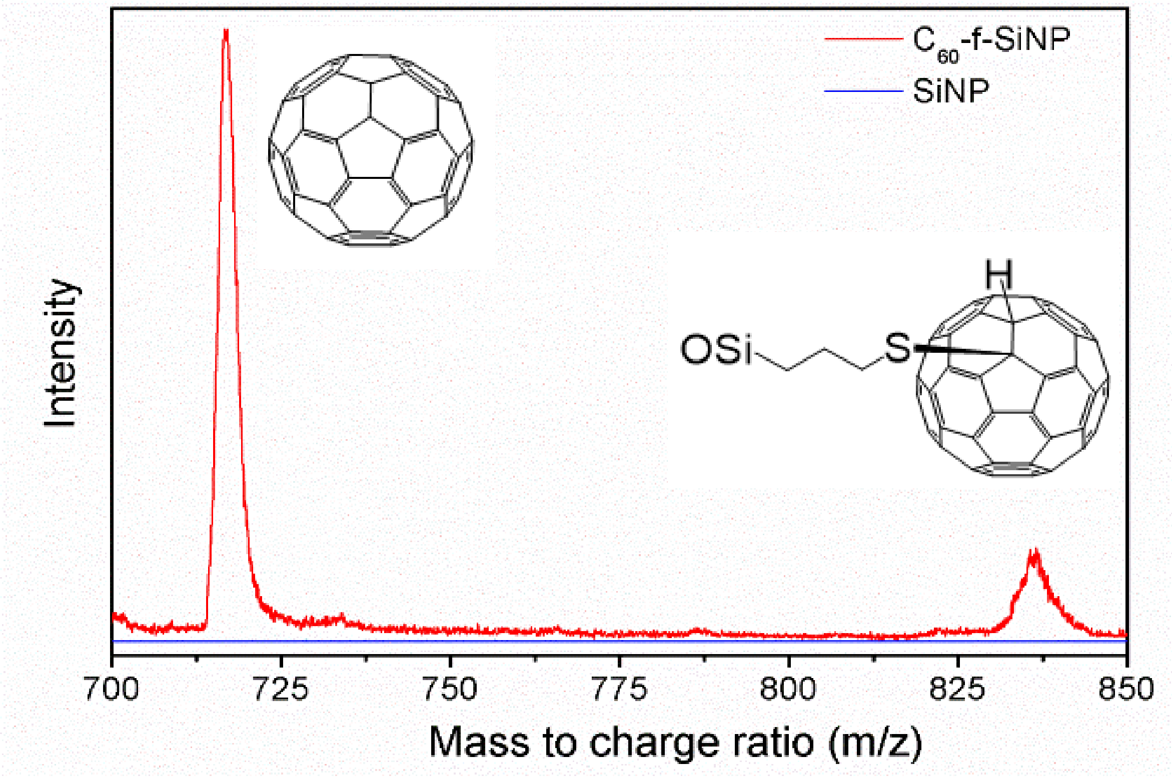

Figure 58: MALDI-ToF-MS spectra of charged ions (+ m/z) associated with the ablation of C_{60}-f-SiNP.

The larger m/z peak, which is less intense, is seen at 830+ m/z and is assigned to the Silica-Fullerene-C_{60} tether. No dimerization or polymerisation of Fullerene-C_{60} was seen within this process, where larger (+m/z) ratios, greater than the m/z regime shown above were also considered, as a potential by-product of free-radical reactions involving Fullerene-C_{60} can be the dimerization and polymerization of this moiety, to form repeating peanut like structures [103]

5.4.4 Thermogravimetric Analysis

The presence of Fullerene-C_{60} was confirmed also by thermogravimetric analysis. As shown in Figure’s 59 and 60, the mass loss and rate of mass change are tracked for both the C_{60}-f-SiNP (in the red trace) and SiNP (in the blue trace) with increasing temperatures.

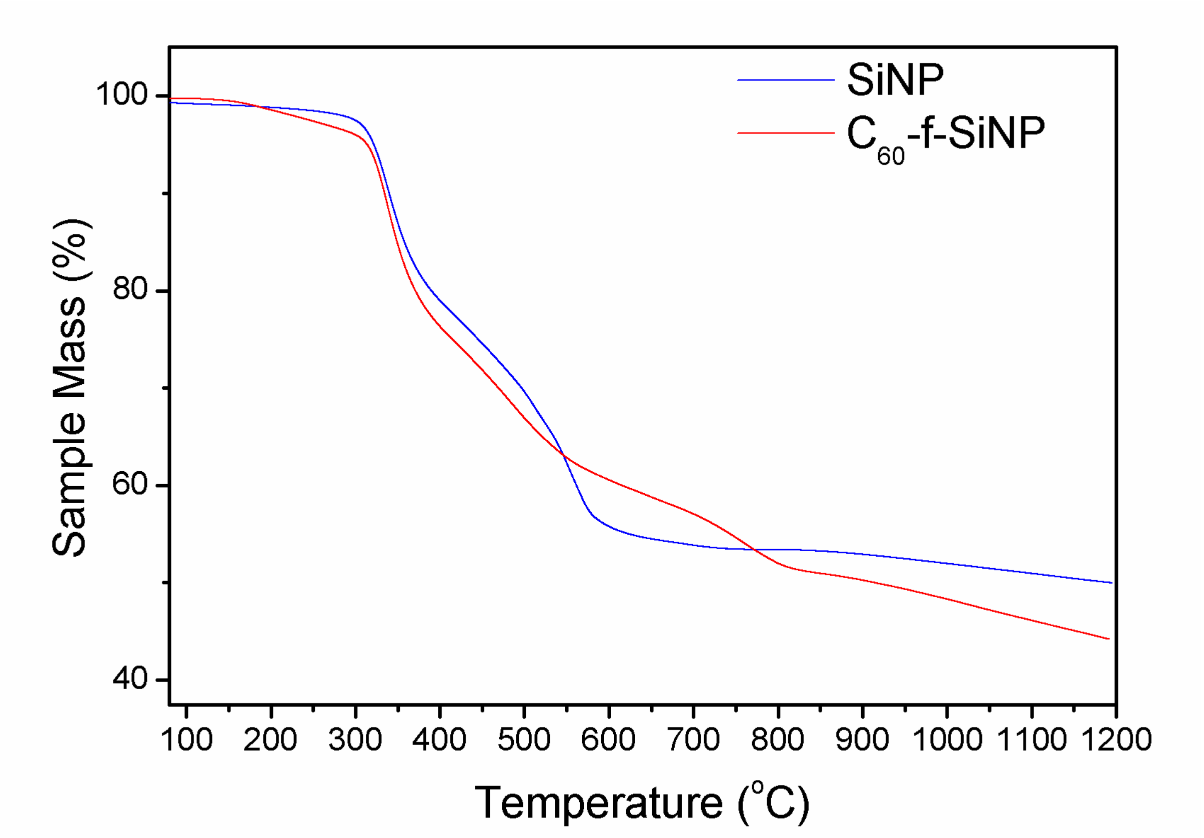

Figure 59: Plot of mass loss as a function of temperature (10 °C increase per minute) for SiNP and C_{60}*-f-SiNP*

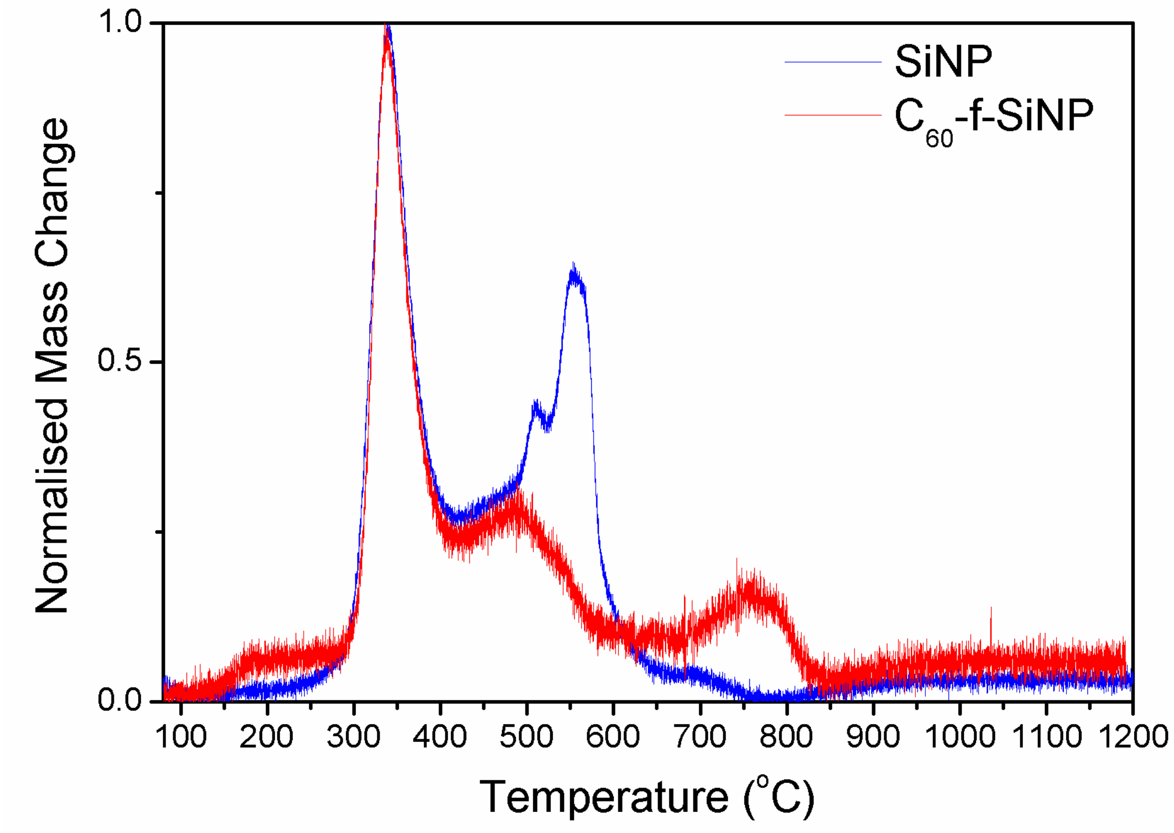

Figure 60: Plot of the first derivative (absolute) of the mass loss change, as a function of temperature

The C_{60}-f-SiNP shows a characteristic sublimation within the 600°C and 800°C regime, which accounts for a 4% mass loss. In both samples a silanol (Si-OH) to siloxane (Si-O-Si) condensation is seen to occur within the 400°C and 600°C region, subtly in Figure 59 and more clearly in Figure 60 it can be seen that the C_{60}-f-SiNP has a less defined mass loss profile than the SiNP sample for this temperature range, where the SiNP without Fullerene-C_{60}, is shown to undergo two overlapping events.

After treatment to 1200 °C both SiNP and C_{60}-f-SiNP were analysed by SEM, as shown in Figure 61 (a) the resultant structure of the SiNP sample is fused and monolithic in nature, whilst C_{60}-f-SiNP shown in Figure 61 (b) remained as spheres.

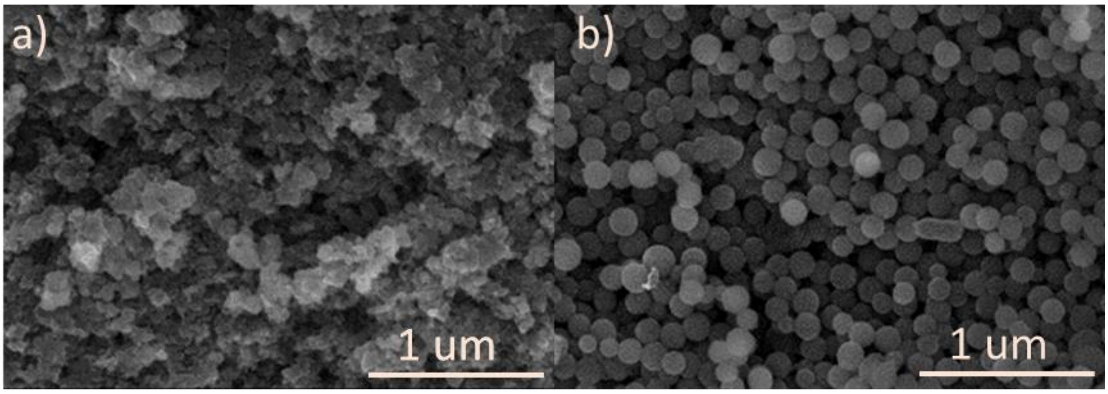

Figure 61: SEM of remains of SiNP (a) and C_{60}-f-SiNP (b) after treatment to 1200 ºC.

In the case of the C_{60}-f-SiNP, it is postulated that the presence of Fullerene-C_{60} could limit the condensation of Si-OH to Si-O-Si to the confines of the particle where the Fullerene C_{60} could be limiting the condensation space of the silanols.

5.4.5 Microscopy

5.4.5.1 Scanning Electron Microscopy

Cleaned C_{60}-f-SiNP were deposited onto silicon wafers, dehydrated, and observed by Scanning Electron Microscopy (SEM), and as evidenced by Figure 62, the evaporation of the solvent (dichloromethane) results in the aggregation of the particles into big clusters. It can be seen that these clusters have a periodic geometry indicative of spheres approximately 200 nm in size

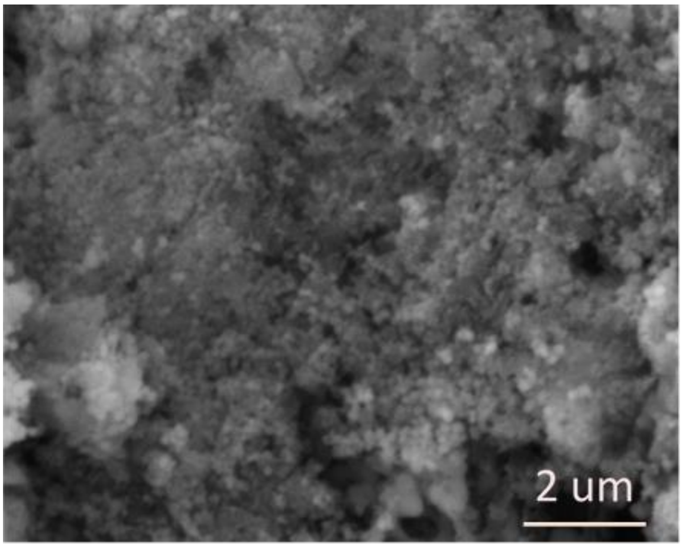

Figure 62: SEM of C_{60}-f-SiNP agglomerates on a silicon wafer

5.4.5.2 Transmission Electron Microscopy

High resolution TEM was performed on single SiNP and C_{60}-f-SiNP particles, coupled with elemental analysis by EDX. No significant difference was observed between the two particles using the elemental technique (EDX), as evidenced by Figure 63.

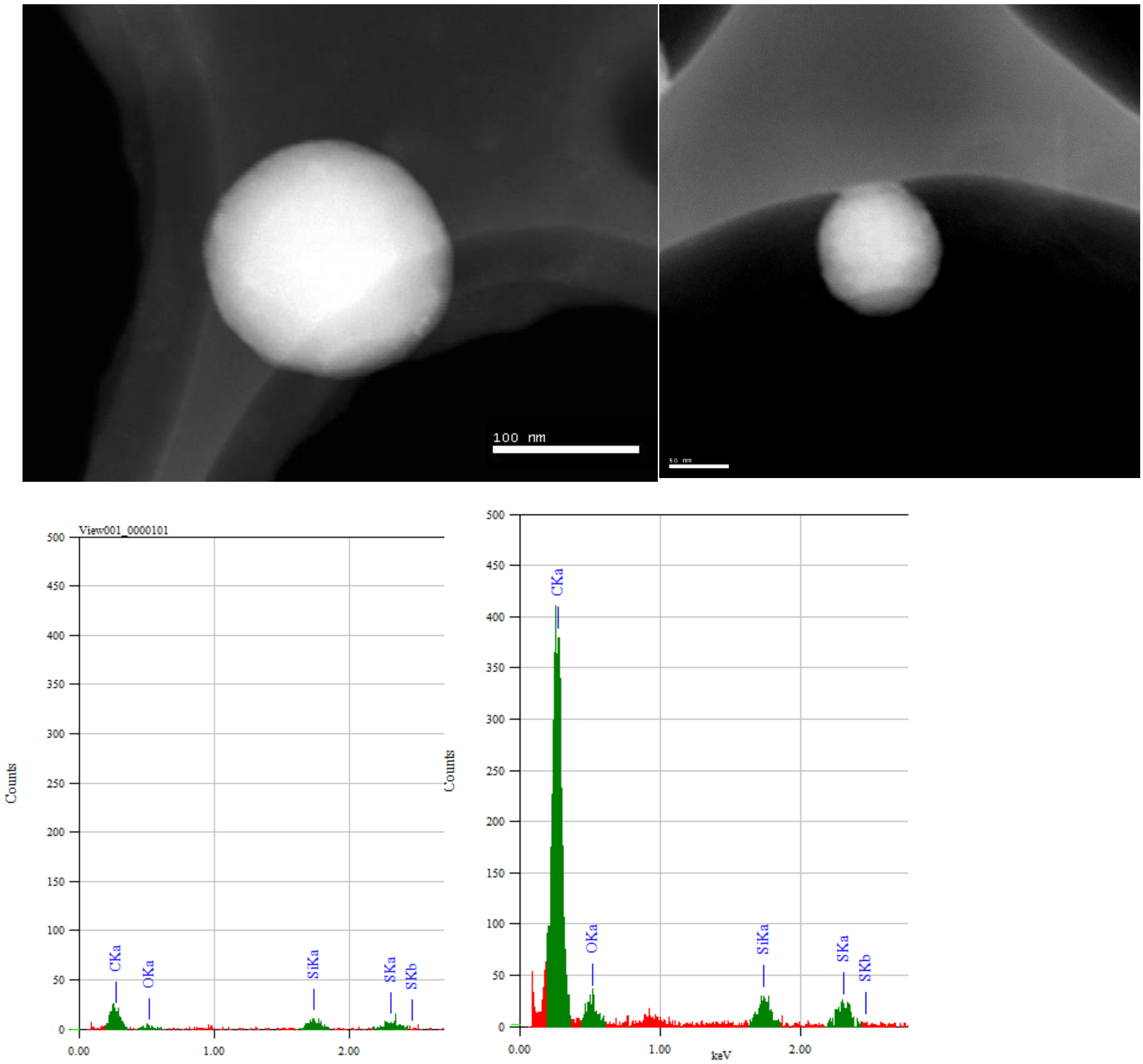

Figure 63: TEM (top) and EDX (bottom) of SiNP (left) and C60-f-SiNP (right)

Attempts to resolve this by TEM were unsuccessful, even by overlaying of focal projections as the focal plane is altered around the edge of the particle surface. Further to this, atomic force microscopy was utilized to consider the surface roughness.

5.4.5.3 Atomic Force Microscopy

Physical alteration of the particle surface was measured by Atomic Force Microscopy (AFM), where observable differences in nanostructure between the SiNP surface and C_{60}-f-SiNP are shown in Figure 64. The C_{60}-f-SiNP is rougher than the SiNP, where lighter areas of the height images (Figure 64 (right)) correspond to higher surface structures (further from the surface). It can be seen for the C_{60}-f-SiNP panels of Figure 64 that areas which are red in the phase diagram are periodically distributed on the surface, and correspond to the lowest points on the sample (closest points to the surface). It seems the deeper the tip gets into a trough of a surface feature, the interactions which are associated with the tip and the surface increase. It can be seen that the surface of the SiNP does show some roughness but the interactions between the tip and the surface are very different.

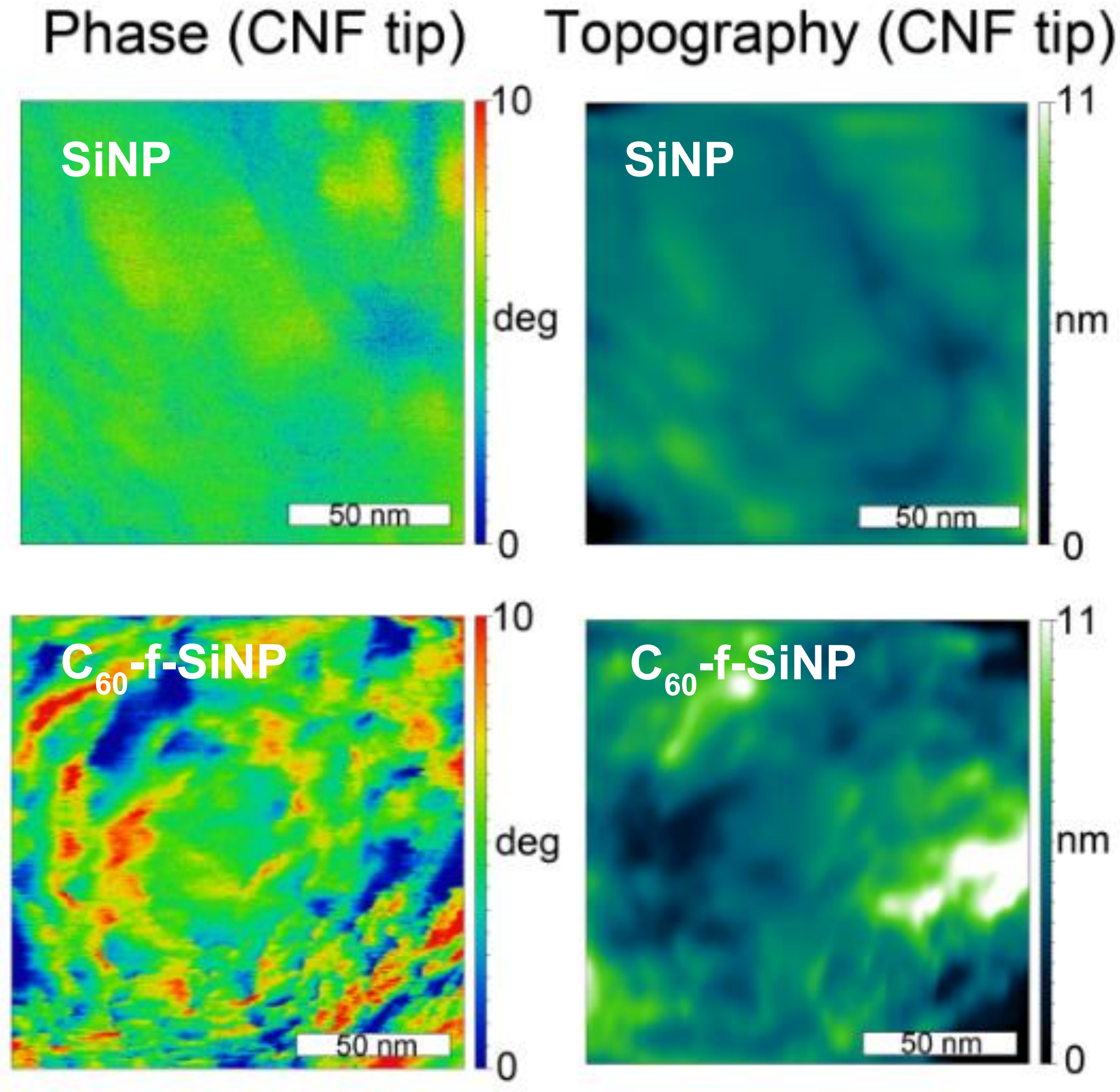

Figure 64: AFM images of the SiNP (top) and C60-f-SiNPs (bottom) with phase channel (left column) and topography channel (right column).

Whilst physical alteration of the particle surface can be seen qualitatively, quantitative interpretation of the phase data, and resolving a roughness profile for the C_{60}-f-SiNP was unsuccessful. It is believed that the hydrophobicity of the C_{60}-f-SiNP surface could be attributing to this, as well as the interactions between Fullerene-C_{60} and the CNT tip.

5.5 Formation of DDT-f-C_{60}

To confirm the chemistry occurring on the particle surface, Dodecanethiol (DDT) and Fullerene-C_{60} were reacted in the presence of thermally generated free radicals to form a DDT-f-C_{60} adduct as shown in Figure 65, and visually in Figure 66. Similarly to the particle system in described in Section 5.2, AIBN was used as a free radical generator. Also, similarly to the C_{60}-f-SiNP system, The DDT-f-C_{60} product was examined by common analytical techniques including MALDI, NMR, ATR-FTIR as well as UV-Vis, in order to gain more insight into the mechanism.

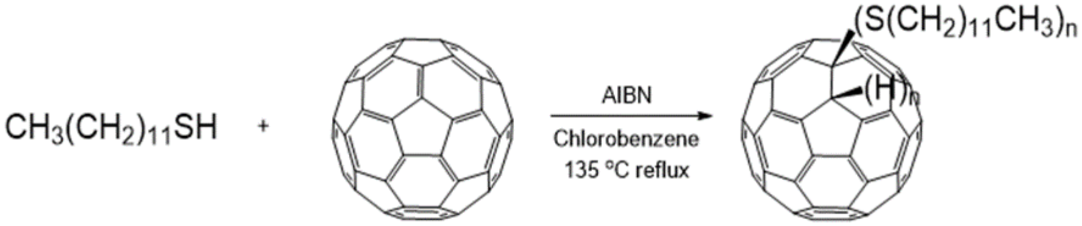

Figure 65: Attachment of dodecanethiol to the Fullerene-C_{60} cage to form DDT-f-C_{60}

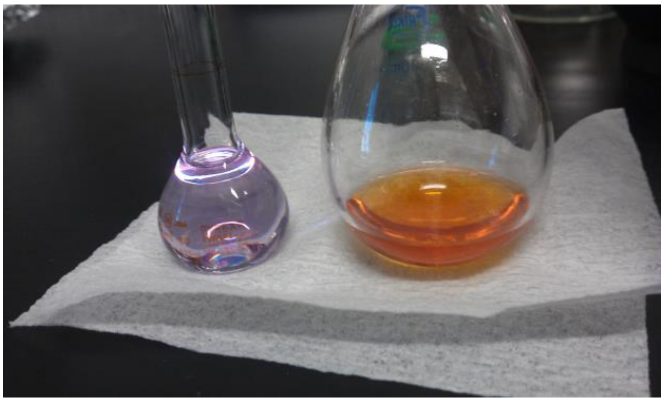

Figure 66: Image of Fullerene-C_{60} (left) and Dodecanethiol-f-C_{60} (right)

5.5.1 ^1H and ^{13}C NMR

5.5.1.2 ^1H NMR

NMR studies of the product reveal that the attachment of dodecanethiol to Fullerene-C_{60} is not a simple process. It can be seen in Figure 67 in the red trace that an appearance of new peaks in the higher chemical shift regime which correspond to the hydrogens on the carbons alpha and beta to the sulfur of DDT-f-C_{60} at 2.70 and 1.68 ppm. However, there are still peaks present at 2.53 and 1.67 ppm, which overlay with peaks that are assigned to the DDT material as hydrogens alpha and beta to the sulfur also.

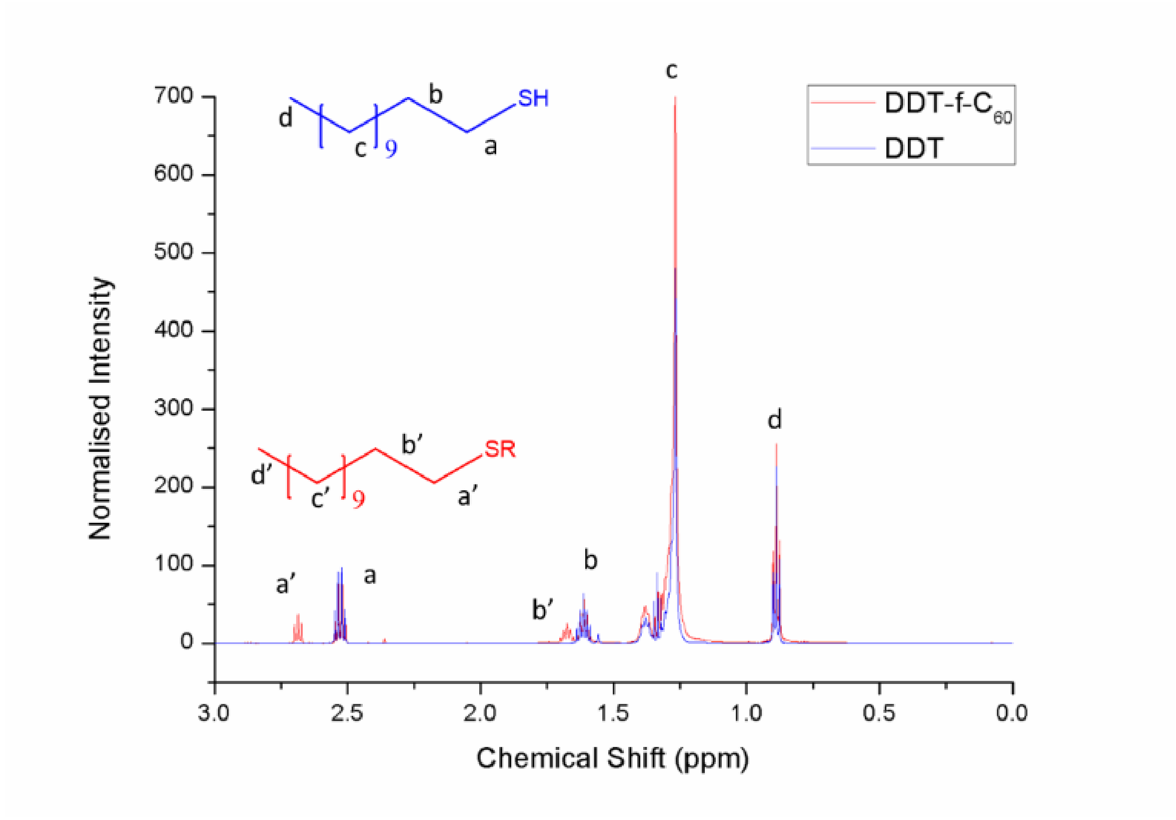

Figure 67: ^{1}H NMR of dodecanethiol (blue) and dodecanethiol-f-C_{60} (red)

After functionalisation and purification of the product, similar environments to DDT remain within the DDT-f-C_{60} adduct, where the red and blue traces above are superimposed. The hydrogens associated with the alpha (labelled a and a') and beta carbons (labelled b and b') are shown in greater detail in Figure 68. Specifically comparing a to a' it can be seen that the chemical environment changes from a quadruplet from a triplet, which suggests that the hydrogen attached to the sulfur heteroatom at the end of the alkyl chain is being removed during the functionalisation process, where the thiol attaches to the fullerene cage, which is sensible. However, the integration for the associated peak areas are not stoichiometric, suggesting that this is not a simple attachment mechanism, and that there are potentially multiple different processes occurring.

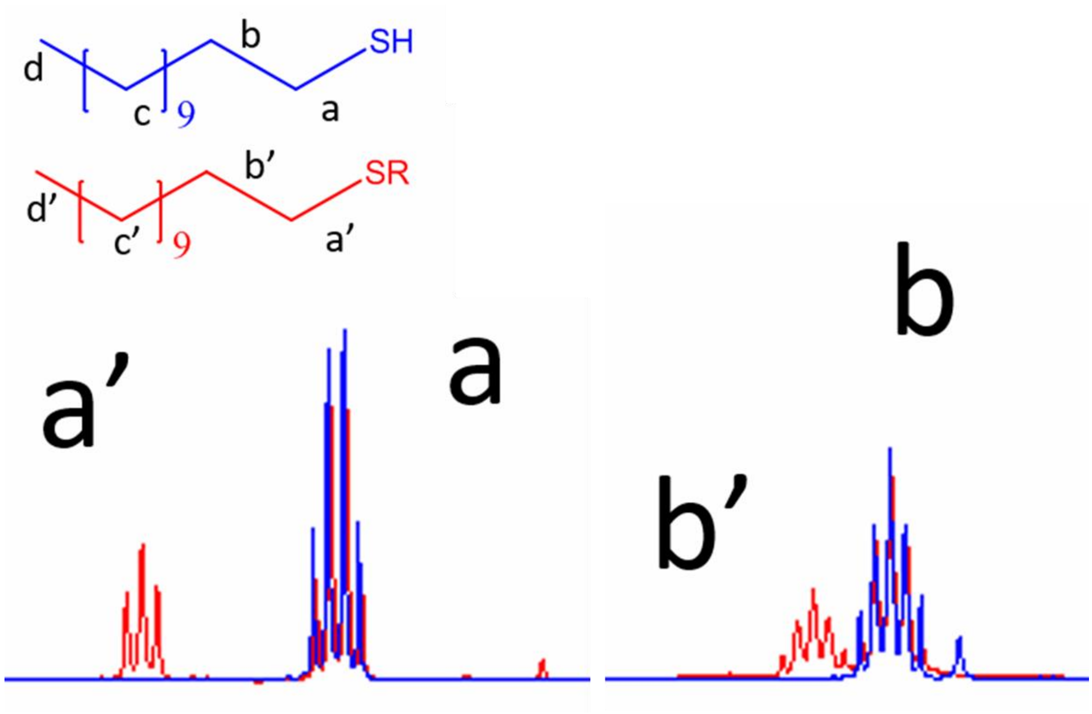

Figure 68: Zoomed in View of NMR Peaks

5.5.1.3 ^{13}C NMR

The ^{13}C NMR nuclei in Figure 69 shows less unique carbon environments exist for the DDT-f-C60 than the DDT molecule itself. Peaks associated with aliphatic hydrocarbon C-C environments which occur in the 0-50 ppm region are shown below. However, it would be expected for sp^2 hybridised carbons with double bond characteristics for peaks to be present within the 100-150 ppm region, which are not seen for the functionalised sample.

This suggests that the interactions between the Fullerene-C$_{60}$ and the DDT are not simple, and could indicate that the Fullerene-C$_{60}$ loses its double bond character during the solution based reaction process, or that the solubility of Fullerene-C$_{60}$ within the sample was too low for analysis, which is likely, given between 15 mg – 20 mg would be soluble within the confines of an NMR tube.

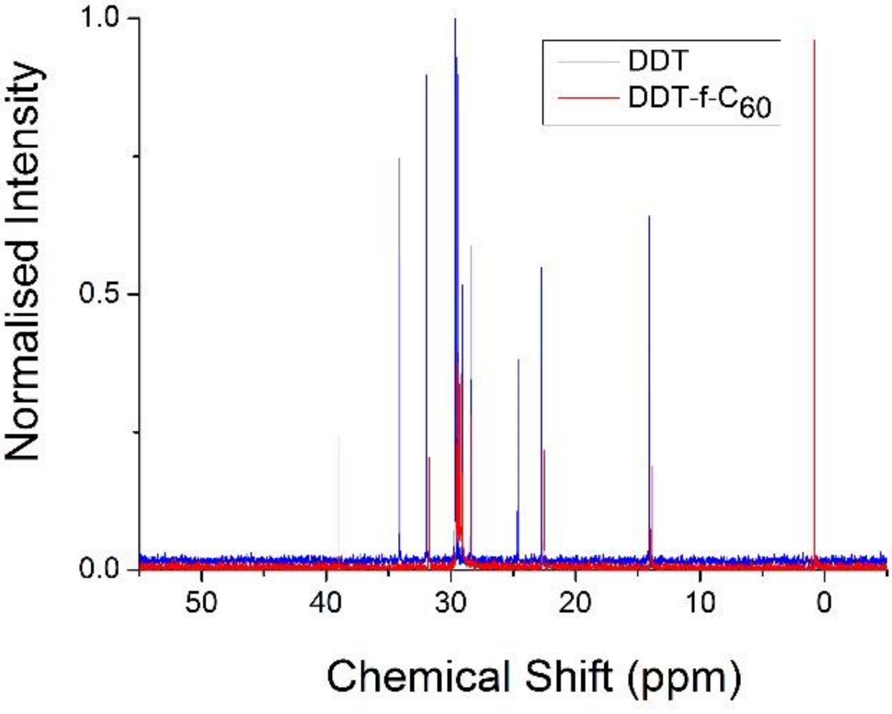

Figure 69: ^{13}C NMR of dodecanethiol (blue) and dodecanethiol-f-C_{60} (red)

5.5.2 MALDI-ToF-MS

The presence of Fullerene-C_{60} within the DDT-f-C_{60} sample was confirmed by MALDI-ToF-MS. As shown below in Figure 70, the characteristic 720 m/z peak, indicative of the molecular ion of Fullerene-C_{60}, can be seen. Larger fragments are seen sequentially in the higher order m/z regime in 14-16 mass unit increments, above the 720 m/z peak, believed to be either due to modification of the Fullerene-C_{60} cage. It is also noticeable that the alkyl thiol is easily cleaved from the surface, with a strong molecular ion for DDT seen in the lower m/z regime.

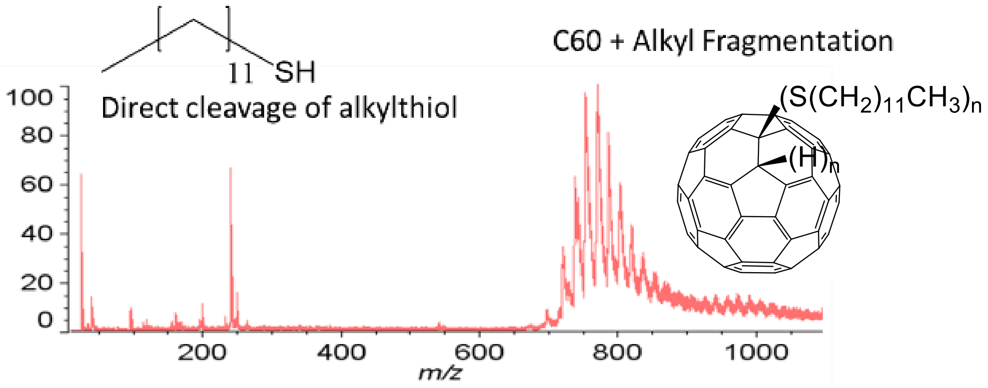

Figure 70:MALDI-ToF-MS of DDT-f-C_{60}

5.5.3 ATR-FTIR

To verify the assignment of fragments in the MALDI-ToF-MS above, the functional groups present within the DDT-f-C_{60} product was considered by ATR-FTIR, where a spectral comparison of the product in the red trace is compared to the starting reagents DDT and Fullerene-C_{60}, shown in Figure 71 below as the blue and teal traces respectively. The specific assignment of peaks of interest are reported in Table 7, where specifically it can be seen that new dipole active modes exist for the DDT-f-C_{60} product, when the traces are compared. The fingerprint region specifically has multiple new infra-red environments associated with the polyaromatic carbon-carbon symmetry distortion, as well as multiple C-S stretching modes. Presence of these fingerprint peaks (A & B), along with the peak labelled E at 1730 - 1660 cm^{-1} and the presence of aromatic C-H stretches which are very weak at 3070 – 3020 cm^{-1} suggests that the Fullerene-C_{60} component of DDT-f-C_{60} still contains double bonds.

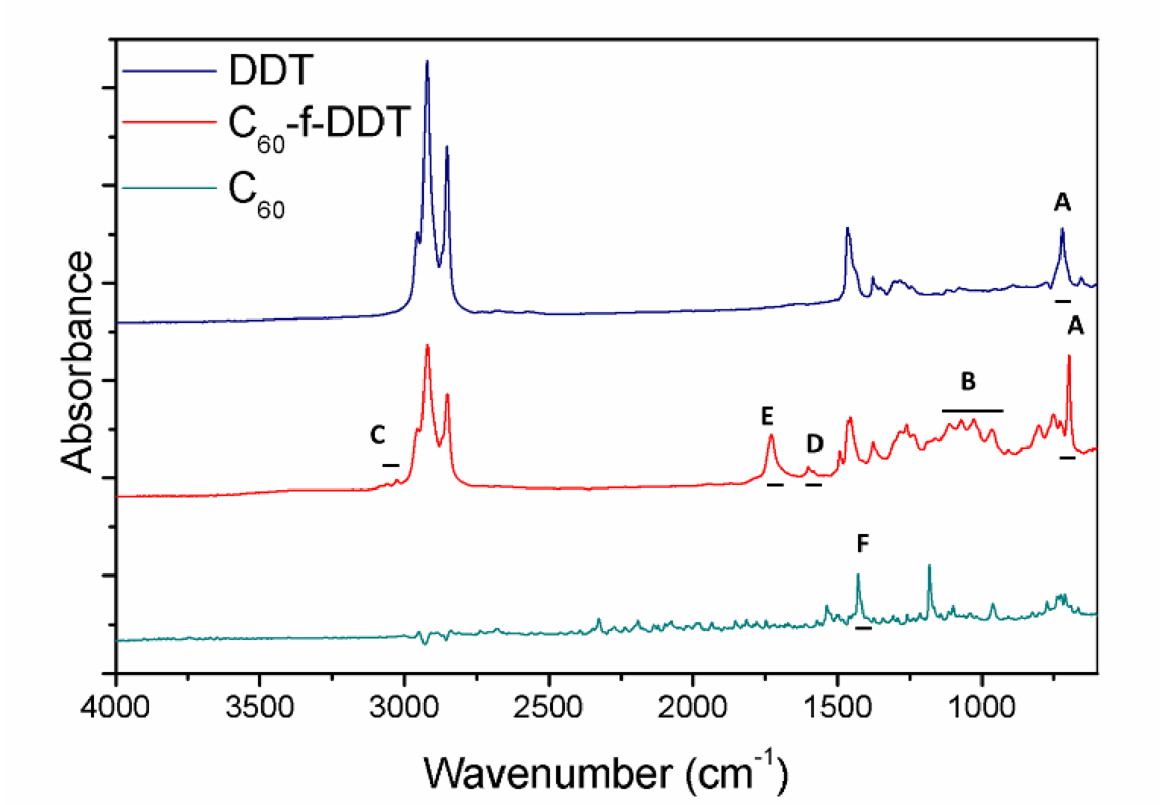

Figure 71:ATR-FTIR spectra of DDT (Blue), C_{60}-f-DDT (Red) and C_{60} (Teal).

Table 7: Assignment of ATR-FTIR peaks in Figure 71

Label	Wavenumber (cm^{-1})	Assignment
A	720 - 698	C-S Stretch
B	1070 – 900	Polyaromatic Substituted C-H Rocking
C	3070 – 3020	Aromatic Hydrocarbon Stretching
D	1580	C-C F1u Symmetrical Mode
E	1730 – 1660	Polyaromatic Substituted C=C Stretch
F	1460	C-C F1u Pentagonal Pinching Mode

Aliphatic and Aromatic C-H stretching environments seen in the DDT-f-C_{60} in the higher wavenumber regime confirms the presence of different carbon environments, that should have been visible in the carbon NMR.5.5.4 UV-Vis

The structure-less absorption features of the DDT-f-C_{60} in the UV-Vis region is shown in Figure 72. This suggests that the DDT-f-C_{60} is not stereospecific, and potentially a multi-adduct species

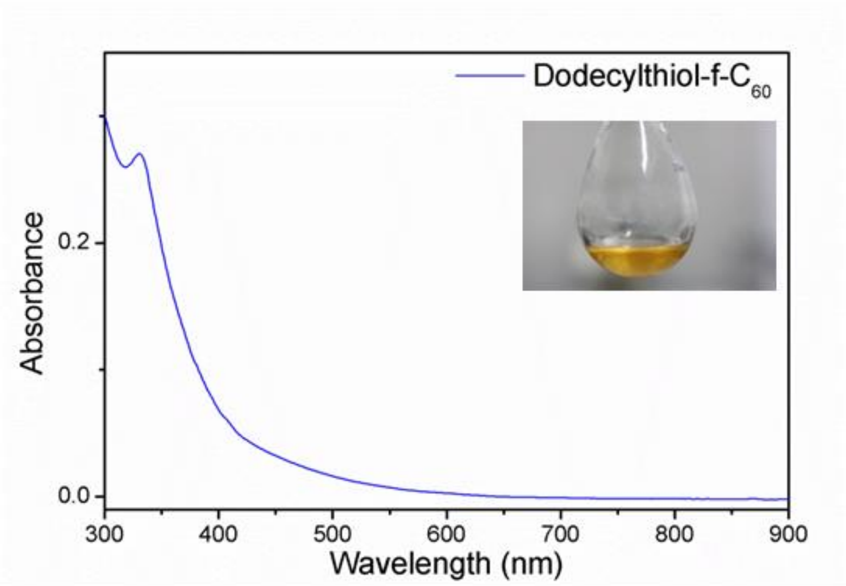

Figure 72:UV-Visible absorption spectrum of DDT-f-C_{60} and its photograph under visible light (hexane solvent)

5.6 Conclusions

This chapter describes the first covalent interaction between an alkyl thiol and Fullerene-C_{60}, where successful attachment of Fullerene-C_{60} to the surface of SiNP is mediated by thermal free radical generation, to create a rough raspberry like structure, C_{60}-f-SiNP. The loss of S-H (2553.33 cm^{-1}) and formation of C=C-H character (1659.46 cm-1) after formation of C_{60}-f-SiNP from SiNP, where the presence of the Fullerene-C_{60} moeity is confirmed by MALDI-Tof-MS with characteristic m/z of +720. The absorbance of the C_{60}-f-SiNP in the UV-Visible region show similarities to Fullerene-C_{60}, and observable differences in nanostructure are seen by AFM.

Dodecanethiol and Fullerene-C_{60} were reacted to form DDT-f-C_{60}, to further understand the chemistry occurring on the particle surface when SiNP and Fullerene-C_{60} react to form C_{60}-f-SiNP. The analysis of DDT-f-C_{60} by ATR-FTIR and MALDI-ToF-MS confirmed the presence of both Fullerene-C_{60} and DDT within the isolated product. The UV-Vis absorption profile as well as the issues surrounding peak identification for ^{1}H and ^{13}C NMR pectra of the DDT-f-C_{60} suggest that the solution reaction lacks specificity.

Chapter 6| Heating and ignition of C_{60}-f-SiNP

6.1 Overview

This chapter focuses on recreating an observation of ignition / combustion of C_{60}-f-SiNP during a Raman spectroscopy experiment. Thermal tracking of the energetic properties of laser induced ignition from an Nd:Y_3Al_5 (Nd:YAG) 1064 nm laser source, and then the subsequent exposure of this material to a conventional Xe tube camera flash, results in the formation of hollow particles and reconstruction into amorphous carbon sheets, which are observed using TEM.

6.2 Introduction

Following extensive analysis of C_{60}-f-SiNP in Chapter 5, attempts were made to characterize the material using Raman spectroscopy, to gain insight into the chemical characteristics, bonding structures and carbon configurations present within the sample. This was unsuccessful, as the C_{60}-f-SiNP was observed to rapidly ablate upon exposure to the Raman laser, even when the intensity of the laser was heavily attenuated. As a result, no information was obtained from the detector regarding the different chemical environments present within the C_{60}-f-SiNP.

Fullerene-C_{60} derivatives, amongst other sp^2 functionalized carbon allotropes such as nanotubes and graphene have been known to ignite and deflagrate upon absorption of energy in the IR or NIR range. This phenomena is described by Krishna et al (2010) where the formation of SWCNT, MWCNT and Carbon Onions occurs from a variety of functionalized Fullerene-C_{60} derivatives, in an oxygen free environment. These molecules included poly-hydroxyl fullerene, fullerene bromide and fullerene hydride, as shown in Figure 73.

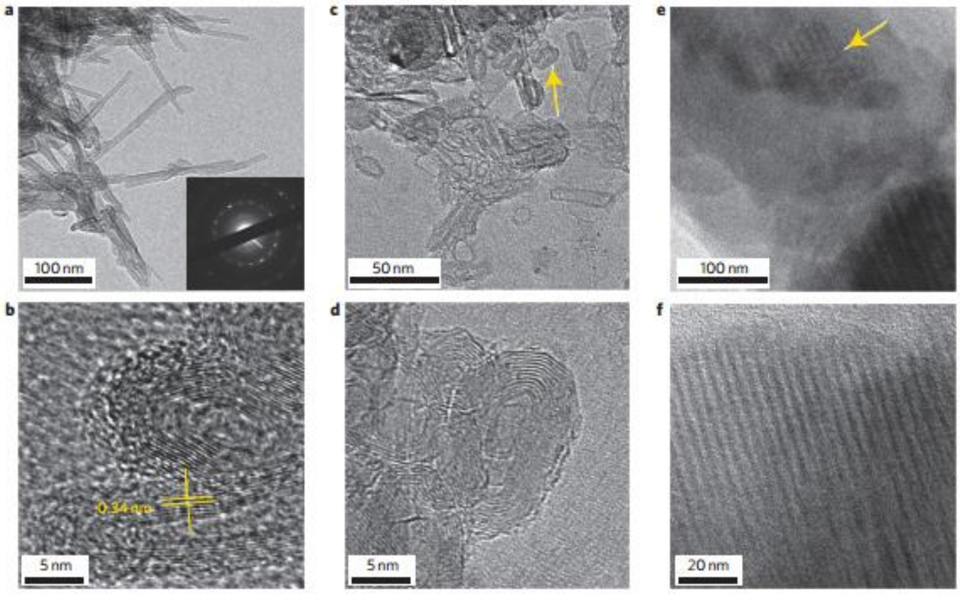

Figure 73: Structures formed from irradiation of polyhydroxyfullerene with a 785 nm laser under an argon atmosphere.[94]

This Chapter is focused specifically on the controlled optical heating of C_{60}-f-SiNP, where the temperature profiles of each event is measured, and electron micrographs of the images are collected.

6.3 Nd:YAG laser treatment

6.3.1 Single Pulse treatment

To measure the temperature of the material after being subjected to the Nd:YAG laser, a pyrometer was fitted and centered over where the laser path, the pyrometer and ablation apparatus are clearly identified below in Figure 74, where the path of the laser to the sample is illustrated by the red line. For the purposes of these experiments the Fullerene-C_{60} sample is contained in a small vial of 2.3 cm^3 internal volume. This allowed for the sample to retain within the vial, which is open, but bottlenecks, as shown in Figure 75 below.

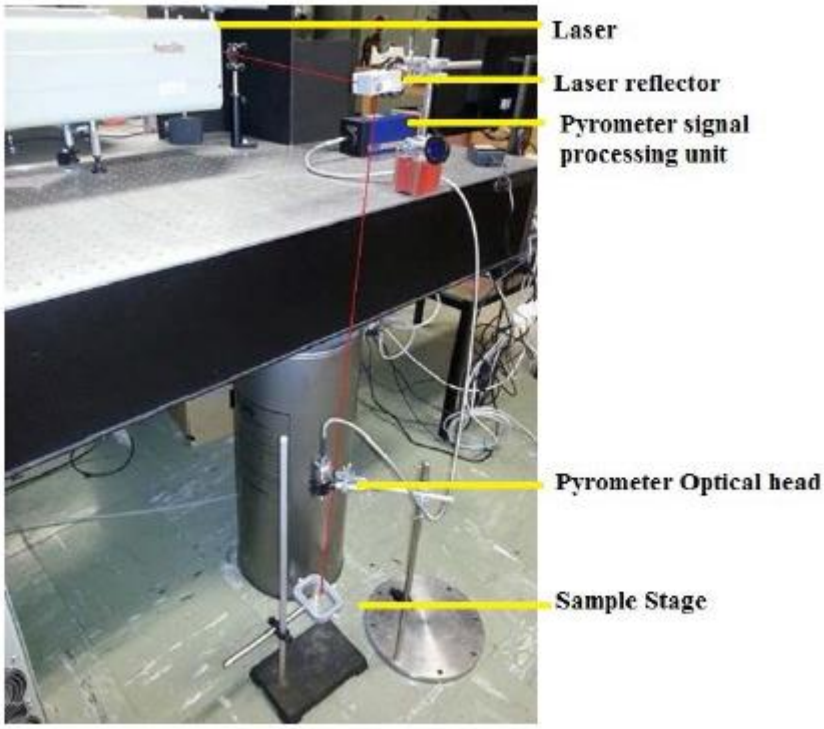

Figure 74: Nd-YAG laser setup showing the beam path to the sample stage, with pyrometer attachment [104]

Figure 75: Image of the vial with C_{60}-f-SiNP particles pushed into the middle.

Upon ablation of C_{60}-f-SiNP by the Nd:YAG laser, a visual flash and popping sound were produced, where the explosion of the material can be seen to occur frame by frame in Figure 76. It can be seen in the sequential images that the particles blast upward, where in the last frame, some of the particle can be seen being ejected out of the vial and onto the sample stage.

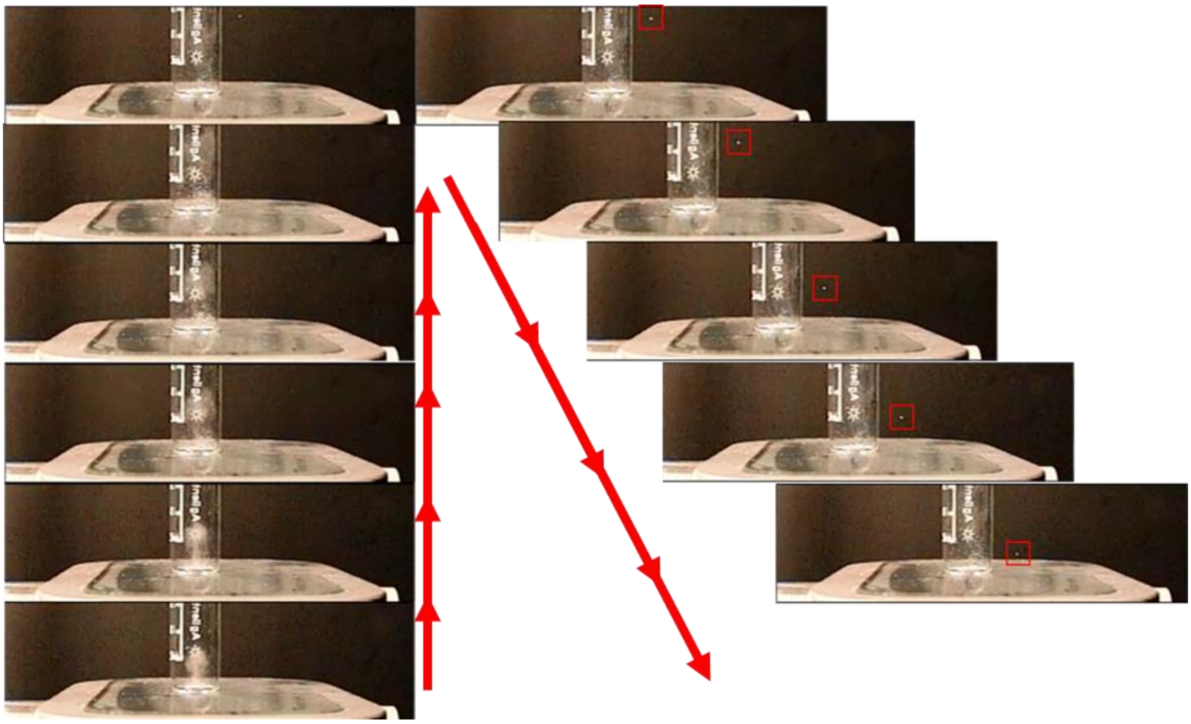

Figure 76: Sequential images of C_{60}-f-SiNP response to Nd:YAG laser treatment

This process was repeated for Fullerene-C_{60} and DDT-f-C_{60} also, which did not produce airborne particulates like the C_{60}-f-SiNP, but did ignite with an audible pop. Temperature of these events was monitored over time using the pyrometer setup as shown below in Figure 77. Similarities can be seen between the thermal profiles of C_{60}-f-SiNP and Fullerene-C_{60}, which absorb for a much longer length of time than the DDT-f-C_{60}.

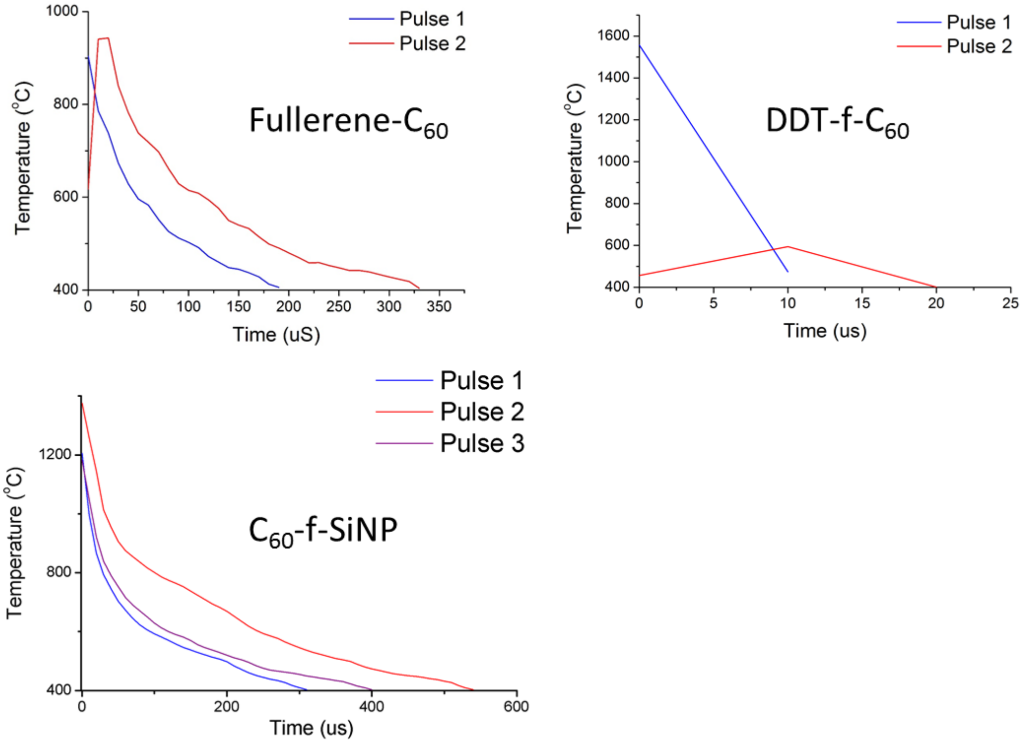

Figure 77: Tracking thermal ablation of Fullerene-C_{60}, DDT-f-C_{60} and C_{60}-f-SiNP with Nd:YAG laser

It can be seen in descending order that C_{60}-f-SiNP had the longest thermal lifetime of (300 – 530 us), followed by Fullerene-C_{60} (180 – 325 us) and DDT-f-C_{60} (10 – 20 us). It can be seen above that the two solid samples (Fullerene-C_{60} and C_{60}-f-SiNP) both have a lower maximum temperature (950 ^{o}C and 1200 ^{o}C) but longer thermal lifespan than the DDT-f-C_{60}, which has a maximum temperature of 1500 ^{o}C, but a very short lifetime in comparison. This could be due to DDT-f-C_{60} being a liquid in comparison to Fullerene-C_{60} and C_{60}-f-SiNP, which are solids.

In the case of the C_{60}-f-SiNP, this Nd:YAG ablation process results in the formation of hollow particles as shown in the Transmission Electron Micrograph in Figure 78 below. The hollow structures resultant from the Nd:YAG ablation, are mainly comprised of silicon and carbon in comparison to the particles pre-ablation, which are shown on the left hand side of Figure 78, which shows a stronger sulphur signal for the SiNP.

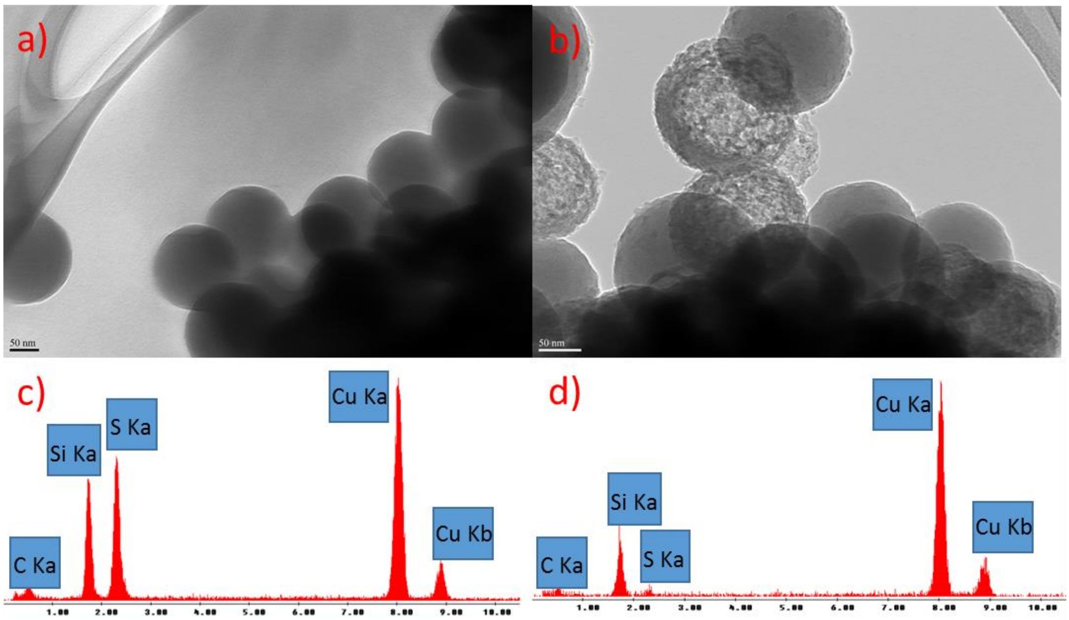

Figure 78: TEM and EDX (a,c) of C_{60}-f-SiNP pre ablation and TEM (b,d) of hollow sphere containing sample after ablation of C_{60}-f-SiNP. (Copper peaks are associated with the TEM grid)

6.3.2 Multiple Pulse treatment

Upon numerous Nd:YAG pulses, a pod like structure is seen in the TEM as shown below in Figure 79, where it is illustrated that the particles no longer sit side by side and are enveloped in a carbonaceous shell.

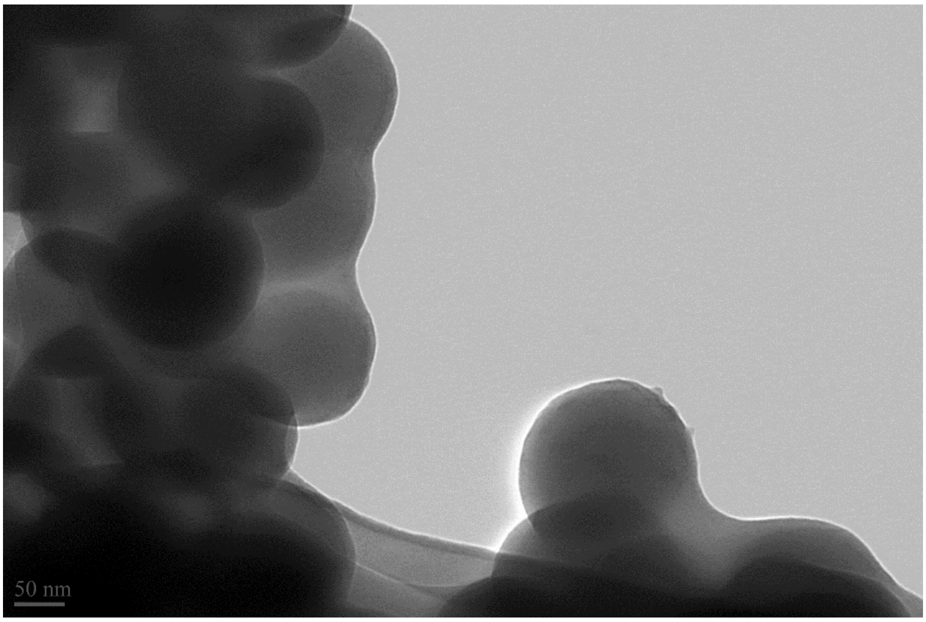

Figure 79: TEM of 'pod-like' particle structures

Representative images of this sample are shown in Figure 80, which suggest that the particle surface is exfoliating upon increased ablation, which could be the polymerisation of the Fullerene-C_{60} layer during the thermal excitation process, which is best visualised in Figure 80(d). Some particles show areas of low exfoliation, where nipple-like structures appear on the particle surface, as is shown in Figure 80(c). Similar looking electron micrographs exist in literature, where carbon rich polymeric materials have been grown off the surface of silica nanoparticles to create a core shell structure.[105]

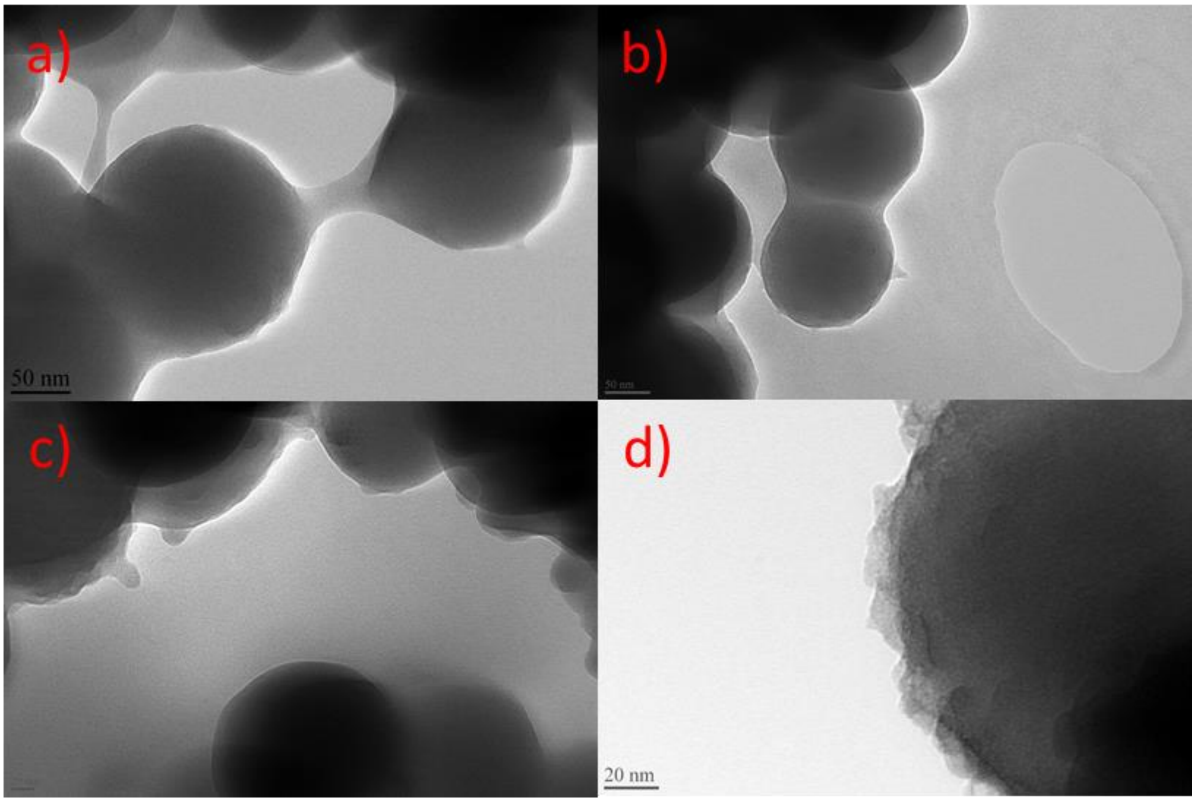

Figure 80: TEM images of multiple pulsed C_{60}-f-SiNP ablated constructs

6.3.3 Discussion

A proposed mechanism has been established for the laser-induced transformation of functionalised fullerenes which is shown in Figure 81 below. It is believed that the rapid increase in temperature from the absorption event causes thermal expansion of the air surrounding the nanomaterial, triggering an acoustic wave, which results in the collision of fullerene cages, which can induce coalescence and/or disintegration of the macromolecular structure.

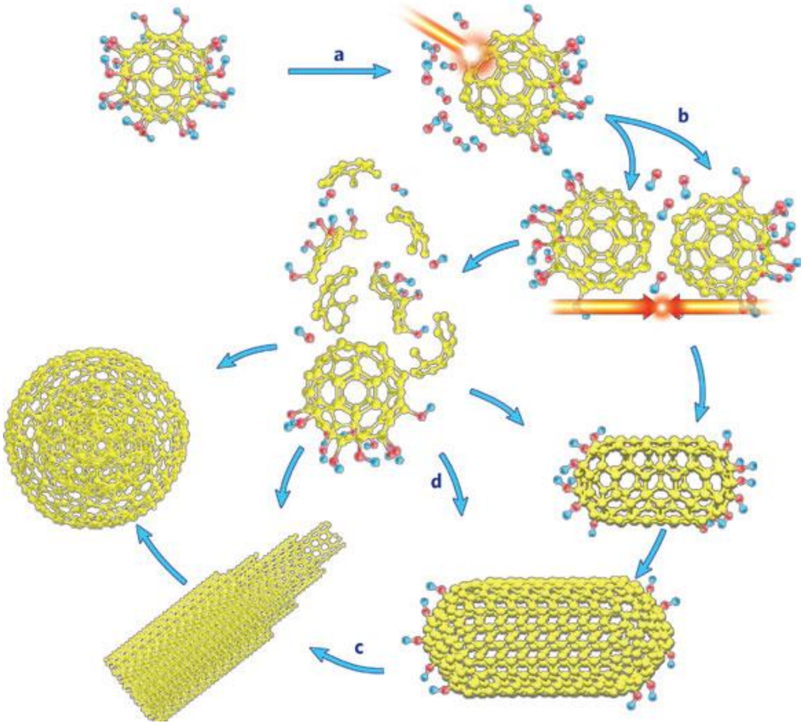

Figure 81: Reconfiguration of Functionalised-$C_{(60)}$[94]

It has been reported that the optical heating and ignition temperatures required for thermal events to occur in Fullerene-C_{60} depend on the functionality of the moiety, where poly-amino, hydroxyl and carboxylised fullerene derivatives have been investigated previously. In such cases, it was argued that the distortion of the molecular cage was the most likely factor to be contributing to this effect, where other influences could be by absorption from different higher ground or excited absorption states. In the case of the C_{60}-f-SiNP discussed in Section 5.3.2, the ground state absorption seen in the solid state UV-Vis shows only slight λ-max shifts relative to the Pristine C_{60}.

6.4 Xe Camera flash, following Nd:YAG laser treatment

Xe camera flashes are known to incite molecular reconfigurations in carbon nanotube structures, in the presence of trace metals. For the purposes of these experiments, the pyrometer only detected unique thermal profiles for the C_{60}-f-SiNP samples that had been subjected to a Nd:YAG laser, containing the hollow spheres.

It is seen below in Figure 82 that when thermal events of each sample are tracked over time, multiple energetic events occur as a result of the Xe flash only in the samples that have been pre-ablated with Nd:YAG laser as discussed in Section 6.2.1. Clearly defined cascading endothermic and exothermic events are recorded by the pyrometer, where the width of each energetic event corresponds to 140 – 170 us. These energetic events do not occur in the control samples (SiNP, Fullerene-C_{60}, Blank) where the temperature profile is seen to plateau over time, where the temperature of the material quickly increases and slowly decreases.

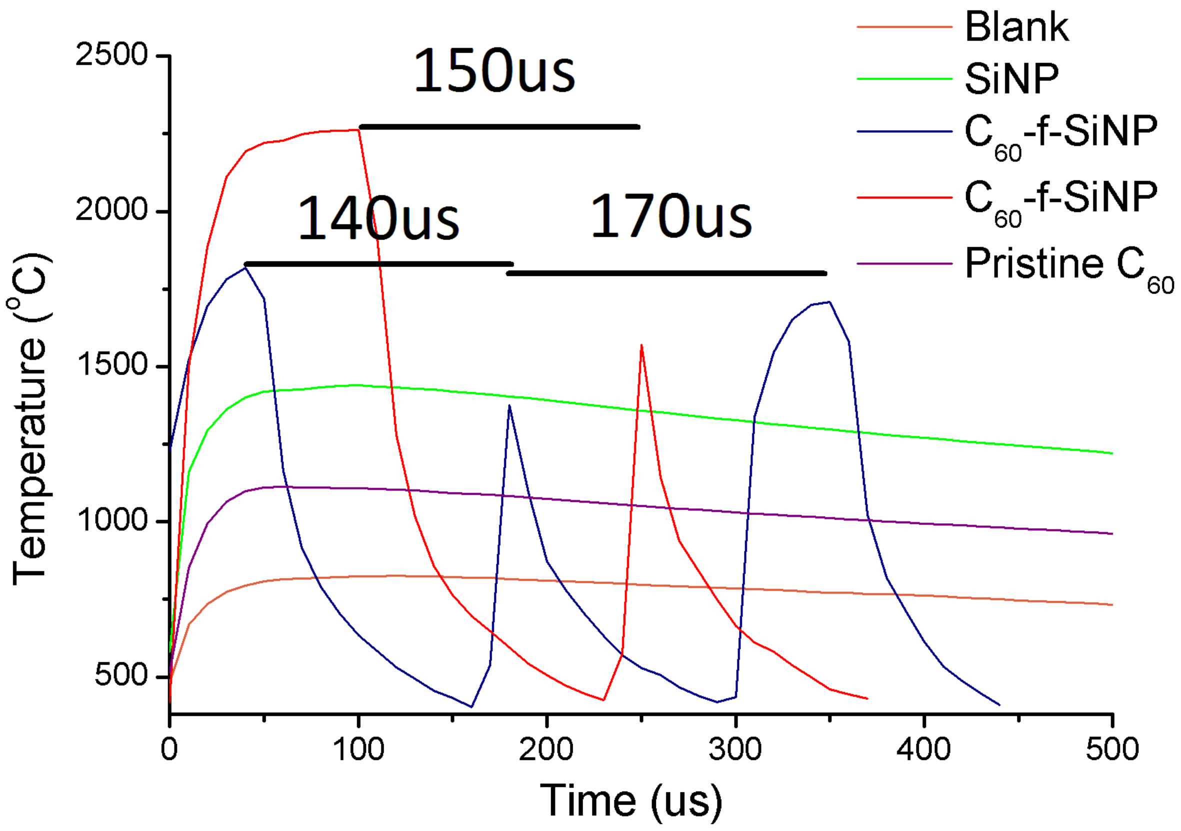

Figure 82: Temperature profiles of camera flash treated samples from pyrometer. (Blank refers to temperature measurement of the camera flash + sample stage)

This energy taken up by the silica core is believed to be transferred externally to the carbonaceous sheet surrounding the particle to form compact amorphous carbon structures, as seen in the TEM images below in Figure 83.

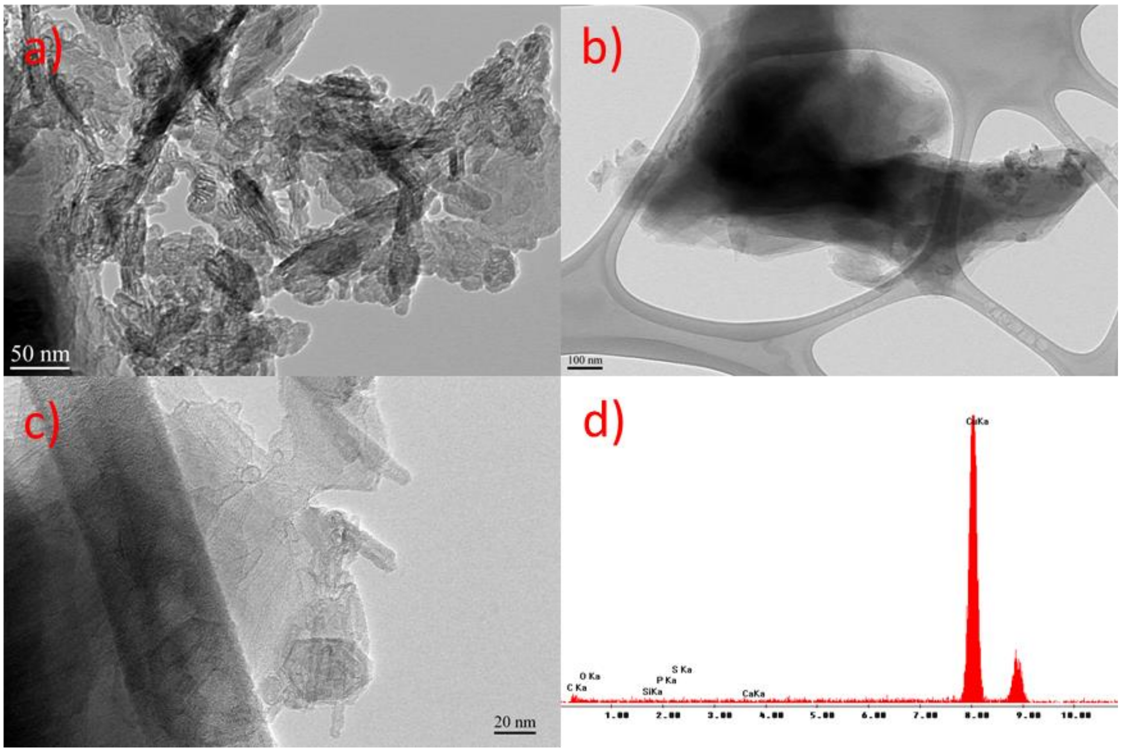

Figure 83: TEM of Xe treated carbonaceous flakes (a-c) and unremarkable EDX (d), showing emission from the copper grid only

Whilst believed to be carbon, the X-Ray diffraction pattern in Figure 84 suggests that there is a lack of repeating structure within these sheets, suggesting they are amorphous, and not crystalline.

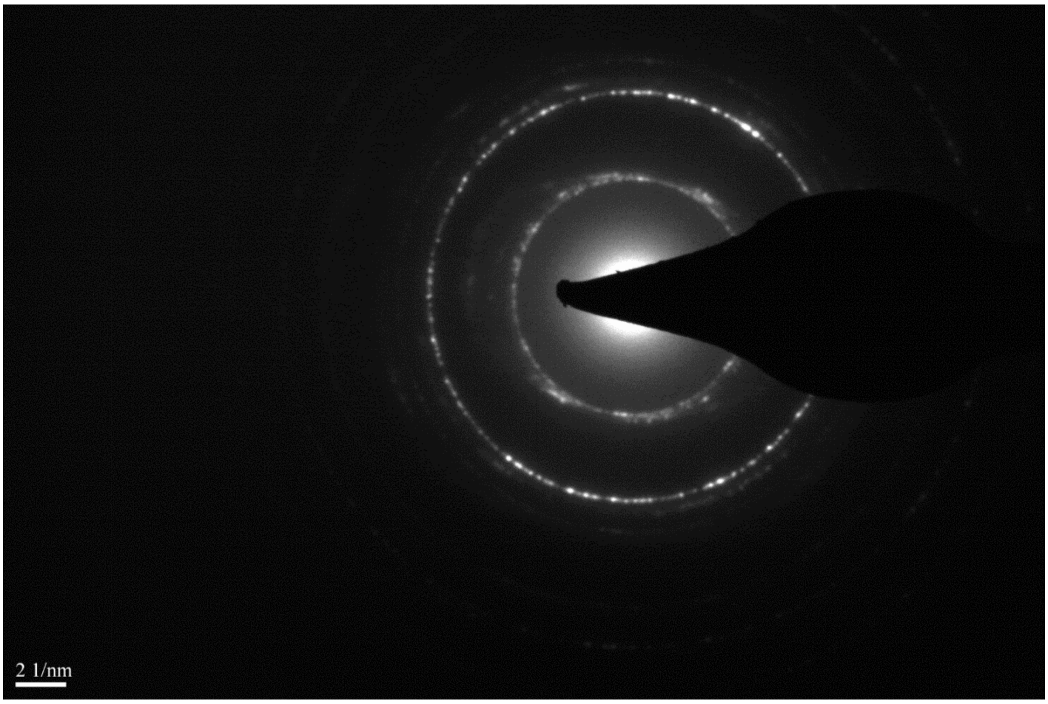

Figure 84: X-Ray diffraction pattern of carbonaceous flakes, which appear to be amorphous

6.5 Conclusions

This chapter highlights that the C_{60}-f-SiNP material created in Chapter 5 is energetic, and can form interesting and diverse structures, including hollow spheres, and amorphous carbon when subjected to a laser and camera flash.

Further to this the hollow spheres created by the laser, when subjected to the camera flash have a unique and eventful temperature profile, in which multiple sequential events are tracked by the pyrometer, which results in new structures being created in the TEM, believed to be due to the exfoliation of surface carbon from the Fullerene-C_{60} layer of C_{60}-f-SiNP.

Chapter 7| Conclusions and Future Work

7.1 Conclusions

Prior to this work, an understanding of the attachment density on the surface of silica nanoparticles was limited to hydroxyl terminated SiO_2 particles only, being characterized quite extensively due to their multitude of applications in a variety of disciplines. An increased understanding of the role functional organic arms have on the growth and attachment density of silica based nanoparticle technologies, as well as the attachment density, and chemistry occurring on the particle surface is paramount to optimizing the surface properties of the particle. Chapter 2 describes the experimental protocol and technical details to do with the formation, chemical modification, analysis and heating of organo-functionalised silica nanoparticles, under controlled conditions.

A description of the controlled growth and analysis of silica nanoparticles with functionality such as phenyl, vinyl, cyano and thiol is demonstrated in Chapter 3. Concentration dependent growth was demonstrated for the phenyl based system. Further measurements on the thiol-terminated silica nanoparticle revealed a surface area of 110,000 nm^2 per 170 nm particle, and through ^{29}Si NMR and computational particle construction, approximately 4.7 sulfur heteroatoms present per nm^2 of particle, which did not change upon theoretical hydration models.

Following this, a simple alkene, 11-bromo-1-undecene, is attached to the surface of silica nanoparticles where the attachment density is determined to be approximately 4.9 attachments per nm^2 of particle. A concentration and time dependence upon attachment density was explored, where it was identified that a 730 molar excess of alkene was required for attachment.

Given the high density attachment to the particle surface, a supramolecular alkene, Fullerene-C_{60} was attached to the particle surface, to form C_{60}-f-SiNP, which was characterized extensively. The complexity of the thiol-Fullerene-C_{60} was further evidenced by exploring the reaction between Fullerene-C_{60} and dodecanethiol.

It was revealed that optical heating would transform the C_{60}-f-SiNP, where the particle transforms into hollow particles, and carbonaceous flakes. The temperature profile of these energetic events was also recorded and discussed, where multiple energetic events are seen in a cascade pattern.

7.2 Future Work

7.2.1 Particle Growth Mechanisms

The growth of functionalised silica nanoparticles throughout this work leaned heavily toward the utility of thiol-terminated silica nanoparticles, and their capabilities for high density surface decoration. Particles functionalized from other organosilanes were discussed in this thesis, and further detail into their growth mechanisms, in the case of (phenyl)trimethoxysilane, growth was seen to be much more rapid than other alkoxysilanes discussed in this work, however, the driving force toward the fast rate of growth of the particles is unknown, but is postulated to be due to reaching an early critical micelle concentration due to insolubility.

A study in real-time could provide valuable information into the growth mechanism and condensation states of the particles, at different concentrations and time points. Given the miscibility issues and rapid opacity, real-time monitoring in the form of SANS would determine particle shape, average size and dispersity, which could be achieved at a neutron beamline.

Insight into particle growth mechanisms through real-time UV-Visible spectroscopy studies, would be a good extension of this project, where determination of the Critical Micelle Concentration (CMC) would provide information regarding concentration dependent particle growth mechanisms.

Phenyl functionalised particles see applications in analytical chemistry as a method to capture chlorobenzene [106], and to detect pesticides,[107] where magnetic particles were coated with (phenyl)trimethoxysilane by a post synthesis seeding method. It is envisioned that increased control over surface properties could be obtained by leveraging the high density of phenyl groups expected to be on the particle surface.

7.2.2 Particle Applications

Fundamentally, it would be an interesting notion to consider the effect similar length, but kinked hydrocarbons and, and hydrocarbons with multiple double bond sites, present in terms of attachment density, as well as the configuration of these molecules on the surface of the particle. For molecules such as oleic acid, where the double bond presents in the middle of the molecule, one would expect this to decrease availability, and thus, reactivity of thiols on the surface of the nanoparticle.

For application oriented outcomes, the use of particles in this work could be tailored to the incorporation of more robust, stimuli responsive molecules on the particle surface. Surface decoration with imaging agents and flurophores could improve the efficiency (quantum yield) of fluorescence and related excitation mechanisms, given the increased rigidity of the molecule upon tethering to a particle surface.[108, 109]

Given the high specific heat capacity of silica, another potential application could be to attach electron transport agents to the surface of the particle, which was originally the idea with Fullerene-$C_{60.}$ It would be important in this case that the charge carrier of interest is distanced appropriately from the particle by linking group of suitable chain length as to not interfere with the transport process.

7.2.3 Application of C_{60}-f-SiNP

The unique energetic properties of C_{60}-f-SiNP revealed that it did not require a desorption matrix for MALDI-ToF-MS analysis and would form interesting structures upon ablation.

Further investigation into the ablation of C_{60}-f-SiNP, as well as a suitable procedure to be able to extract the hollow shells created by optical heating from the Nd:YAG laser, which could provide for specific testing to be done on the material formed, as it is created in this thesis at sparingly low yields.

Interestingly, in the case of C_{60}-f-SiNP, it did not require a matrix for desorption of Fullerene-C_{60}, which is quite uncommon, where π-conjugated molecules such as 9-Nitroanthracene are generally used. Protein and peptide detection is commonly enriched by silica particles acting as a suitable matrix[110, 111], and it is envisioned that the C_{60}-f-SiNP could demonstrate similar properties, but for π-conjugated species, instead of amino-acids.

Chapter 8| References

1. Bohr, M.T., *Nanotechnology goals and challenges for electronic applications.* IEEE Transactions on Nanotechnology, 2002. **1**(1): p. 56-62.
2. Roco, M.C. and W.S. Bainbridge, *Societal implications of nanoscience and nanotechnology: Maximizing human benefit.* Journal of Nanoparticle Research. **7**(1): p. 1-13.
3. Eustis, S. and M.A. El-Sayed, *Why gold nanoparticles are more precious than pretty gold: Noble metal surface plasmon resonance and its enhancement of the radiative and nonradiative properties of nanocrystals of different shapes.* Chemical Society Reviews, 2006. **35**(3): p. 209-217.
4. Jang, S.P. and S.U.S. Choi, *Role of Brownian motion in the enhanced thermal conductivity of nanofluids.* Applied Physics Letters, 2004. **84**(21): p. 4316-4318.
5. Mintsa, H.A., et al., *New temperature dependent thermal conductivity data for water-based nanofluids.* International Journal of Thermal Sciences, 2009. **48**(2): p. 363-371.
6. Nguyen, C.T., et al., *Temperature and particle-size dependent viscosity data for water-based nanofluids – Hysteresis phenomenon.* International Journal of Heat and Fluid Flow, 2007. **28**(6): p. 1492-1506.
7. Choi, O. and Z. Hu, *Size Dependent and Reactive Oxygen Species Related Nanosilver Toxicity to Nitrifying Bacteria.* Environmental Science & Technology, 2008. **42**(12): p. 4583-4588.
8. Carlson, C., et al., *Unique Cellular Interaction of Silver Nanoparticles: Size-Dependent Generation of Reactive Oxygen Species.* The Journal of Physical Chemistry B, 2008. **112**(43): p. 13608-13619.
9. He, C., et al., *Effects of particle size and surface charge on cellular uptake and biodistribution of polymeric nanoparticles.* Biomaterials, 2010. **31**(13): p. 3657-3666.
10. Albanese, A., P.S. Tang, and W.C.W. Chan, *The Effect of Nanoparticle Size, Shape, and Surface Chemistry on Biological Systems.* Annual Review of Biomedical Engineering, 2012. **14**(1): p. 1-16.
11. Chithrani, B.D., A.A. Ghazani, and W.C.W. Chan, *Determining the Size and Shape Dependence of Gold Nanoparticle Uptake into Mammalian Cells.* Nano Letters, 2006. **6**(4): p. 662-668.
12. Allure-Media, *Gold Is Surging, And It's Having An Awesome 2014*, gold-is-surging-and-its-having-an-awesome-2014.jpg, Editor. 2014, Business Insider Australia: World Wide Web.
13. Ted Pella, I., *Unconjugated Gold Sols*, gold-colloids-wcopy.jpg, Editor. 2016, Ted Pella Microscopy: World Wide Web.
14. Cytodiagnostics, *Introduction to Gold Nanoparticle Characterization*, G.N. Absorbance, Editor. 2016, Cytodiagnostics Inc.: World Wide Web.
15. Zahn, M., *Magnetic Fluid and Nanoparticle Applications to Nanotechnology.* Journal of Nanoparticle Research, 2001. **3**(1): p. 73-78.
16. Qian, X.M. and S.M. Nie, *Single-molecule and single-nanoparticle SERS: from fundamental mechanisms to biomedical applications.* Chemical Society Reviews, 2008. **37**(5): p. 912-920.
17. Shipway, A.N., E. Katz, and I. Willner, *Nanoparticle Arrays on Surfaces for Electronic, Optical, and Sensor Applications.* ChemPhysChem, 2000. **1**(1): p. 18-52.

18. Tiede, K., et al., *Detection and characterization of engineered nanoparticles in food and the environment.* Food Additives & Contaminants: Part A, 2008. **25**(7): p. 795-821.
19. Roy, I., et al., *Optical tracking of organically modified silica nanoparticles as DNA carriers: A nonviral, nanomedicine approach for gene delivery.* Proceedings of the National Academy of Sciences of the United States of America, 2005. **102**(2): p. 279-284.
20. Zhu, R., et al., *Molecularly imprinted layer-coated silica nanoparticles for selective solid-phase extraction of bisphenol A from chemical cleansing and cosmetics samples.* Analytica Chimica Acta, 2010. **658**(2): p. 209-216.
21. Wieckowski, A., E.R. Savinova, and C.G. Vayenas, *Catalysis and electrocatalysis at nanoparticle surfaces*. 2003: CRC Press.
22. Balazs, A.C., T. Emrick, and T.P. Russell, *Nanoparticle polymer composites: where two small worlds meet.* Science, 2006. **314**(5802): p. 1107-1110.
23. Tan, W., et al., *Bionanotechnology based on silica nanoparticles.* Medicinal Research Reviews, 2004. **24**(5): p. 621-638.
24. Xia, T., et al., *Polyethyleneimine Coating Enhances the Cellular Uptake of Mesoporous Silica Nanoparticles and Allows Safe Delivery of siRNA and DNA Constructs.* ACS Nano, 2009. **3**(10): p. 3273-3286.
25. Chang, J.-S., et al., *In Vitro Cytotoxicitiy of Silica Nanoparticles at High Concentrations Strongly Depends on the Metabolic Activity Type of the Cell Line.* Environmental Science & Technology, 2007. **41**(6): p. 2064-2068.
26. Salata, O., *Applications of nanoparticles in biology and medicine.* Journal of Nanobiotechnology, 2004. **2**(1): p. 1-6.
27. Ahamed, M., M.S. AlSalhi, and M.K.J. Siddiqui, *Silver nanoparticle applications and human health.* Clinica Chimica Acta, 2010. **411**(23–24): p. 1841-1848.
28. Schmidt, O.G., et al., *Nanotechnology — Bottom-up Meets Top-down*, in *Advances in Solid State Physics*, B. Kramer, Editor. 2002, Springer Berlin Heidelberg: Berlin, Heidelberg. p. 231-240.
29. Shimomura, M. and T. Sawadaishi, *Bottom-up strategy of materials fabrication: a new trend in nanotechnology of soft materials.* Current Opinion in Colloid & Interface Science, 2001. **6**(1): p. 11-16.
30. Mijatovic, D., J.C.T. Eijkel, and A. van den Berg, *Technologies for nanofluidic systems: top-down vs. bottom-up-a review.* Lab on a Chip, 2005. **5**(5): p. 492-500.
31. Domènech, B., et al., *Bifunctional Polymer-Metal Nanocomposite Ion Exchange Materials, Ion Exchange Technologies*, in *InTech*, P.A. Kilislioglu, Editor. 2012.
32. Taylor, S.R., *Abundance of chemical elements in the continental crust: a new table.* Geochimica et Cosmochimica Acta, 1964. **28**(8): p. 1273-1285.
33. Travitzky, N., et al., *Additive Manufacturing of Ceramic-Based Materials.* Advanced Engineering Materials, 2014. **16**(6): p. 729-754.
34. Stöber, W., A. Fink, and E. Bohn, *Controlled growth of monodisperse silica spheres in the micron size range.* Journal of Colloid and Interface Science, 1968. **26**(1): p. 62-69.
35. Donaldson, L., *'Cornell Dots' receive approval for clinical trials: Nanotechnology.* Materials Today, 2011. **14**(4): p. 131.
36. Cottingham, K., *Quantum Dots Leave the Light On.* Analytical Chemistry, 2005. **77**(17): p. 354 A-357 A.
37. Choyke, P.L., *Nanoparticles: Take only pictures, leave only footprints.* Science translational medicine, 2014. **6**(260): p. 260fs44-260fs44.
38. Burns, A., et al., *Core/Shell Fluorescent Silica Nanoparticles for Chemical Sensing: Towards Single-Particle Laboratories.* Small, 2006. **2**(6): p. 723-726.

39. Fu, Y., J. Zhang, and J.R. Lakowicz, *Plasmonic Enhancement of Single-Molecule Fluorescence Near a Silver Nanoparticle.* Journal of Fluorescence, 2007. **17**(6): p. 811-816.
40. Brinker, C.J. and G.W. Scherer, *Sol-gel science: the physics and chemistry of sol-gel processing*. 2013: Academic press.
41. Woodhead, J. and D. Segal, *Sol-gel processing.* Chemistry in Britain, 1984. **20**(4): p. 310 - 313.
42. van Blaaderen, A. and A. Vrij, *Synthesis and Characterization of Monodisperse Colloidal Organo-silica Spheres.* Journal of Colloid and Interface Science, 1993. **156**(1): p. 1-18.
43. Margulis-Goshen, K. and S. Magdassi, *Organic nanoparticles from microemulsions: Formation and applications.* Current Opinion in Colloid & Interface Science, 2012. **17**(5): p. 290-296.
44. Arriagada, F.J. and K. Osseo-Asare, *Synthesis of Nanosize Silica in a Nonionic Water-in-Oil Microemulsion: Effects of the Water/Surfactant Molar Ratio and Ammonia Concentration.* Journal of Colloid and Interface Science, 1999. **211**(2): p. 210-220.
45. Schubert, U. and N. Hüsing, *Synthesis of inorganic materials*. 2012: John Wiley & Sons.
46. Schladt, T.D., et al., *Synthesis and bio-functionalization of magnetic nanoparticles for medical diagnosis and treatment.* Dalton Transactions, 2011. **40**(24): p. 6315-6343.
47. Pontoni, D., T. Narayanan, and A.R. Rennie, *Time-Resolved SAXS Study of Nucleation and Growth of Silica Colloids.* Langmuir, 2002. **18**(1): p. 56-59.
48. Kousaka, Y., T. Nomura, and M. Alonso, *Simple model of particle formation by homogeneous and heterogeneous nucleation.* Advanced Powder Technology, 2001. **12**(3): p. 291-309.
49. Slowing, I.I., et al., *Mesoporous silica nanoparticles as controlled release drug delivery and gene transfection carriers.* Advanced Drug Delivery Reviews, 2008. **60**(11): p. 1278-1288.
50. Park, C., et al., *Controlled release of guest molecules from mesoporous silica particles based on a pH‐responsive polypseudorotaxane motif.* Angewandte Chemie International Edition, 2007. **46**(9): p. 1455-1457.
51. Zhang, J., et al., *Multifunctional envelope-type mesoporous silica nanoparticles for tumor-triggered targeting drug delivery.* Journal of the American Chemical Society, 2013. **135**(13): p. 5068-5073.
52. Zachariah, M.R., et al., *Dynamic light scattering and angular dissymmetry for the in situ measurement of silicon dioxide particle synthesis in flames.* Appl Opt, 1989. **28**(3): p. 530-6.
53. Lippmaa, E., et al., *Structural studies of silicates by solid-state high-resolution silicon-29 NMR.* Journal of the American Chemical Society, 1980. **102**(15): p. 4889-4893.
54. Bayer, E., et al., *Characterization of chemically modified silica gels by 29 Si and 13 C cross-polarization and magic angle spinning nuclear magnetic resonance.* Journal of Chromatography A, 1983. **264**: p. 197-213.
55. Maidenberg, Y., et al., *Mixed Silane Monolayers for Controlling the Surface Areal Density of Click-Reactive Alkyne Groups: A Method to Assess Preferential Surface Adsorption on Flat Substrates and a Method to Verify Compositional Homogeneity on Nanoparticles.* Langmuir, 2013. **29**(38): p. 11959-11965.
56. Skoog, D.A., F.J. Holler, and S.R. Crouch, *Principles of Instrumental Analysis*. 2007: Thomson Brooks/Cole.
57. Davydov, V.Y., A.V. Kiselev, and L.T. Zhuravlev, *Study of the surface and bulk hydroxyl groups of silica by infra-red spectra and D2O-exchange.* Transactions of the Faraday Society, 1964. **60**(0): p. 2254-2264.

58. Puddu, V. and C.C. Perry, *Interactions at the Silica–Peptide Interface: The Influence of Particle Size and Surface Functionality.* Langmuir, 2014. **30**(1): p. 227-233.
59. Christy, A.A. and P.K. Egeberg, *Quantitative determination of surface silanol groups in silicagel by deuterium exchange combined with infrared spectroscopy and chemometrics.* Analyst, 2005. **130**(5): p. 738-744.
60. Iler, R.K., *The colloid chemistry of silica and silicates*. 1955: Cornell University Press.
61. Peri, J.B. and A.L. Hensley, *The surface structure of silica gel.* The Journal of Physical Chemistry, 1968. **72**(8): p. 2926-2933.
62. Ballard, C.C., et al., *ESTERIFICATION OF THE SURFACE OF AMORPHOUS SILICA.* The Journal of Physical Chemistry, 1961. **65**(1): p. 20-25.
63. Azioune, A., et al., *Synthesis and Characterization of Active Ester-Functionalized Polypyrrole−Silica Nanoparticles: Application to the Covalent Attachment of Proteins.* Langmuir, 2004. **20**(8): p. 3350-3356.
64. Wu, Z., et al., *Surface properties of submicrometer silica spheres modified with aminopropyltriethoxysilane and phenyltriethoxysilane.* Journal of colloid and interface science, 2006. **304**(1): p. 119-124.
65. Nakamura, M. and K. Ishimura, *One-pot synthesis and characterization of three kinds of thiol-organosilica nanoparticles.* Langmuir, 2008. **24**(9): p. 5099-5108.
66. Rahman, I., M. Jafarzadeh, and C. Sipaut, *Synthesis of organo-functionalized nanosilica via a co-condensation modification using γ-aminopropyltriethoxysilane (APTES).* Ceramics International, 2009. **35**(5): p. 1883-1888.
67. Jung, H.-S., D.-S. Moon, and J.-K. Lee, *Quantitative Analysis and Efficient Surface Modification of Silica Nanoparticles.* Journal of Nanomaterials, 2012. **2012**: p. 8.
68. Corrie, S.R., G.A. Lawrie, and M. Trau, *Quantitative Analysis and Characterization of Biofunctionalized Fluorescent Silica Particles.* Langmuir, 2006. **22**(6): p. 2731-2737.
69. Dastidar, S., et al., *Fabrication of meso and nanotextured silica surfaces for tunable densities of functionalized molecules.* Colloids and Surfaces A: Physicochemical and Engineering Aspects, 2012. **412**: p. 38-46.
70. Kim, S.H., M. Jeyakumar, and J.A. Katzenellenbogen, *Dual-Mode Fluorophore-Doped Nickel Nitrilotriacetic Acid-Modified Silica Nanoparticles Combine Histidine-Tagged Protein Purification with Site-Specific Fluorophore Labeling.* Journal of the American Chemical Society, 2007. **129**(43): p. 13254-13264.
71. Calero, P., et al., *Chromogenic silica nanoparticles for the colorimetric sensing of long-chain carboxylates.* Chemical Communications, 2008(14): p. 1668-1670.
72. Campos, R., et al., *Fluoroalkyl-Functionalized Silica Particles: Synthesis, Characterization, and Wetting Characteristics.* Langmuir, 2011. **27**(16): p. 10206-10215.
73. Schiestel, T., H. Brunner, and G.E. Tovar, *Controlled surface functionalization of silica nanospheres by covalent conjugation reactions and preparation of high density streptavidin nanoparticles.* Journal of nanoscience and nanotechnology, 2004. **4**(5): p. 504-511.
74. Mader, H.S., *Surface Modification of Silica Particles and Upconverting Particles Using Click Chemistry* in *DER FAKULTÄT CHEMIE UND PHARMAZIE*. 2010, UNIVERSITÄT REGENSBURG.
75. Zhang, G., et al., *Robust Superamphiphobic Coatings Based on Silica Particles Bearing Bifunctional Random Copolymers.* ACS Applied Materials & Interfaces, 2013. **5**(24): p. 13466-13477.
76. Mangos, D.N., T. Nakanishi, and D.A. Lewis, *A simple method for the quantification of molecular decorations on silica particles.* Science and Technology of Advanced Materials, 2014. **15**(1): p. 015002.
77. Hoyle, C.E. and C.N. Bowman, *Thiol–ene click chemistry.* Angewandte Chemie International Edition, 2010. **49**(9): p. 1540-1573.

78. Cramer, N.B., J.P. Scott, and C.N. Bowman, *Photopolymerizations of thiol-ene polymers without photoinitiators.* Macromolecules, 2002. **35**(14): p. 5361-5365.
79. Northrop, B.H. and R.N. Coffey, *Thiol–ene click chemistry: computational and kinetic analysis of the influence of alkene functionality.* Journal of the American Chemical Society, 2012. **134**(33): p. 13804-13817.
80. Hirsch, A. and M. Brettreich, *Fullerenes: Chemistry and Reactions*. 2005: Wiley.
81. Sitharaman, B., *Nanobiomaterials Handbook*. 2011: CRC Press.
82. V. Kleandrova, V., et al., *Review of Structures Containing Fullerene-C60 for Delivery of Antibacterial Agents. Multitasking model for Computational Assessment of Safety Profiles.* Current Bioinformatics, 2015. **10**(5): p. 565-578.
83. McEwen, C.N., R.G. McKay, and B.S. Larsen, *C60 as a radical sponge.* Journal of the American Chemical Society, 1992. **114**(11): p. 4412-4414.
84. Wudl, F., *Fullerene materials.* J. Mater. Chem., 2002. **12**(7): p. 1959-1963.
85. Grillo, R., A.H. Rosa, and L.F. Fraceto, *Engineered nanoparticles and organic matter: A review of the state-of-the-art.* Chemosphere, 2015. **119**: p. 608-619.
86. Bosi, S., et al., *Fullerene derivatives: an attractive tool for biological applications.* European journal of medicinal chemistry, 2003. **38**(11): p. 913-923.
87. Hollamby, M.J., et al., *Directed assembly of optoelectronically active alkyl–π-conjugated molecules by adding n-alkanes or π-conjugated species.* Nature chemistry, 2014. **6**(8): p. 690-696.
88. Li, H., et al., *Alternatively Modified Bingel Reaction for Efficient Syntheses of C60 Hexakis-Adducts.* Organic letters, 2006. **8**(24): p. 5641-5643.
89. Prato, M., et al., *Addition of azides to fullerene C60: synthesis of azafulleroids.* Journal of the American Chemical Society, 1993. **115**(3): p. 1148-1150.
90. Rubin, Y., et al., *Synthesis and x-ray structure of a Diels-Alder adduct of fullerene C60.* Journal of the American Chemical Society, 1993. **115**(1): p. 344-345.
91. Dixon, D.A., et al., *Patterns for addition to fullerene (C60).* The Journal of Physical Chemistry, 1992. **96**(15): p. 6107-6110.
92. Tzirakis, M.D. and M. Orfanopoulos, *Radical Reactions of Fullerenes: From Synthetic Organic Chemistry to Materials Science and Biology.* Chemical Reviews, 2013. **113**(7): p. 5262-5321.
93. Iskin, B., G. Yilmaz, and Y. Yagci, *Mono-addition Synthesis of Polystyrene–Fullerene (C60) Conjugates by Thiol–Ene Chemistry.* Chemistry–A European Journal, 2012. **18**(33): p. 10254-10257.
94. Krishna, V., et al., *Optical heating and rapid transformation of functionalized fullerenes.* Nature nanotechnology, 2010. **5**(5): p. 330-334.
95. Iijima, S., *Carbon nanotubes: past, present, and future.* Physica B: Condensed Matter, 2002. **323**(1): p. 1-5.
96. Bellamy, M.K., *Using FTIR-ATR Spectroscopy To Teach the Internal Standard Method.* Journal of Chemical Education, 2010. **87**(12): p. 1399-1401.
97. Kuentzel, L.E., *Calcium Carbonate as Internal Standard for Quantitative Infrared Analysis.* Analytical Chemistry, 1955. **27**(2): p. 301-301.
98. Robinson, J.W., E.M.S. Frame, and G.M. Frame, *Undergraduate Instrumental Analysis, Sixth Edition*. 2004: Taylor & Francis.
99. Khire, V.S., T.Y. Lee, and C.N. Bowman, *Synthesis, characterization and cleavage of surface-bound linear polymers formed using thiol− ene photopolymerizations.* Macromolecules, 2008. **41**(20): p. 7440-7447.
100. Wang, S., et al., *Nanomaterials and singlet oxygen photosensitizers: potential applications in photodynamic therapy.* Journal of Materials Chemistry, 2004. **14**(4): p. 487-493.

101. Rather, J.A. and K. De Wael, *Fullerene-C 60 sensor for ultra-high sensitive detection of bisphenol-A and its treatment by green technology.* Sensors and Actuators B: Chemical, 2013. **176**: p. 110-117.
102. Cremonini, M., et al., *Addition of alkylthiyl and alkoxy radicals to C60 studied by ESR.* The Journal of Organic Chemistry, 1993. **58**(17): p. 4735-4738.
103. Hunter, J., et al., *C120+ Isomers from Laser Ablation of Fullerene Films.* The Journal of Physical Chemistry, 1994. **98**(31): p. 7440-7443.
104. Trewartha, S., *Light Ignition of Carbon Nanotubes for the Initiation of Energetic Materials*, in *School of Chemical and Physical Sciences*. 2015, Flinders University`.
105. Karahasanoğlu, M., A. Önen, and İ.E. Serhatlı, *Synthesis of hybrid materials via photopolymerization of benzoin functionalized silica nanoparticles.* Progress in Organic Coatings, 2014. **77**(6): p. 1079-1084.
106. Saraji, M. and N. Khaje, *Phenyl-functionalized silica-coated magnetic nanoparticles for the extraction of chlorobenzenes, and their determination by GC-electron capture detection.* J Sep Sci, 2013. **36**(6): p. 1090-6.
107. Taira, S., et al., *Synthesis and Characterization of Functionalized Magnetic Nanoparticles for the Detection of Pesticide.* International Journal of Inorganic Chemistry, 2012. **2012**: p. 7.
108. Ow, H., et al., *Bright and Stable Core−Shell Fluorescent Silica Nanoparticles.* Nano Letters, 2005. **5**(1): p. 113-117.
109. Yang, W., et al., *Novel fluorescent silica nanoparticle probe for ultrasensitive immunoassays.* Analytica Chimica Acta, 2004. **503**(2): p. 163-169.
110. Cheng, M.M.-C., et al., *Nanotechnologies for biomolecular detection and medical diagnostics.* Current Opinion in Chemical Biology, 2006. **10**(1): p. 11-19.
111. Chen, H., C. Deng, and X. Zhang, *Synthesis of Fe3O4@ SiO2@ PMMA Core–Shell–Shell Magnetic Microspheres for Highly Efficient Enrichment of Peptides and Proteins for MALDI-ToF MS Analysis.* Angewandte Chemie International Edition, 2010. **49**(3): p. 607-611.